Characterisation of Advanced Thermoelectric Materials and Devices

By Sherko Ghaderi

A thesis submitted to Newcastle University for the degree of Doctor of Philosophy.

School of Engineering

March 2020

Abstract

A successful method in relation to increasing the thermoelectric figure of merit is by means of employing the lattice thermal conductivity, seeing as this one of the parameters which is not affected by the electronic structure of the material. It can be accomplished by employing the sol-gel method to synthesise the thermoelectric materials. The advantage of the sol-gel method includes minimisation of the lattice vibration and consequently, lower thermal conductivity.

In this thesis, the thermoelectric characterisation of nickel nanoparticles embedded in silica aerogel at two different concentrations has studied and compared with pure silica aerogel. The samples exhibit a significant increase in electrical conductivity, while the sample's thermal conductivity remained almost unchanged. This promising result has motivated the nanostructuring of Zn_4Sb_3 and embed it in the silica aerogel using the sol-gel method.

Thermal conductivity measurement using scanning thermal microscopy proven to be a technique to evaluate the thermal conductivity at submicron scale. However, this technique is limited by several important parameters in relation to extracting thermal conductivity. In this thesis, thermal conductivity measurements using scanning thermal microscopy were studied and all relevant parameters measured experimentally with the aim of improving the accuracy of the thermal conductivity measurements. Likewise, a method has created that will measure the seebeck coefficient of the material using SThM. The advantage of this technique compared with existing methods are direct measurement, no sample preparation and no need to fabricate seebeck coefficient test structures.

In this thesis, the thermoelectric materials are characterised using different techniques to evaluate the performance of the material from 300K to 420K. The measurements system used in the thesis are thermal conductivity measurements using three specific techniques: scanning thermal conductivity, HotDisk analyser and Raman spectroscopy temperature dependence. The electrical resistivity of the materials was studied using the Keithley 4200-SCS four probe station. The material seebeck coefficient was measured using scanning thermal microscopy.

Acknowledgements

I would like to express my gratitude to my supervisors Dr. Sarah Olsen and Professor Lidija Siller for their support and advice throughout this research project. It has been a great pleasure to work with them. Thank you.

Table of contents

Dedicated to

My family and beloved parents

Lists of figures

Nomenclature

Term	*Abbreviation*
Atomic Force Microscope	AFM
Full Width at Half Maximum	FWHM
Kelvin Nanotechnology	KNT
Molecular Dynamics	MD
Scanning Electron Microscope	SEM
Scanning Thermal Microscopy	SThM
Scanning Probe Microscope	SPM
Thermoelectric Figure of Merit	ZT
Transmission Electron Microscopy	TEM
X-ray Diffraction	XRD

Symbol	*Variable*	*Unit*
a	Thickness of the meniscus	m
ac	Radius of mechanical contact	m
b	Equivalent radius of the thermal exchange	m
b_w	Wire width	m
C	Heat capacity	J kg^{-1} K^{-1}
C_p	Heat capacity at constant pressure	J kg^{-1} K^{-1}
C_{pa}	Heat capacity due to acoustic phonons	J kg^{-1} K^{-1}
C_v	Heat capacity at constant volume	J kg^{-1} K^{-1}
D	Diameter	m
d	Thickness	m
d_0	Mass Density	kg m^{-3}
d_s	Tip-sample separation distance	m
E	Young modulus	Pa
f	Frequency	Hz
$G_{atom-atom}$	Thermal conductance of atom-atom contact	W K^{-1}

G_c	Contact thermal conductance	W K^{-1}
G_{eq}	Equivalent thermal conductance	W K^{-1}
G_p	Probe thermal conductance	W K^{-1}
$G_{p\text{-}w}$	Probe-water thermal conductance	W K^{-1}
$G_{w\text{-}s}$	Water-sample thermal conductance	W K^{-1}
G_Q	Quantum thermal conductance	W K^{-1}
G_{rad}	Thermal conductance of radiation	W K^{-1}
G_s	Thermal conductance of the sample	W K^{-1}
G_{ss}	Thermal conductance of the solid-solid contact	W K^{-1}
$G_{total,\ meniscus}$	The total conductance of the water meniscus	W K^{-1}
G_w	Thermal conductance through the water meniscus	W K^{-1}
h	Heat transfer coefficient	W m^{-2} K^{-1}
hk	Meniscus height	m
I	Electrical current	A
I_t	Total electrical current	A
K_1	Correction factor	
kx	X-component of the wave vector	
L	Length	m
FN	Applied force	N
F_{ad}	Adhesion force	N
F_{cap}	Capillary forces	N
F_{po}	Pull-off forces	N
G_r	Grashof number	
G_{air}	Thermal conductance through air	WK^{-1}
N	Number of phonon modes	
N_u	Nusselt number	
p	Fin perimeter	m
P_a	Probe Joule power - Probe free in air	W
P_c	Probe Joule power - Probe in contact with sample	W
P_p	Power dissipated in the probe	W
P_d	Power dissipated in the heater (heating wire)	W
P_{rms}	Power per unit heater length	Wm^{-1}
P_r	Prandtl number	
Q	Heat flux	W

R	Electrical resistance	Ω
R_a	Tip apex radius	m
R_{ar}	Arithmetic value of roughness	m
R_b	Thermal boundary resistance	m^2 K W^{-1}
R_g	Gas constant	J mol^{-1} K^{-1}
R_s	Spreading thermal resistance	K W^{-1}
R_{th}	Interface thermal resistance	K W^{-1}
R_{p-p}	Peak-to-peak roughness	m
R_{sph}	Sphere radius	m
R_{tip}	Tip thermal resistance	K W^{-1}
$R_{interface}$	Thermal resistance at the tip-sample interface	K W^{-1}
R_0	Electrical resistance of the probe at Ta	Ω
R_H	Relative humidity	
r_1	Smallest meniscus radius	m
r_k	Cavity radius	m
S	Section	m^2
T	Temperature	K
T_a	Ambient Temperature	K
t_1	Film thickness	m
t_{12}	Phonon transmission coefficient	
V	Voltage	V
V_{DC}	Continuous voltage	V
V_m	Molar volume	m^3 mol^{-1}
$V_{3\omega}$	Third harmonic voltage	V
w	Width	m

Greek symbols

α	Thermal diffusivity	m^2 s^{-1}
γw	Water surface tension	N m^{-1}
θ	Relative temperature	K
θ	Mean Relative temperature	K
θ_{DC}	Continuous relative temperature	K
θ_{2w}	Second harmonic relative temperature	K

γ	Cp/Cv	
λ_{max}	Maximum wavelength of thermal radiation	μm
λ	Thermal conductivity	W m^{-1} K^{-1}
λ_{pp}	Phonon-phonon thermal conductivity	W m^{-1} K^{-1}
λ_{w}	Thermal conductivity of water	W m^{-1} K^{-1}
λ_{max}	Maximum wavelength of thermal radiation	m
Λ	Phonon mean free path	m
μ	Diffusion length	m
ν	Poisson ratio	
v_{pa}	Velocity of acoustic phonons	m s^{-1}
ρ	Electrical resistivity	Ω m^{-1}
Φ	Phase lag	°
Φ_d	Heat flow density	W m^{-2}
ω	Angular frequency	Rad s^{-1}

Chapter 1

Introduction

1.1 Thermoelectricity

Energy is essential for all activity to occur. As the global population grows and new industrial economies emerge, energy demands continue to increase at a rapid pace. As it is confronted by this challenge, new types of energy supply are necessary, while limiting the environmental impact that our energy use causes. Answering this challenge requires all available energy resources. Converting energy with high efficiency is one of the major challenges of energy production. Additionally, employing thermoelectric materials improves the effectiveness of applications and can be used as an energy harvester that directly converts waste heat into electricity.

Thermoelectricity refers to the ability of current to flow inside materials due to a temperature difference.[1] The electrical conductance G of a nanoscale device with a channel that is connected with two contacts as shown in Figure 1-1 can be expressed as:[2]

$$G = \frac{2q^2}{h}\int T(E)M(E)\left(\frac{\partial f_0}{\partial E}\right)dE \qquad \text{Equation 1-1}$$

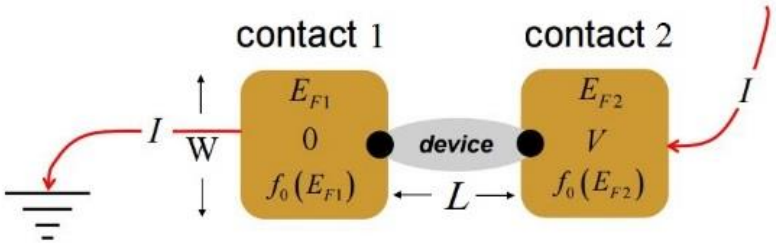

Figure 1. 1: Thermoelectric device connected with two contacts[3]

Conductance is proportional to the quantized conductance $2q^2/h$ correlated with the contacts.[3] Here, q is the electron charge and h is the Planck constant. Conductance is also related to the conducting channels number $M\ (E)$ at energy *E* and moreover, is proportional to the conductor width in the 2D materials and to the cross-sectional part in the 3D materials.[2-3]

Conductance is also proportional to the transmission *T (E)*, which is the probability of an electron with energy *E* introduced via one contact to the other contact.[3] It should be noted that the expression for electrical conductance has been observed to be effective in 1D, 2D and 3D and also in ballistic, diffusive and quasi-ballistic resistors for the appropriate expression of *M (E), T (E)*.[3] The electrical voltage in the bulk is $\varepsilon_x = \rho_n J_{nx}$ (Vm^{-1}). A similar equation can be derived for 2D and 1D cases.[2-3]

Heat flux J_Q, due to heat transported by lattice vibration, the device phonons with two contacts shown in Figure 1-1 can be expressed as:[1-3]

$$J_Q = -k_L \frac{dT_L}{d_x} \quad \mathrm{Wm}^{-2} \qquad \text{Equation 1-2}$$

where k_L is lattice thermal conductivity. The electrons in the state are filled according to the equilibrium Fermi-Dirac function and phonons obey Bose-Einstein statistics.[4] The heat current is a combination of thermal conductance and temperature difference.[5]

The total electrical current (I_t) of a resistor bulk where two contacts are separated by length (L) within the existence of a temperature gradient is:[6]

$$I_t = G\Delta V + S_T \Delta T \qquad \text{Equation 1-3}$$

where S_T is the Soret coefficient in AK^{-1} which is defined as the ratio of the thermal diffusion coefficient to the normal diffusion coefficient. Thermoelectricity contains the flow of heat and charge. The heat current I_Q at temperature gradient is:[7-8]

$$I_Q = -TS_T \Delta V - K_0 \Delta T \qquad \text{Equation 1-4}$$

where K_0 is the electronic heat conduction due to electron in WK^{-1} and *T* is temperature in K. It should be stated that both the lattice (phonons) and the electrons participate in the conduction of heat. The lattice thermal conductivity (k_n) is related to the electronic thermal conductivity (k_0) in the n-type semiconductor as follows:[9]

$$k_n = k_0 - s_n^2 \sigma_n T \qquad \text{Equation 1-5}$$

The s_n is Seebeck coefficient for *n* type conductor in WK^{-1} and σ_n is conductivity in Sm^{-1}.

1.2 Electric current flow: the Seebeck effect

The Seebeck effect is the appearance of potential differences due to the existence of a temperature gradient in a material (Figures 1-2). When a temperature difference exists between two ends of the material (T_1, T_2), electrons go from the hot to the cold end. Consequently, a positive voltage must develop to halt the diffusion. Similarly, for a p-type semiconductor, a negative open-circuit voltage develops. This open-circuit voltage is termed Seebeck voltage (ΔV).[10-11]

$$\Delta V = -\int_{T_1}^{T_2} S\,(T)\,dT \qquad \text{Equation 1-6}$$

.

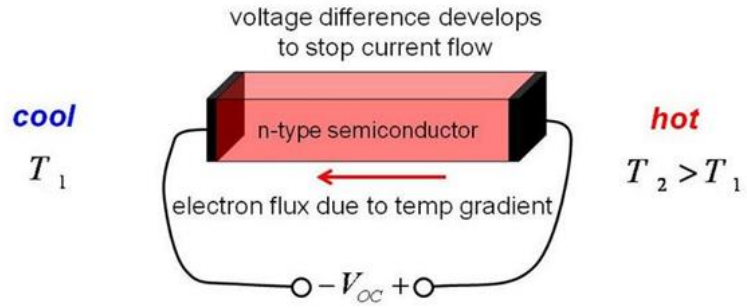

Figure 1. 2: N-type semiconductor in relation to the existence of a temperature gradient[3]

It should be noted that the Seebeck effect can be explained in terms of Fermi levels.[9] The current flow depends on the difference in Fermi energy $(f_E = 1/1 + e^{(E-E_F)/k_BT})$ of two contacts. In highly doped n-type semiconductors, the levels which are conducting the current are above the Fermi level $(f_2(T_2) > f_1(T_1))$. Therefore, for the current to be discontinued, contact 2 must create a positive voltage to lower its Fermi level and produce $(f_2(T_2) = f_1(T_1))$. Alternatively, in the case of a highly doped p-type semiconductor, seeing as the states are below the fermi level $(f_2(T_2) < f_1(T_1))$, a negative voltage should be created on contact 2 to raise its Fermi level and produce $(f_2(T_2) = f_1(T_1))$. The Seebeck coefficient $(S(T))$ relates to the difference between the average energy at which the current flows and the Fermi levels:[1-3]

$$S_n(T) = \left(\frac{K_B}{-q}\right)\left(\frac{E_c - E_F}{K_B T} + \delta_n\right) \qquad \text{Equation 1-7}$$

$$S_p(T) = \left(\frac{K_B}{+q}\right)\left(\frac{E_F - E_v}{K_B T} + \delta_p\right) \qquad \text{Equation 1-8}$$

where δ_p indicates how far the average current flows from the conduction band edge (E_c) in a n-type semiconductor or (E_v) in p-type semiconductors and q is the electron charge that has a value of 1.6×10^{-19} C .[9]

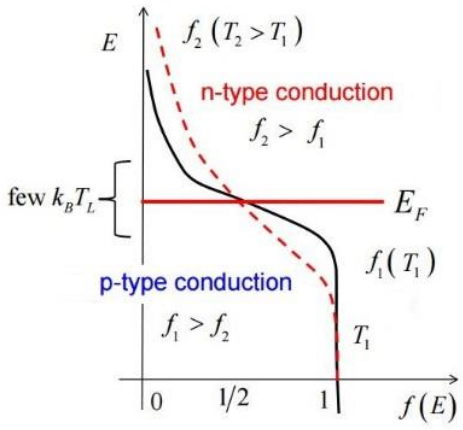

Figure 1. 3: Equilibrium Fermi function vs. the energy of two distinctive temperatures[9]

1.3 Heat current flow: the Peltier effect

In 1834, Peltier discovered the second law of the thermoelectric effect, where an isothermal sample consisting of an electric current driven into one of the contacts enables electrons to flow from one end to the other. As the electrons flow, they transmit energy (heat); therefore, an electron current is supplemented by means of a heat current. It should be noted that the Peltier effect is primarily an interface effect, as the energy transfer occurs at the interface of metal to semiconductor which makes the junction cold.[12]

The magnitude of absorbed and produced heat (Q) at the junction when a current (I) is present is expressed as:

$$Q = \Pi(T)\ I \qquad \text{Equation 1-9}$$

The symbol $\Pi(T)$ is the Peltier coefficient, which depends on the direction of the current being positive or negative.[11]

The Seebeck ($S(T)$) and Peltier ($\prod(T)$) effects have an intimate relationship, known as the Kelvin relation. This relationship demonstrates that the Seebeck effects and Peltier are fundamentally related by temperature T:[10]

$$\Pi(T) = T\,S(T) \qquad \text{Equation 1-10}$$

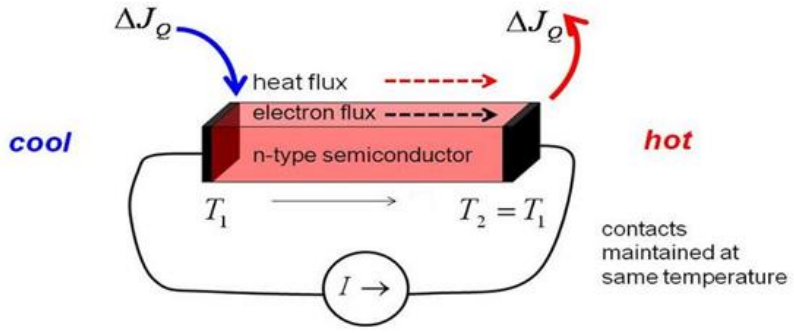

Figure 1. 4: n-type semiconductor slab with a current source that forces heat flow[3]

1.4 The Thomson effects

In the Seebeck effect an electric current will be induced in a material under a temperature gradient. The Peltier effect is exchanging heat within the environment when an electrical current goes through a material. Therefore, both a temperature gradient and electric field are present and occur at the same time inside the single material. This is termed the Thomson effect (κ) and includes only a single material. Therefore, there is no need for a junction.[10]

When a current (I) is passing through a semiconductor, the Thomson relationship can determine the rate of heat (Q) that is exchanged with the environment:[11]

$$Q = \kappa\, I\, \Delta T \qquad \text{Equation 1- 11}$$

As a result of the Thomson effect, a single thermoelectric device can be used either in power generation or refrigeration mode.

The Seebeck coefficient is associated with the average energy of current transport and both types of thermal conductivity; specifically, lattice and electronic thermal conductivity and it is also proportional to electrical conductivity. It can be written as:[13-14]

$$\frac{k_n}{T\sigma_n} = L \qquad \text{Equation 1-12}$$

which is the Wiedemann-Franz law with $L = 2.44 \times 10^{-8},\ \mathrm{W\,\Omega\,K^{-2}}$ being the Lorentz number and σ_n is electrical conductivity in $\mathrm{Sm^{-1}}$.[14]

1.5 Thermoelectric figures of merit (ZT)

The thermoelectricity of materials involves direct conversion between the electricity and heat. The Peltier, Seebeck and Thomson effects are common ways to exploit the performance of thermoelectric materials. In addition, the thermoelectric material's functioning can be expressed in terms of the figure of merit (ZT):[10]

$$ZT = \frac{S^2\sigma T}{k_n + k_0} \qquad \text{Equation 1-13}$$

where, σ is electrical conductivity, S is the Seebeck coefficient, k_n is the lattice thermal conductivity, k_0 is the carrier (electronic) thermal conductivity and T is the temperature. $S^2\sigma$ is known as the thermoelectric power factor.

Each of these parameters has a crucial role to play in enhancing the ZT.[14]

Symbol	Relation	Name	Unit
S	$\Delta V/\Delta T$	Seebeck coefficient	$\mathrm{VK^{-1}}$
σ	$\Delta I/\Delta V$	Electrical conductivity	$\mathrm{sm^{-1}}$
T	T	Temperature	K
K	$1/T\ (\Delta Q/\Delta d)$	Thermal conductivity	$\mathrm{Wm^{-1}K^{-1}}$

Table 1.1: Thermoelectric materials factors[14]

The challenge in producing a high figure of merit (ZT) lies in simultaneously attaining a high Seebeck coefficient, high electrical conductivity in addition to low thermal conductivity in the same solid. These parameters are temperature-dependent and are closely interrelated in such a way that by enhancing one parameter, the other decreases.

The contributions made by the ZT parameters are illustrated in Figure 1-5.[15] This graph demonstrates that a considerable Seebeck effect (very low carrier concentration) is required. Materials comprising a high Seebeck coefficient can be created in insulators with a wide band gap, in addition to a low carrier density semiconductor.[16] To have extensive electrical conductivity, a material with a narrow band gap is desirable. These materials with high electrical conductivity can be uncovered in metals, as well as high concentration semiconductors. Consequently, optimisation of these parameters is required, in order for the materials to have thermoelectric properties. High-quality thermoelectric materials are heavily-doped semiconductors ranging from 10^{20} to 10^{21} (carrier cm^{-3}) to make sure that high conductivity occurs. In addition, to have a sizable net Seebeck effect, a single type carrier (P or N type) is necessary.

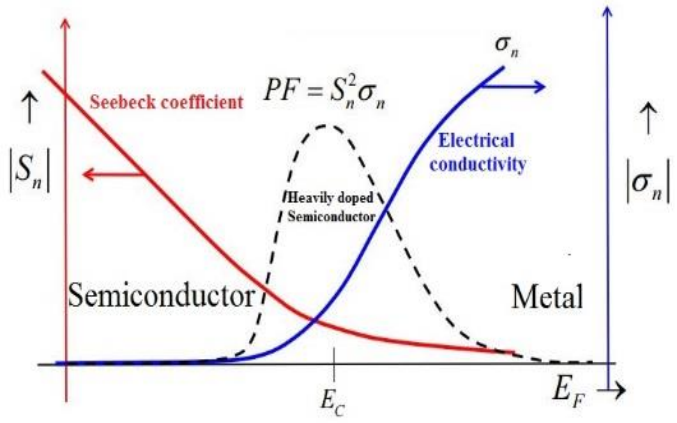

Figure 1. 5: Contributions to ZT [17]

The Seebeck effect depends primarily on the difference in the Fermi levels of materials,[18] whereas electrical conductivity is dependent on the amount of conduction channels and the average free path of the carriers.[19-20] The denominator of the ZT is the thermal conductivity. Typically, the lattice thermal conductivity might be engineered with the aim of improving the ZT.[21]

1.6 Thermoelectric devices

Thermoelectric devices consist of thermoelectric materials and can therefore, be employed in various applications. Thus, a thermoelectric device could possibly be conjoined with other energy converters, for instance photovoltaic devices that are unsuccessful in capturing the thermal part of solar energy, or can work as independent devices in power generation, refrigeration and sensors. Improving the efficiency of thermoelectric devices may possibly mean that they are applied more in conventional applications. There are numerous advantages in using thermoelectric devices compared to fossil fuels, solar energy and nuclear source generators. The benefits consist of the absence of moving parts, reduced maintenance and independence from the type of heat source.

High-quality thermoelectric materials have the N-type and P-types separated to produce a single type carrier, which increases the Seebeck coefficient.[21] Furthermore, a small band gap and sufficiently highly doped materials are necessary, in order to increase mobility and, as a consequence, increase electrical conductivity. Thermoelectric devices consist of two legs connected in series, in addition to two ends which are shorted at the top for current flow supplied by a current source situated at the bottom, although there is a thermal parallel to the heat flow. Each of the legs comprises doped materials with $S > 0$ for p-type and $S < 0$ for n-type.[22-25] The practical importance of the performance of thermoelectric materials occurs lies in the ability to convert heat into electricity in power generation mode, or to force heat to flow in refrigeration mode.

Thermoelectric effects can be used in various applications such as:[25]

1. Power generation (Seebeck effect) $\Delta T \rightarrow \Delta V$
2. Cooling and heating elements (Peltier effect) $\Delta V \rightarrow \Delta T$

Considering a thermoelectric power generator which consists of P-type and N-types of thermoelectric material connected at the hot end and a load connected to the cold end of the module. In the case of the power generator in Figure 1-6, heat is applied to the upper plate and a heat sink on the bottom plates. Thus, positive charges are transferred away from the heat source, down the P-type leg via the load, whilst the current is conveyed back into the load on the left and continues up the N-type leg. In the N-type leg, the electrons are transported away from the heat source to complete the circuit. Here, the Seebeck effect will generate a potential difference and current flow through the load.[26-27]

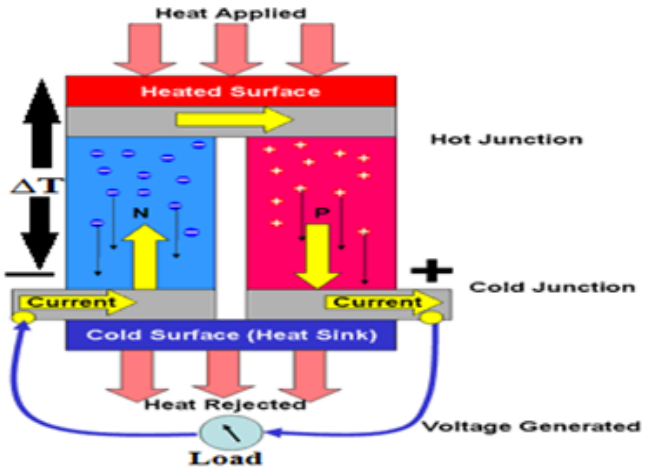

Figure 1. 6: Thermoelectric power generator [26]

The temperature difference between the two ends provides the voltage and heat flow at both legs, which enables the current. Maximum power is attained once the internal resistance of the module is equivalent to the load resistance (load matching). Thus, the internal resistance of the module not only depends on the electrical resistance of thermoelectric materials but is also reliant on the electrical resistance of the metal and the metal interconnector between the modules, and, moreover, is dependent on the geometry of the materials such as the area (A) and, length (L).[27] Similar to electrical resistance, thermal conductance includes radiation and conduction of entire modules and, in addition, also has an effect on efficiency.

The maximum efficiency of the module is expressed as:[27]

$$\eta_{max} = \frac{\Delta T}{T_H} \times \frac{\sqrt{1+Z\bar{T}}-1}{\sqrt{1+Z\bar{T}}+\frac{T_C}{T_H}} \qquad \text{Equation 1-14}$$

where,

ZT = Thermoelectric material figure of merit $\qquad Z\bar{T} = \frac{(S_n - S_P)^2 \bar{T}}{\left[(\rho_n k_n)^{1/2} + (\rho_p k_p)^{1/2}\right]^2}$

$\bar{T}$ = Average temperature between hot and cold surfaces $\qquad \bar{T} = \frac{T_H + T_C}{2}$

$\Delta T = T_H(\text{temperature at hot side}) - T_C(\text{temperature at cold side})$

$\frac{\Delta T}{T_H}$ = Carnot coefficient

The maximum efficiency of thermoelectric power generation involves two terms**.** The first is the Carnot coefficient, where each type of heat engine cannot exceed the Carnot boundary.[17] The second is the thermoelectric properties of the materials used in devices, which are expressed in terms of the figure of merit (ZT).[27]

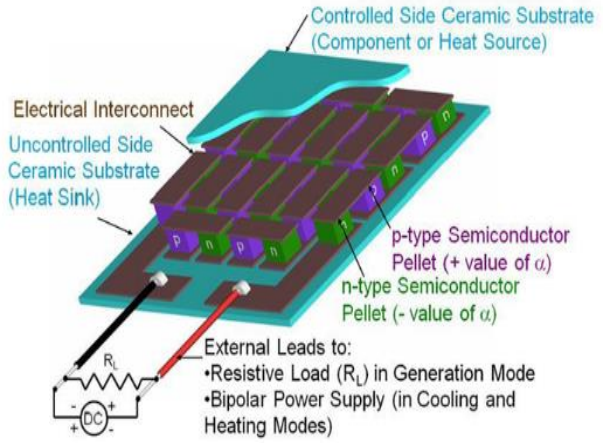

Figure 1. 7: Thermoelectric power generation involving numerous p and n-type thermoelectric materials[26]

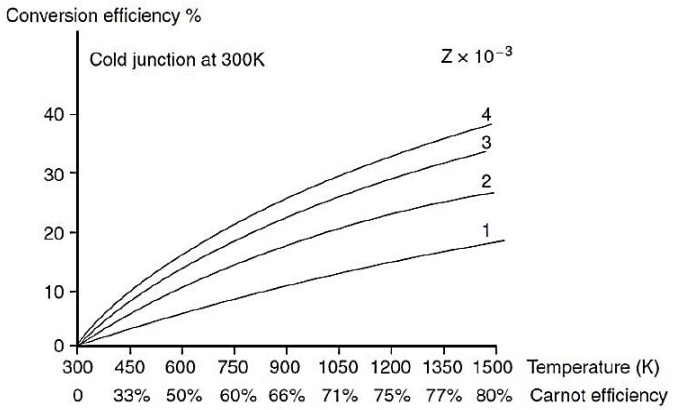

Figure 1. 8: Conversion efficiency of a thermoelectric power generator [27]

Kelvin states that the Peltier effects and Seebeck will occur in a single thermoelectric module. The same theory is also applied to the Peltier cooler, as illustrated in Figure 1-9. However, an external current source will drive carriers inside the materials and force heat to flow from one end to the other.[17]

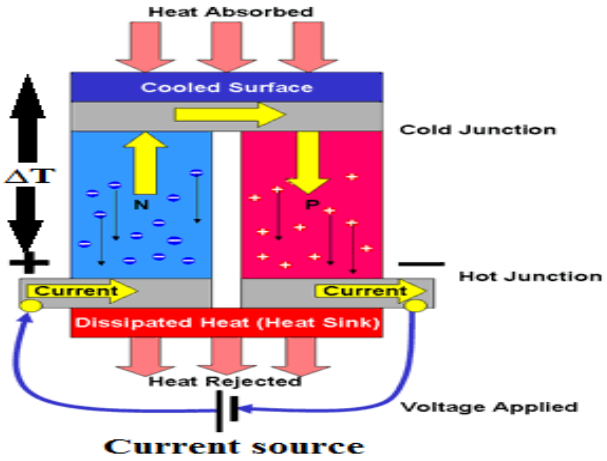

Figure 1. 9: Thermoelectric Peltier cooler [26]

A maximum coefficient of performance will be obtained by using the ZT [26-27] and a temperature difference.

$$\eta_{max} = \frac{T_C}{\Delta T} \times \frac{\sqrt{1+Z\bar{T}} - \frac{T_H}{T_C}}{\sqrt{1+Z\bar{T}}+1} \qquad \text{Equation 1-15}$$

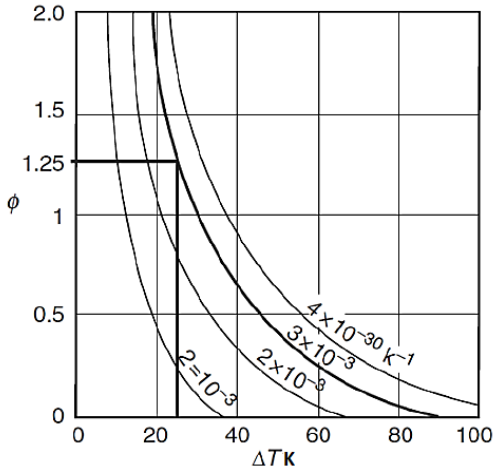

Figure 1. 10: Coefficient of performance of a thermoelectric Peltier cooler [27]

Thermoelectric materials can be applied in numerous applications, depending on the temperature of the application.

I. Room temperature applications (Low temperatures)

a. Implantable medical devices require the batteries to be changed after a number of years. Such devices can be operated by thermoelectric power generation that can harvest

heat from the human body and convert it into electricity so as to activate the device. To allow the device to function, a thermoelectric module with 70 μW in output is sufficient.[28]

b. Thermoelectric power generation can be used to operate wireless sensors. Wireless sensors are a combination of a microelectronic CMOS, battery and sensors. Thus, a thermoelectric power generator can harvest heat by operating the CMOS and convert it into electricity to charge the battery.

II. High temperature (industrial applications)

a. Approximately 90% of global oil and gas needs to be converted in to heat prior to being utilised. However, this method wastes a considerable amount of heat. Hence, only 30% of the overall energy is useful energy, while roughly 70% dissipates.[17] With regards to this, a thermoelectric power generator can be used to convert some of this energy into electricity.

Other thermoelectric applications include:[17]

- Peltier coolers
- Waste-heat recovery, e.g. from vehicles
- Micro refrigerators on chips
- Telecoms laser cooling
- Thermal cycler (DNA amplifier) in the biomedical sector
- Thermoelectric sensors

Table 1-2 provides a list of thermoelectric materials at both room temperature (RT) and high temperature up to 900 K. Moreover, the device efficiency of these materials using Equation 1-15 is also estimated at the peak performance of their temperature. The device efficiency potential of room temperature thermoelectric materials only is calculated for Table 2. As the temperature difference is much larger in high temperature application, any improvement in ZT can also improve device efficiency in high temperature applications.

The maximum efficiency of thermoelectric materials before and after ZT enhancement was calculated based on η_{max}. The maximum efficiency of the single thermocouple versus the temperature difference at a different current and predicted values of ZT is plotted in Figure 1-8. In this calculation, the temperature on the side of the cold end was maintained at 300 K, whilst the temperature on the hot side varied from 300 to 600 K.

The problems associated with this material during fabrication are demonstrated in the table below. The cost and complexity of fabrication and toxicity play significant roles in the application of thermoelectric materials.

The efficiency of a thermoelectric device at room temperature ($\Delta T \approx 25$ K) is low because the thermoelectric material's ZT is low. A theoretical study performed for Zn_4Sb_3 demonstrated nanoporosity can in effect improve the ZT of this specific material by a factor of 5.8. It has been observed that at room temperature, this increase in ZT can improve device efficiency by a factor of 14.

Table 1.2 illustrates that ZT has increased $150\ times$ by making nanowires (instead of bulk), 46 times by introducing doping, and 47 times by using porous material (instead of bulk). Thus, combining these techniques provides a wider scope to improve values of ZT further. The potential is shown of the possibility of increasing ZT significantly by using nanostructuring and porosity and consequently device efficiency could rise.

The efficiency of a thermoelectric device is dependent on:[29]

- ZT
- Amount of heat flow (Q_h) through the material from the side that is hot to the side which is cold

1.7 Possible thermoelectric materials

Three important parameters; specifically, the electrical and thermal conductivity, as well as the Seebeck coefficient need to be selected carefully. Semiconductors have a higher potential for thermoelectric applications and are extremely suitable thermoelectric materials,

	Material	ZT (bulk)	ZT (enhanced)	ZT enhancement factor	Reference	Method to increase ZT	Experimental /theoretical	T (Cold) K	T (Hot) K
Room T performance	Zn4Sb3	0.40	2.32	5.8	7, 8	Porous	THEORETICAL	285	310
	Bi2Te3	0.74	1.05	1.4	1, 2, 3	Nanostructured	measured	285	310
	(Zn0.99Cd0.01)4Sb3	0.40	0.90	2.3	9	Cd- doped	measured	285	310
	ZnSb	0.60	0.90	1.5	10	nanostructured	measured	285	310
	Sb2Te3	0.40	0.74	1.9	14	nanostructured	measured	285	310
	Si	0.02	0.72	36.0	12	Nanowire	measured	285	310
	SrZnSb2	0.14	0.30	2.1	11	Layered	measured	285	310
	MnSi1.75	0.05	0.18	3.6	6	Nano & Porous	measured	285	310
	GaN	0.001	0.002	1.7	13	Skutterudite	measured	285	310
	In4Se3	1.02	1.48	1.5	19	nanostructured	measured	285	1000
	SiGe	0.22	1.30	5.9	16	Nano & Porous	measured	285	1073
	PbTe	0.20	1.96	9.8	4, 5	Superlattice	measured	285	800
High T performance	Ca9Co12O28	0.03	1.20	46.2	20	Co-doped	measured	285	800
	CoSb3	0.05	1.20	23.5	23, 24	In-doped	measured	285	750
	MnSi	0.68	0.80	1.2	22	porous	measured	285	600
	Si100Pi2.5	0.01	0.47	47.0	15	porous	measured	285	900
	Zn0.98Al0.02O	0.30	0.42	1.4	18	Nano & Porous	measured	285	830
	ZnO	0.22	0.61	2.8	17	Nano & Porous	measured	285	478
	IrSb3	0.10	0.15	1.5	21	Skutterudite	measured	285	800

Table 1.2: Thermoelectric materials at both high and room temperature

allowing the separate control of electrical conductivity (electron) σ and thermal conductivity (phonon) k_n.

Table 1.3 reveals thermoelectric parameters in the materials. It demonstrates that semiconductors are the most appropriate material to choose for thermoelectric materials and that these characteristics can be engineered with the intention of boosting the thermoelectric material's performance in the semiconductors.[54]

TE parameters → Materials ↓	Electrical conductivity σ	Seebeck coefficient S	Thermal conductivity k
Metal	Very High ~10^7 Sm^{-1} ↑	Low ~ 10μVK^{-1} ↓	High ~10^2 $Wm^{-1}K^{-1}$ ↑
Insulators	Extremely low ~$10^{-10}Sm^{-1}$ ↓	High ↑	Low ~10^{-2}-10^{-4} $Wm^{-1}K^{-1}$ ↓
Semiconductors	Moderate $10^{-3}Sm^{-1}$ ↑	High ~120 μVK^{-1} ↑	Low ~10 $Wm^{-1}K^{-1}$ ↓

Table 1.3: The thermoelectric properties of bulk metals, semiconductors and insulators[54]

A variety of thermoelectric materials have been developed, which are used in thermoelectric devices. Most of the thermoelectric materials have temperature-limited operations at certain temperatures. In order to have a high net Seebeck coefficient, it is vital to develop single thermoelectric materials (P-type or N-type). N- and P-type materials developed for semiconductors are illustrated in Figure 1-11.[12]

(Bi, Sb)(Te, Se) are the most familiar commercial thermoelectric materials employed in thermoelectric devices. Tellurium (Te), which is known to be toxic, is one of the scarcest elements on the planet, which makes its applications expensive and less sustainable for large appliances. The material works at room temperature, given that it does not function at a high temperature. In addition, at a higher temperature above 800 K SiGe alloys produce an improved performance.

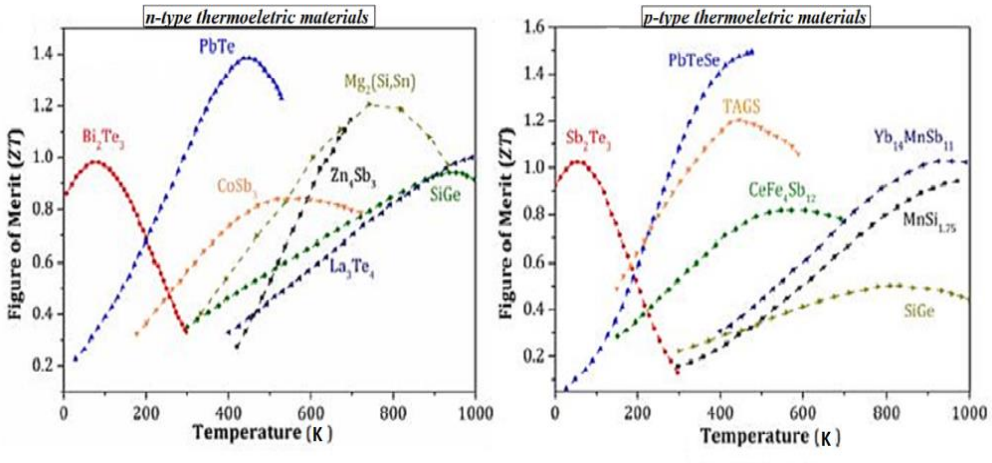

Figure 1. 11: N-type and P-type semiconductor materials[15, 17, 21]

1.8 The thermoelectric figure of merit. How it can be improved?

The main challenge in developing thermoelectric materials with a high figure of merit is to connect the thermoelectric parameters. There are a number of approaches used to enhance the figure of merit, such as doping with certain materials, nanostructuring, alloying and introducing porosity inside the material.

Alloying is one of several methods employed with the aim of improving the figure of merit in thermoelectric materials over an extensive period of time. Atomic-scale defects in alloying materials will scatter phonons and, resulting in reduced thermal conductivity. This method is reaching its limit and reducing thermal conductivity further by alloying is almost impossible.[55]

Another successful method to increase ZT can be achieved by means of controlling the lattice thermal conductivity, as this is the only parameter not influenced by the electronic parameters of the material**.**[56]

The denominator of the figure of merit ZT is thermal conductivity for which, in general, $k_l \gg k_{ele}$ is true in semiconductors.[56] It should be mentioned that the lattice thermal conductivity is relative to the mean free path of phonon scattering. Electron scatter from defects, phonons, roughness and boundaries, and any minute change in these factors can enhance ZT and feasibly reduce thermal conductivity. The differences in thermal conductivity in the materials is illustrated in Figure 1-12. In the case of a semiconductor, the graph

confirms that virtually all of the heat is conveyed by phonons and the thermal conductivity is reducing in the metal.[57]

Therefore, the ZT can be developed by means of:

- Enhancing the power factor $S^2\sigma$ (thermo power), or by way of
- Lowering the thermal conductivity k

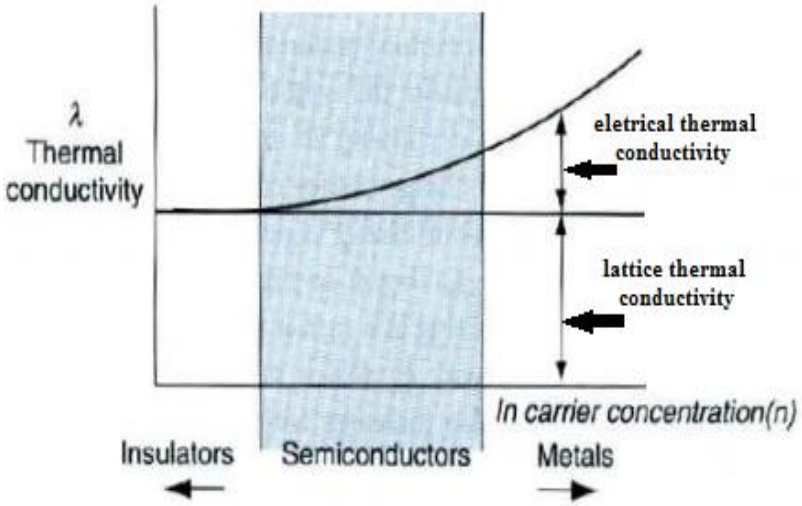

Figure 1. 12: Thermal conductivity variation in the materials [57]

Table 3 shows the consequences of lattice thermal conductivity on the thermoelectric material's performance. Here, the comparison is undertaken between the N-type and P-type Bi_2Te_3 with bulk Si and Ge at 300 K.[58-59] In Table 3, virtually all of the materials have the same doping concentration at the same temperature of 300 K. The electrical resistivity in Si and Ge is not too different from that of the Bi-Te components. In addition, most of the change is caused by the huge difference in thermal conductivity.

Bi_2Te_3 demonstrates a narrow band-gap, whilst the mean free path is also very small (Λ =15 nm at 300 K). Thus, these characteristics produce thermal conductivity which is extremely low and as a result, increase the figure of merit. In the case of silicon, this material has a similar mean free path (Λ =14 nm at 300 K) but a wide band-gap, which produces thermal conductivity 74 times greater than that of Bi_2Te_3.[58-59]

Material (300 K)	N (cm^{-1})	ρ (Ωm)	α (μVK^{-1})	k (WKm^{-1})	ZT(300 K)
N-type					
n-Bi_2Te_3 (31)	-	1.6×10^{-5}	-160	2.0	740×10^{-3}
n-Si (32)	1.0×10^{19}	6×10^{5}	-95	148	31×10^{-5}
n-Ge (33)	1.1×10^{19}	1.5×10^{-5}	-308	59.9	32×10^{-3}
P-type					
p-$(BiSb)_2Te_3$ (31)	-	1.2×10^{-5}	175	2.0	675×10^{-3}
p-Si (32)	1.5×10^{19}	9×10^{-5}	148	148	49×10^{-5}
p-Si (34)	1.0×10^{19}	2.8×10^{-5}	280	59.9	14×10^{-3}

Table 1.4: Comparison of the thermoelectricity of the three materials[58-59]

There is an improvement in ZT due to the nanostructuring of this material. Thus, nanostructuring improves the density of the state (DOS) adjoining the Fermi level by means of quantum confinement and, therefore, enables the thermopower ($S^2\sigma$) to increase. Furthermore, as the average free path of the electron is small in contrast to that of the phonons in semiconductors, which are heavily doped, the nanostructuring creates a large density of interface, where phonons over a large average free path range can be dispersed more efficiently and favourably contrary to the electrons. Therefore, the lattice thermal conductivity is reduced, whereas the electronic conduction and carrier mobility is maintained.[60-65] Furthermore, the nanostructuring of materials has increased ZT in numerous materials, as indicated in Table 2.

Certain materials, for example bulk lead telluride (PbTe)-based materials, PbTe/PbSeTe quantum dot superlattices, BiTe/SbTe superlattices, and, recently, Si nanowires and BiSbTe composite structure have created significant enhancements in ZT due to reductions in thermal conductivity by means of phonons scattering due to nanostructuring.[65] A high ZT value up to 2.4 has been observed in Bi_2Te_3/Sb_2Te_3 superlattices.[66] In addition, PbTe/PbTeSe quantum dot superlattices that comprise values of ZT greater that 3.0 at 600K have been reported.[67]

Figure 1-13 illustrates recent figures of merit for high performance thermoelectric materials related to nanoengineering.[68] Figure 1-13 is verbatim the same as figure 2 in reference 70. In the case of SiGe alloy, nanoengineering improves the performance of the thermoelectric material. Consequently, the ZT has improved from 0.2 to 1.4 K at 1200 K.[69]

As an example, Bi_2Te_3 base film is confirmed as having a thermal conductivity of 0.3-0.4 $Wm^{-1}K^{-1}$ that is 25% lower than the bulk.[66] Furthermore, silicon nanowire 10-20 nm thick exhibits low thermal conductivity with a $k_{bulk}/k_{nanowire}$ ratio, which is noted to be as high as 25–150 at room temperature.[59]

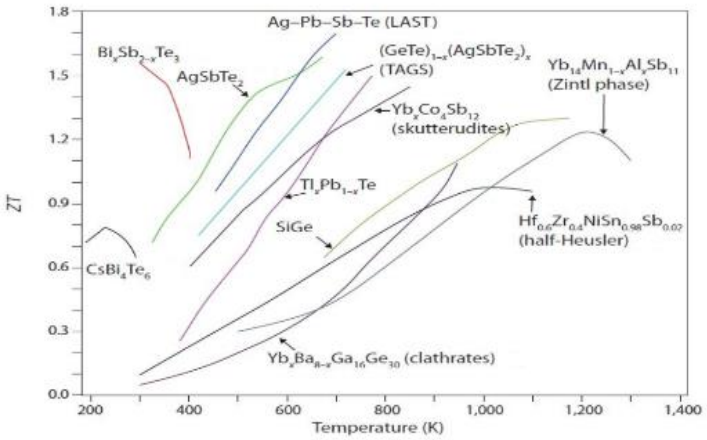

Figure 1. 13: ZT as a function of temperature for nanoengineered thermoelectric materials [70]

Apart from nanostructuring, by introducing porosity in the thermoelectric materials, thermal conductivity can be decreased considerably. The main mechanism to lower thermal conductivity in porous materials is by scattering the phonons with pore boundary. In addition, the number of pores, as well as their size, shape and orientation influence thermal conductivity.[71]

The influence of porosity on the thermoelectric properties of Bi_2Te_3 has been extensively reported. Figure 1-14 reveals the effect of porosity on its ZT. The study demonstrates that the introduction of porosity results in, reduced lattice thermal conductivity and electrical resistivity, as well as an improved figure of merit.[72]

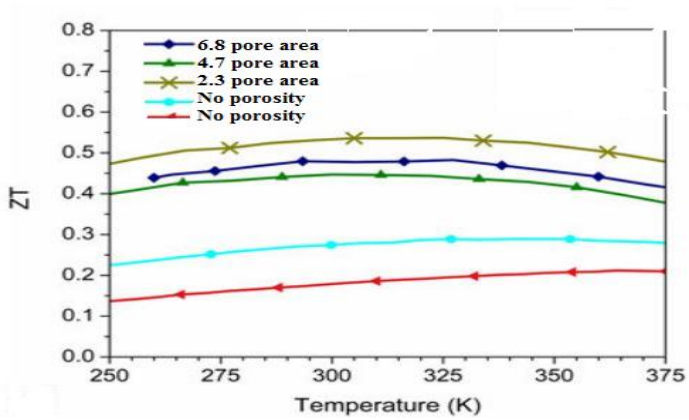

Figure 1. 14: ZT for Bi_2Te_3 pore material with different values of porosity [72]

Overall, the figure of merit will increase by ensuring that the thermal conductivity is lowered. However, the optimisation of porosity is required so as to accomplish the most appropriate figure of merit. In the case of Bi_2Te_3, which is a nanoporous structure, a value of porosity of 2.30% could improve the ZT. The maximum figure of merit for this material is 0.54 at 325 K.[72] A theoretical investigation in relation to the material porosity and pore surface roughness of silicon nanomeshes has been conducted. At room temperature, a porosity of 50% results in a reduction of 80% in thermal conductivity. Furthermore, the pore boundary also reduces thermal conductivity; however, its influence is weak.[71]

Mesoporous ZnO thin films are synthesised by using the aerogel technique and their porosity increased from 29-40%. The electrical and thermal conductivity and Seebeck coefficients signified a close correlation with the porosity of the thin films, indicating that the thermoelectric properties can be changed by altering their porosity. The mesoporous ZnO thin films with the highest porosity examined had the best thermoelectric properties (the lowest thermal conductivity and the highest Seebeck coefficient).[73-74]

Discussion has taken place concerning the effect of nanoscale porosity on the thermoelectric properties of SiGe.[75] The results indicate that porosity often results in smaller values of ZT in SiGe due to a reduction in electrical conductivity. The thermal conductivity of CoSi has been determined to decrease with the introduction of porosity and is also influenced by the numbers of pores. However, electrical conductivity decreases as the porosity increases, due to the scattering of electrical conductivity.[76]

1.9 Thesis Motivation

The characterisation of thermoelectric materials of submicron scale is a challenging task. The Seebeck coefficient, thermal conductivity and electrical resistivity perimeters signify the performance and quality of the material. Therefore, precise and accurate measurement is essential for any electronic device. In this thesis, the thermoelectric characterisation of Zn_4Sb_3 material and silica aerogel using different techniques is discussed. In particular, the scanning thermal microscopy technique is used to examine thermal conductivity and the technique is discussed in detail. The effect of SThM probe thermal conductance on thermal conductivity measurements has been experimentally determined. Likewise, a specific method has been created with the intention of measuring the Seebeck

coefficient utilising SThM. The proposed technique is used to examine the Seebeck coefficient measurements of samples.

Silica aerogel is of interest owing to its minimal thermal and electrical conductivity. Engineering the material properties of silica aerogel can alter its electrical and thermal conductivity. This has led to the synthesis of silica aerogel embedded with Zn_4Sb_3 thermoelectric material in this study. The thermoelectric properties of the synthesised material have been examined using different techniques, which represents a promising route to improving its properties. In addition to that, the thermoelectric characterisation of silica aerogel embedded with nickel nanoparticles has been examined which also shows that it is a promising material.

1.10 Thesis outline

In Chapter 2, a brief summary of the measurement techniques is given. Standard results on known samples are also presented. Chapter 3 thermal conductivity measurements using scanning thermal conductivity (SThM) are discussed. The results are compared with thermal conductivity measurements using different techniques. In addition, the effect of SThM probe thermal conductance on thermal conductivity is discussed. Chapter 4 presents the characterisation of the thermoelectric properties of silica aerogel embedded with nickel nanoparticles (NiNPs), while Chapter 5 describes the synthesis of silica aerogel embedded with Zn_4Sb_3 as a thermoelectric material. In addition, the thermoelectric characterisation of the synthesised sample is presented.

Chapter 2

Experimental Techniques

2.1 Introduction

This chapter examines the experimental approaches to characterise materials in this PhD. In order to evaluate the performance of materials, accurate characterisation is necessary. In particular, the characterisation of individual parameters in the figure of merit at different temperatures is essential.

The Peltier coefficient, Seebeck coefficient and electrical conductivity, in addition to the electronic and lattice thermal conductivity are the four variables in the determination of the ZT.[77]

$$Z = \frac{S^2\sigma}{k_l + k_e} \qquad \text{Equation 2-1}$$

The electrical characterisation of the material uses the Van der Pauw structure on a four-probe station and the Hall effect to be measured. The thermal conductivity of the samples is measured using scanning thermal microscopy, a HotDisk analyser and Raman-temperature spectroscopy. Here, by applying the Wiedemann-Franz law ($k = \sigma LT$), the electronic thermal conductivity is estimated. With regards to the properties of the thermoelectric materials, the figure of merit is a temperature dependent quantity.

The Peltier and Seebeck coefficients are related to the Kelvin relation, and thus there is no need to measure them separately.

To obtain accurate results, electrical and thermal characterisation must be completed carefully, as several factors can affect the results, as discussed below. Since all of the parameters in the figure of merit are temperature-dependent, they can be multiplied by absolute temperature in an attempt to make the result dimensionless. Material composition is analysed using Raman spectroscopy, where the electrical resistivity is assessed using the four-point probe technique.

2.2 Electrical characterisation

The primary equation for diffusive transport is: [78]

$$J_{nx} = \sigma_n \frac{d\left(E_F/q\right)}{dx} \qquad \text{Equation 2-2}$$

where σ_n is conductivity and E_F is quasi-fermi level. By solving the Boltzmann transport equation[78], a standard result is predictably obtained.

The subscript n indicates that it is an N-type material and it is assumed that a similar equation can be considered for P-type materials. Under a uniform carrier density, $d(E_F/q)/dx = \varepsilon_x$, [78-79] and:

$$J_{nx} = \sigma_n \varepsilon_x \qquad \text{Equation 2-3}$$

$$\varepsilon_x = \rho_n J_{nx} \qquad \text{Equation 2-4}$$

where, ε_x is the electric field and σ_n is electrical conductivity. For a diffusive sample, resistivity depends on the material and not on the dimensions of the sample.[79] The units of the current density and resistivity of 1D, 2D and 3D samples are as shown in table 2.1:

Dimension	ε_x	J_{nx}	ρ_n
1D	$\mathrm{Vm^{-1}}$	A	$\Omega\mathrm{m^{-1}}$
2D	$\mathrm{Vm^{-1}}$	$\mathrm{Am^{-1}}$	Ω
3D	$\mathrm{Vm^{-1}}$	$\mathrm{Am^{-2}}$	Ωm

Table 2.1: The units of current density and resistivity depending on dimensionality

The resistivity of the material is frequently established by means of applying the 4-probe method. In this procedure, two probes are utilised to measure the voltage, whilst the two remaining probes are employed to assess the current. The four-probe method is able to eradicate measurement errors attributable to probe resistance, the contact resistance between each metal probe, in addition to the material and the spreading resistance under each probe. In this technique, a high impedance voltmeter obtains a slight current. Hence, the voltage

throughout the probe resistance is reduced, increasing the contact resistance and resistance that are extremely small.

2.2.1 Four-probe resistivity measurement

The electrical current equation is:[79]

$$J_{nx} = \sigma_n \varepsilon_x \qquad \text{Equation 2-5}$$

The subscript n indicates an N-type material, but similar considerations also apply to p-type materials. Resistivity is generally measured because it depends on the material and not the dimensions of the resistor.

Electrical conductivity is measured by applying the Van der Pauw technique to obtain electrical resistivity. Moreover, two different measurement systems are used in this study: Hall equipment and four probe measurement (CASK4200 equipment).

The CASK4200 allows the measurement of resistivity in the absence of a magnetic field; however, in the case of the Hall equipment, by applying a magnetic field, resistivity, carrier density and mobility can be measured. The advantage of using the Van der Pauw technique to measure resistivity is that it allows problems due to sample geometry to be avoided.[80-81] In this technique, sheet resistance, carrier density, carrier type and the mobility of major carriers can be determined.[80]

In the technique, four contacts are provided on the edges of the sample. The contacts are sufficiently small.

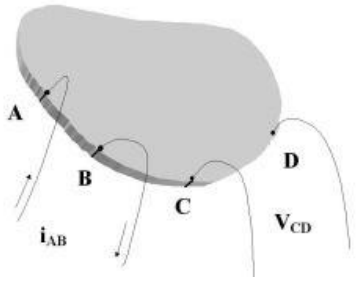

Figure 2. 1: Van der Pauw structure [79]

The effects of contact on the edges of the resistivity sample can be obtained by: [78-79]

$$e^{\left(-\pi\frac{R_{AB,CD}d}{\rho}\right)} + e^{\left(-\pi\frac{R_{BC,AD}d}{\rho}\right)} = 1 \qquad \text{Equation 2-6}$$

where d is the thickness of the sample and:

$$R_{AB,CD} = \frac{V_D - V_C}{i_{AB}} \qquad \text{Equation 2-7}$$

$$R_{BC,AD} = \frac{V_A - V_D}{i_{BC}} \qquad \text{Equation 2-8}$$

Here I_{AB} is the current fed to the sample from contact A and drained from contact B. If all of the contacts are symmetrical, resistivity can be calculated from:

$$\rho_1 = \frac{\pi}{2ln2}\frac{R_{AB,CD}+R_{BC,AD}}{2} \qquad \text{Equation 2-9}$$

$$\rho_2 = \frac{\pi}{2ln2}\frac{R_{CD,AB}+R_{AD,BC}}{2} \qquad \text{Equation 2-10}$$

Therefore:

$$\rho = \frac{\rho_1+\rho_2}{2} \qquad \text{Equation 2-11}$$

The resistivity, carrier density and mobility of a material can be measured using the Hall effect measurement technique.[81] In this technique, by applying a *z*-direction magnetic field B_z, forcing a current to contact A and C whilst measuring the voltage between the other two, B and D reverse the direction of the magnetic field and once more measure voltage between the same contacts. The average of the two measured voltages is the Hall voltage V_H:

$$V_H = B_z I / n_s te \qquad \text{Equation 2-12}$$

Where I is electrical current, t is the thickness of the conductor and e is te electron charge. The Hall coefficient r_H, Hall concentration n_H, charge concentration n_s and J_x is current desnsity u_s can subsequently be determined from the Hall voltage:[81]

$$r_H = \frac{E_z}{J_x B_z} \qquad \text{Equation 2-13}$$

$$n_H = r_H n_s \qquad \text{Equation 2-14}$$

$$r_H = 1/en_H \qquad \text{Equation 2-15}$$

The dependence of electrical resistivity with temperature illustrates the influence of scattering on the carrier mobility within the materials. Typically, mobility increases as the temperature rises; subsequently, at a certain temperature, the mobility will begin to decrease. These changes in mobility are attributed to charge impurity scattering and phonon scattering respectively.[83] The important point as regards mobility when it increases with increasing temperature, is that it indicates the presence of impurity-dominated scattering, whereas when mobility decreases with increasing temperature, this signifies increasing phonon scattering.[83]

2.3 Thermal characterisation

Measuring thermal conductivity is a challenging task. In this case, the challenge occurs owing to the problem associated with performing the measurement, besides the microstructural differences in subtle characteristics, for instance grain orientation, porosity, the size of the defect, in addition to the impurity levels between the materials.[82-83]

Many techniques exist to determine the thermal conductivity of material, for instance the thermal diffusivity method. This method has advantages and, in addition, some limitations.[84-86]

Thermal conductivity was investigated and measured using three different methods: scanning Thermal Microscopy, micro Raman spectroscopy and HotDisk analyser. These methods enable thermal conductivity to be investigated at submicron scale. In particular, SThM is a useful tool that can capture both the bulk and nanoscale properties of materials.

2.3.1 Scanning thermal microscopy (SThM)

An atomic-force-microscopy (AFM) probe is utilised with the purpose of scanning sample top surfaces to generate images with vertical and horizontal resolution down to the nanoscale range.[87-88] The AFM comprises a cantilever which has a sharp tip positioned at its end. Additionally, a laser diode points towards the end of the tip and subsequently creates reflection of the light from the cantilever to a sensitive deflector. The instrument operates by

way of determining the deflection which takes place on the tip while it is scanning the surface of a substrate, where this particular deflection is identified by the change in the reflected light.[89-90] A schematic diagram of an AFM is shown in Figure 2-2.

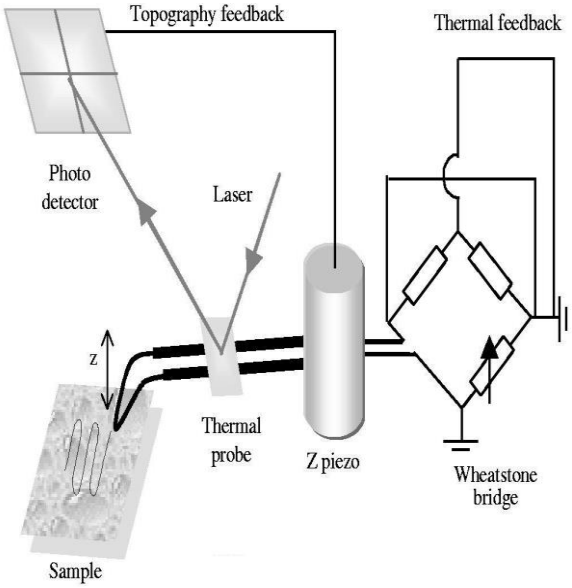

Figure 2. 2: Schematic diagram of an AFM[89]

In regard to the scanning thermal microscopy, the AFM equipment uses a special cantilever to calculate the thermal conductivity or the local temperature of an interface. The SThM technique plots the thermal properties of the sample surface by means of utilising a thermal probe that includes a resistive element.[90] It should be noted that the SThM exists in two modes, thermal contrast microscopy (TCM) and thermal conductivity contrast microscopy (CCM).[91] TCM permits the variations in temperature on a sample surface to be determined, whilst CCM enables the user to calculate variations in thermal conductivity in a sample surface.

The tip of the SThM is the principal part of SThM measurement. It performs concurrently as a resistance thermometer (or a heater in the CCM mode) and as a contact AFM tip. SThM probes used previously provided insufficient spatial and thermal resolution and moreover, were seriously restricted by the geometry of a wire-based thermal probe, for instance Wollastone wire.[92]

The XE-Series SThM makes use of a nano-fabricated thermal probe where a resistive element is lithographically patterned on to the tip of the AFM. The tip of the radius of the nanofabricated probe is below $100\ nm$, allowing high resolution thermal image scanning, whereas the Wollaston wire probe is greater than several hundred nm.[93]

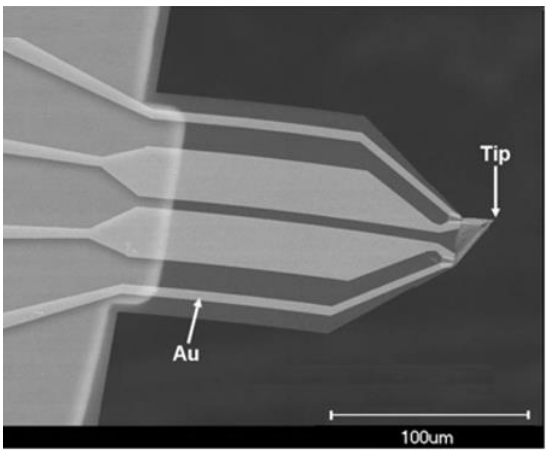

Figure 2. 3: SEM image of the Nanothermal probe [93]

The specifications of the nanothermal probe are listed in Table 2.2 in detail.

Nanothermal probe properties	Specification
Cantilever base	Silicon
Cantilever dimension	150 μm × 60 μm × 1 μm
Tip height	~12 μm
Tip radius	≤ 100 nm
Resistance	200~600 Ω
Thermal coefficient of resistivity	~1 Ω $°C^{-1}$
Maximum recommended current	2 mA
Maximum recommended temperature	200 °C
Normal spring constant	~0.45 Nm^{-1}
Normal resonant frequency	~48 kHz

Table 2.2: Specification of nanothermal probe

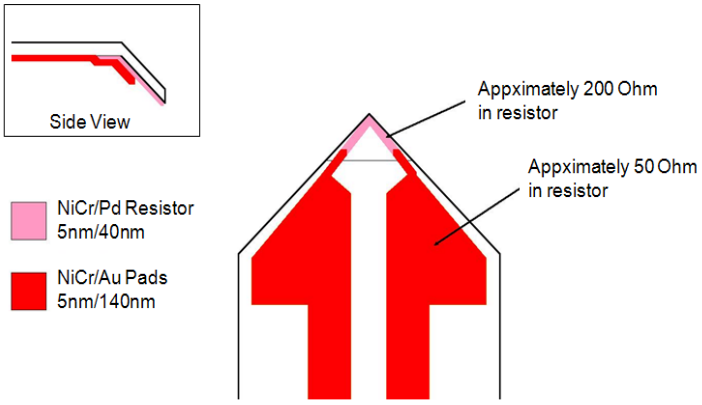

Figure 2. 4: Scanning thermal microscopy probe[91]

In the TCM approach, the resistive element of the thermal SThM probe is employed as a resistance thermometer. Its temperature varies as the tip scrutinises the surface in relation to the temperature of the surface. The alteration in the temperature of the resistive element produces a change in its resistance. Moreover, the temperature of a very small region can be measured by way of passing a continuous current through the tip and calculating the resistance.

To recognise the change in tip resistance, it is created to be a part of the Wheatstone bridge circuit as Figure 2-5 illustrates. Furthermore, a continuous current, known as the probe current is distributed to the bridge.

Initially, the tip is placed in thermal equilibrium together with the sample surface, which results in constant resistance. The variable resistor located in the bridge is subsequently modified, with the aim of making the potential difference between Points 1 and 2, zero. Afterwards, the probe's temperature is noted to alter as the probe inspects the surface. The equivalent change in probe resistance will modify the voltage balance of the bridge and as a result, modify the voltage difference between Points 1 and in Figure 2-5. This process is known as the SThM error and subsequently employed to produce the SThM image in the TCM mode.[91]

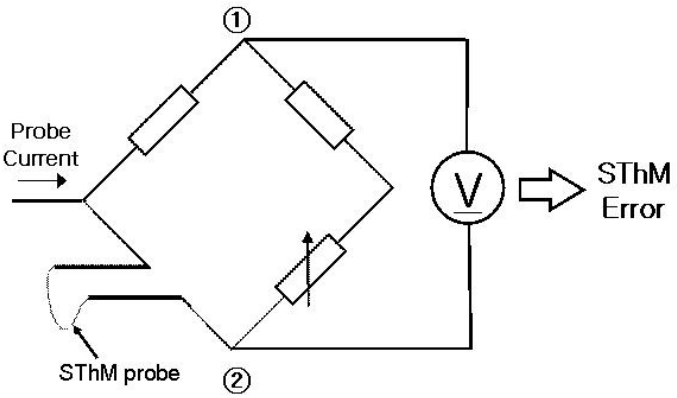

Figure 2. 5: The SThM probe is part of the Wheatstone bridge[92]

In this case, so that no self-heating of the probe arises, the current passed through the probe in TCM is established to be small enough. This is for the reason that resistance change attributable to self-heating would trigger errors in temperature measurement. Likewise, in the TCM method, the scanning speed is restricted by the time it takes the tip to achieve thermal equilibrium with the surface of the sample.[91-93]

In CCM, the thermal SThM probe's resistive element is operated as a resistive heater. Figure 2-6 illustrates a schematic diagram of SThM in CCM. To preserve the tip of the probe at a set temperature via a feedback loop, an adequate amount of energy is applied. The energy that is essential to maintain the set temperature signifies the local thermal conductivity.[93-94]

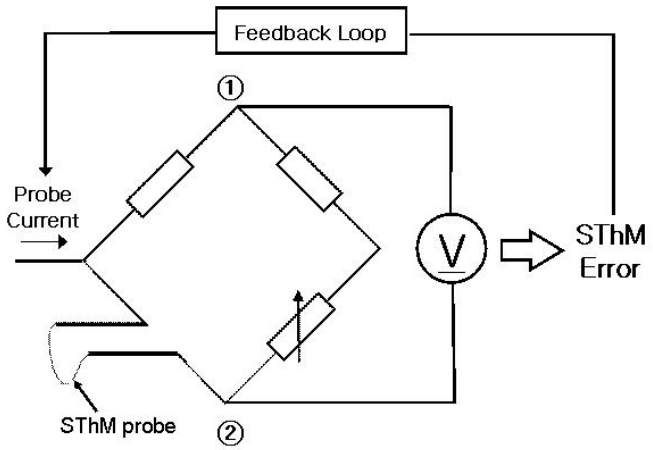

Figure 2. 6: SThM probe as part of the Wheatstone bridge circuit comprising a feedback loop to modify the probe current so that it is maintained at a constant temperature[92]

In the CCM approach, the control circuit makes use of a feedback loop to alter the current of the probe applied to the bridge, with the intention of sustaining the probe at a temperature that is constant.

Originally, the tip is in thermal equilibrium with the surface of the sample. The energy which is delivered to the tip by the probe current equates to the heat (energy) emanating from the tip by way of heat conduction between the tip and the surface of the sample.

The following three factors control the flow of the heat:[94-96]

- The probe's contact area
- Temperature difference between the probe and the sample
- Thermal conductivity of the sample

If the sample is flat enough and allows the contact area of the probe to remain constant and moreover, the sample is at a continuous temperature, where the difference in temperature between the probe and the sample stays constant, given that the probe's temperature is maintained at a constant level via the feedback loop, the difference in thermal conductivity of the surface material can be verified by way of calculating the modification in heat flow from the probe to the surface.

In other words, heat flow changes cause the probe temperature to change. Then, a corresponding resistance change alters the balance of the bridge and then the generation of the SThM error signal. The feedback loop detects the error signal and alters the probe current to cancel out the error signal. The probe current, via a feedback loop, decreases or increases the energy provided to the cantilever tip to maintain a constant temperature and therefore a constant resistance. The distribution of thermal conductivity on the sample surface is determined according to the change in probe current.[97-100]

2.3.2 Raman spectroscopy

Raman spectroscopy is an effective and extremely influential analytical process that provides information at a molecular level. In this process, the interaction of electromagnetic radiation with matter, primarily the scattering of light in addition to a specific emission, delivers information regarding chemical agents that is crucial.[101] Moreover, within a wide range of scientific disciplines, Raman spectroscopy is an essential device in obtaining such corroboration. This method permits the rapid detection of materials and gives valuable

information concerning rotational and vibrational transitions and also provides data on the structure of the material, structural analyses and spatial arrangement of the molecules.[102]

In relation to Quantum theory, the energy of photon E is given by equation 2-16:[101-102]

$$E = h\nu = hc\bar{\nu} \qquad \text{Equation 2-16}$$

where h is Planck's constant, ν is its frequency and $\bar{\nu}$ is the wavenumber. The specific energy ΔE has to fulfil the quantum condition that follows:

$$\Delta E = |E_p - E_q| = \lambda\nu = {}^{hc}/_{\lambda} \qquad \text{Equation 2-17}$$

where E_p and E_q are energies of different quantum states, where a molecule can occur, c is the velocity of light and λ is the wavelength. Therefore, the energy of a molecule will be altered by an amount E, if the discharges the photon.

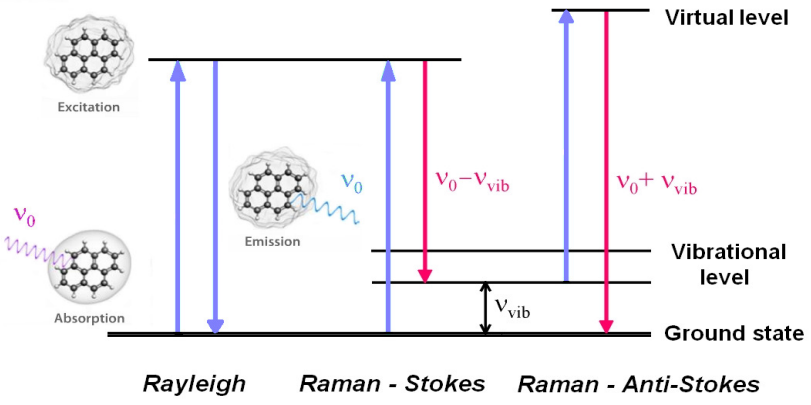

Figure 2. 7: Energy level diagram for Raman scattering, Stokes scattering and anti-Stokes scattering [101]

The Raman effect occurs when intense monochromatic light irradiates a piece of material as shown in figure 2.7. A significant part of the light beam, typically from the near-infrared, visible or near-ultraviolet range is dispersed without any changes in frequency. Consequently, no energy is lost or gained. Specifically, a part is absorbed in Rayleigh (elastic) scattering, which is vital for the origin of the spectra, is dispersed non-elastically. Once the photon interacts with the molecule, principally with the bonds of the molecule and the

electron cloud, the photon induces molecule excitation from the ground state to a virtual energy state. When the molecule slows down, it produces a photon and subsequently, goes back to a different rotational or vibrational state. The energetic difference between the ground state and the final state creates a shift in the released photon's wavelength.[102]

Raman shifts is dependent on the specific molecular geometry of the material and are autonomous of the incident photon's wavelength; that is, of the excitation wavelength of the laser.

Raman spectrum signifies the requirement of intensity of the scattered light (in arbitrary units) on wavelength or on a Raman frequency shift (measured in cm^{-1}**).** The intensity of Raman scattering is subject to various factors, for instance the excitation wavelength of the laser employed, the excitation power applied, the volume of Raman active molecules lit by the laser beam, as well as the temperature.[102]

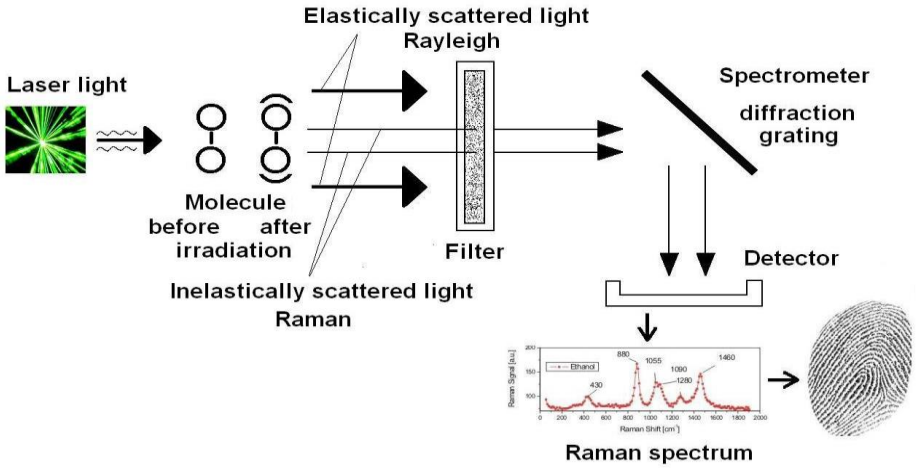

Figure 2. 8: Raman spectroscopy: principle and detector set-up[102]

2.3.3 Temperature-dependent Raman spectroscopy

The non-contact and direct method applied in the measurement of thermal conductivity is based on micro-Raman spectroscopy. In this system, a laser beam is focused accurately on the sample and collects scattered phonons due to phonon-phonon scattering with lattices. This scattering is known as Raman scattering. Furthermore, temperature information can be obtained by the shifting of the Raman peak due to thermal expansion.[94-95]

In relation to Raman spectroscopy, this technique is based on two things. First, local heating due to the laser beam concentrating on the sample, is directly related to the thermal

conductivity of the sample. Secondly, the change in the Raman peak by means of temperature can be applied to assume the local temperature increase.[95]

The straightforward linear relationship between heating power P and the local temperature of the sample creates its thermal conductivity. Furthermore, calibration at low laser power P is required so that no additional temperature will be induced. This is essential to associate the Raman peak position to the local temperature. Subsequently, at any given laser power, the extent of the Raman peak position is related to the increase in the temperature locally and produces the determination of the thermal conductivity of the material.

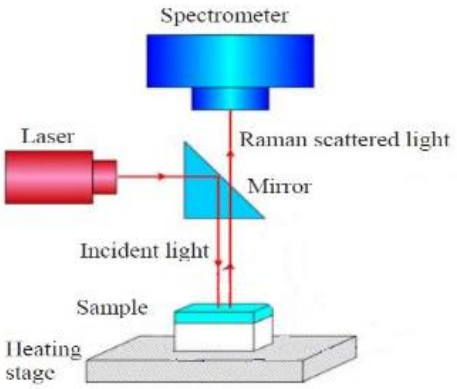

Figure 2. 9: Schematic diagram of the micro-Raman method [96]

As shown in Figure 2-9, when a laser beam is treated with radiation and concentrated on the sample, the temperature will increase at the place where the beam strikes the surface. The increased temperature is precisely associated with the thermal conductivity of the sample. The shift in Raman peak in conjunction with the temperature can be utilised to determine the difference in the increase in local temperature. In addition, a simple relationship between laser power and local temperature can be used to extract thermal conductivity:

$$k = \frac{2P}{\pi a\,(T_s - T_r)} \qquad \text{Equation 2-18}$$

where

P= the power of laser in Watts

a = diameter of the heating source

T_s = local temperature on the sample

T_r = bulk temperature (ambient temperature)

In this method, the sample is heated from 20 ℃ to 150 ℃ during the heating stage. The Raman calibration equation explains the relationship between the Raman peak position and temperature at low laser power. The calibration needs to be performed at low laser power in order to ensure that additional heat is not introduced into the sample. The position of the Raman peak needs to be plotted against the temperature to extract the Raman calibration equation.

The Raman measurement of porous silicon with a porosity of 64% and thickness of 93 μm was found.[96] The sample was heated from 100 to 500 ℃ with intervals of 100 ℃ using a heating stage. The power of the laser beam at this point was 1.8 mW so as to make sure that the temperature did not increase. The Raman measurement was performed at five different temperatures and the results are illustrated in Figure 2-10.

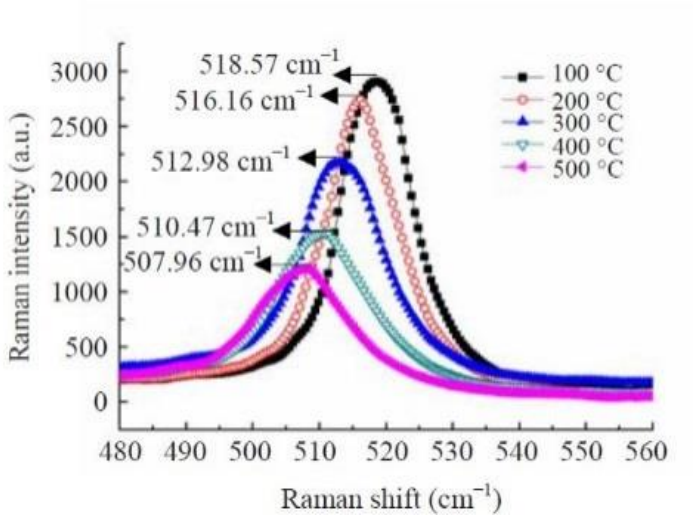

Figure 2. 10: Raman spectra and the peak positions of porous silicon at various temperatures [96]

The linear correlation between the Raman peak position of the sample tested and the temperature is described in Figure 2-11. Consequently, it can be seen that the Raman peaks position drops as the temperature increases.

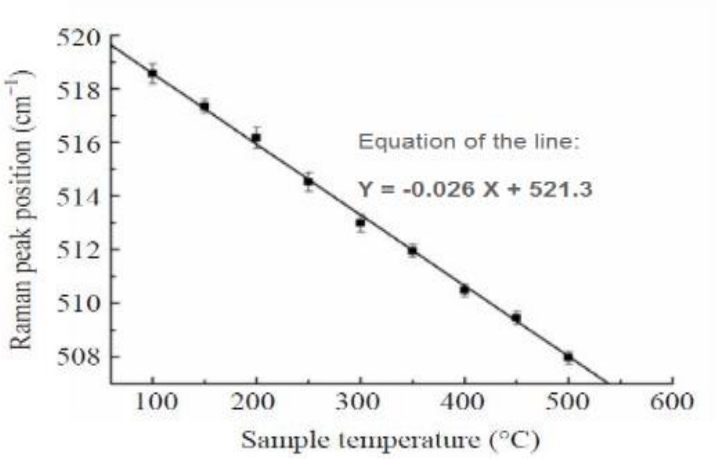

Figure 2. 11: Raman peak position vs. the temperature of porous silicon at a low laser power of 1.8 mW [96]

The line equation such as the one shown in Figure 2-18 can be extracted from Raman peak position versus temperature. By performing the Raman measurement with laser power which is higher, the line equation is used to extract the corresponding local temperature (T_s) on the sample with a different laser power. The T_s is substituted in Equation 2-16 to extract the sample's thermal conductivity. Here, the thermal conductivity of the porous silicon sample with a porosity of 64% is 0.85 W m^{-1} K^{-1}.[96]

An alternative way to measure thermal conductivity by Raman spectroscopy is via the intensity ratio (anti-Stokes/Stokes ratio).[97-98] If the system is in thermal equilibrium, the relative occupation of the excited states and ground states can be derived from the Boltzmann distribution:

$$\frac{I_S}{I_{AS}} \propto e^{\frac{h\nu_1}{K_B T_S}} \qquad \text{Equation 2-19}$$

where

I_{AS}= anti-Stokes Raman shift

I_S = Stokes Raman shift

K_B= Boltzmann constant

$h\nu_1$ = energy gap between the excited and ground states

T = absolute temperature

The frequency dependence of Stokes and anti-Stokes Raman scattering is described as:

$$I_s \propto \nu_0(\nu_0 - \upsilon_1)^3 \qquad \text{Equation 2-20}$$

$$I_{As} \propto \nu_0(\nu_0 + \upsilon_1)^3 \qquad \text{Equation 2-21}$$

where

υ_0 = frequency of exciting laser beam,

$\nu_0 \pm \upsilon_1$= frequency of Raman Stokes (- sign) and anti-Stokes (+ sign) band

A combination of the Boltzmann distribution and frequency dependence gives:

$$I_S/I_{AS} = \frac{(\nu_0-\upsilon_1)^3}{(\nu_0+\upsilon_1)^3}\, e^{\frac{h\upsilon_1}{k_B T_S}} \qquad \text{Equation 2-22}$$

where

T_s = local temperature of the sample which has increased due to the laser power.

By using Equation 2-19 and substituting T_s, the sample's thermal conductivity can be removed.

2.3.4 HotDisk analyser

The HotDisk is also employed to establish the samples' thermal properties. In this method, a disk sensor is located between two samples. Subsequently, it is heated by way of a continuous electrical current for a short period. The heat that is produced disperses from the sensor into the immediate unknown sample material, which generates a temperature increase and the sensor. The mean rises in the transient temperature of the sensor, in the region of 0.5K- 5K, is calculated at the same time by means of monitoring the difference in electrical resistance.[99]

The temperature coefficient of the sensor material's resistivity is the relationship related to the change in resistivity with the corresponding variation in temperature. In order to avoid any influence from outside the lateral boundaries of the sample, the time duration of the heating current is typically restricted by the sample size. Furthermore, if the sample is greater than the diameter of the sensor, the probing depth of the heating (thermal penetration depth) should be of an equivalent magnitude as the radius of the Hot Disk sensor. Consequently, this guarantees the stable values of diffusivity and thermal conductivity.[99]

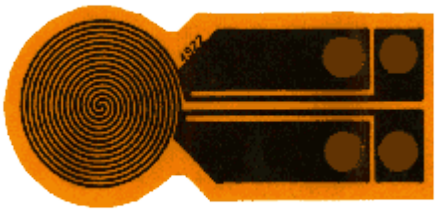

Figure 2. 12: Hot Disk sensor with a diameter of 5mm [100]

In this experiment, the HotDisk TPS 2500 S model was employed. The device specifications can be seen in Table 2-3:[100]

Thermal conductivity	0.005 to 1800 $Wm^{-1}K^{-1}$
Thermal diffusivity	0.1 to 1200 mm^2s^{-1}.
Specific heat capacity	Up to 5 $MJm^{-3}K^{-1}$.
Measurement time	1 to 1280 seconds.
Reproducibility	Typically, better than 1 %.
Accuracy of measurement	Better than 5 %
Temperature range	-253 °C to 1000 °C.
With furnace	Ambient to 750 °C [1000 °C oxygen free].
With circulator	-35 °C to 200 °C
Smallest sample Dimensions	0.5 mm × 2 mm diameter or square for bulk testing. 0.1 mm × 10 mm diameter or square for slab testing. 10 mm × 5 mm diameter or square for one-dimensional testing.
Sensor types available	All Kapton sensors. All Mica sensors. All Teflon sensors.

Table 2.3: Specification of the HotDisk analyser

2.4 Characterisation of material composition

The composition of the materials has an effect on their physical utility properties and therefore, their electrical and thermal characteristics. This section describes the tools used to examine and identify the composition of the materials.

2.4.1 X-ray diffraction

For the identification of unknown crystalline materials, for example minerals or inorganic compounds, a powerful tool known as X-ray powder diffraction (XRD) is used. The identification of unknown solids is significant in relation to studies in geology and environmental science.[103] XRD is also used for the characterisation of crystalline materials, and the identification of fine-grained minerals such as clays, the determination of unit cell proportions.

X-rays are created in a cathode ray tube by means of heating a filament to deliver electrons, which are accelerated in the direction of a target by an elastic field. The target material is showered with electrons. It can be seen that characteristic X-ray spectra are created when the electrons have sufficient energy to dislodge the inner shell electrons of the target material.[103]

Next, the X-rays are focused onto the sample. As the sample and detector rotate, the intensity of the reflected X-rays is documented. When the geometry of the incident X-rays encroaching on the sample is able to satisfy the Bragg equation, constructive interference takes place and a peak in intensity arises. Figure 2.13 shows the peak position of the Zn_4Sb_3 powder measured with the XRD.

The XRD experiment is carried out with either powdered sample or single crystal. In single crystal XRD allows to observe the exact atomic positions with determining the bond length and angles. Whereas in the powder XRD, it provides information about the phase and crystallinity of material. The powder XRD looks at a large sample and mainly it is considered a bulk characterisation technique.

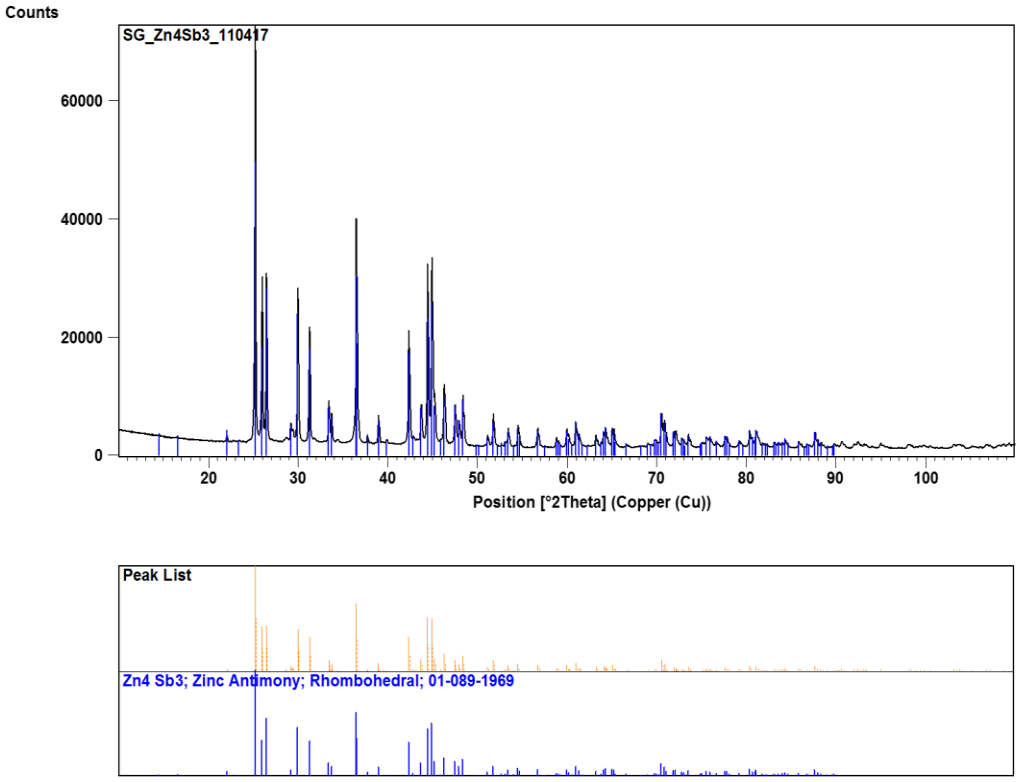

Figure 2. 13: Peak positions arise where the X-ray beam is diffracted by the crystal lattice in the XRD measurement of Zn_4Sb_3

2.4.2 Transmission electron microscopy

Transmission electron microscopy (TEM) is where a beam of electrons is diffused via an ultra-thin specimen. As it passes through, the electrons interact with the specimen. An image is then created by way of the interaction of the electrons conveyed via the specimen. Additionally, the image is enlarged and concentrated on an imaging device, for example a fluorescent screen on a layer of photographic film, or to be identified by a sensor, like a charge-coupled device (CCD) camera.

2.5 Sample preparation

A typical sample shape for electrical resistivity measurements is a rectangle whereas the sample could be in any shape to measure thermal conductivity. In this study the Zn_4Sb_3 thermoelectric material was received from the research collaborators in a cylindrical disk shape with a thickness of 5mm. The sample was cut using a wire cutting machine in

rectangular ($5mm \times 5mm$) shape. For contact purposes, four gold contacts were deposited on the four corners of each sample. Gold makes a better contact between the probes and the sample.

The silica aerogel was received in a random shape. Then, the samples were cut into a rectangular shape using a small fixed-blade cutter.

2.6 Synthesis of the sample using Aerogel

Most aerogels result from gels prepared by way of the sol-gel process. Sol-gel denotes a process where solid nanoparticles dispersed in a liquid phase (sol) collect together to shape a permanent three-dimensional network that extends throughout the liquid phase (gel).[105] The production of the aerogel involves a series of distinct steps, as follows:

Step 1: The establishment of different solvated metal precursors or stable alkoxide solutions (sol).

Step 2: Gelation resulting from the formation of an oxide- or alcohol- bridged network (gel) by means of the reactions of polycondensation or polyesterification, which produces a remarkable improvement in the viscosity of the solution.

Step 3: The gel aging (syneresis), during the polycondensation reactions last to a point that the gel changes into a solid mass, together with the contraction of the gel network and discharge of the solvent from the pores of the gel.

The gels aging process is vital as it prevents the gels that have been cast from cracking.

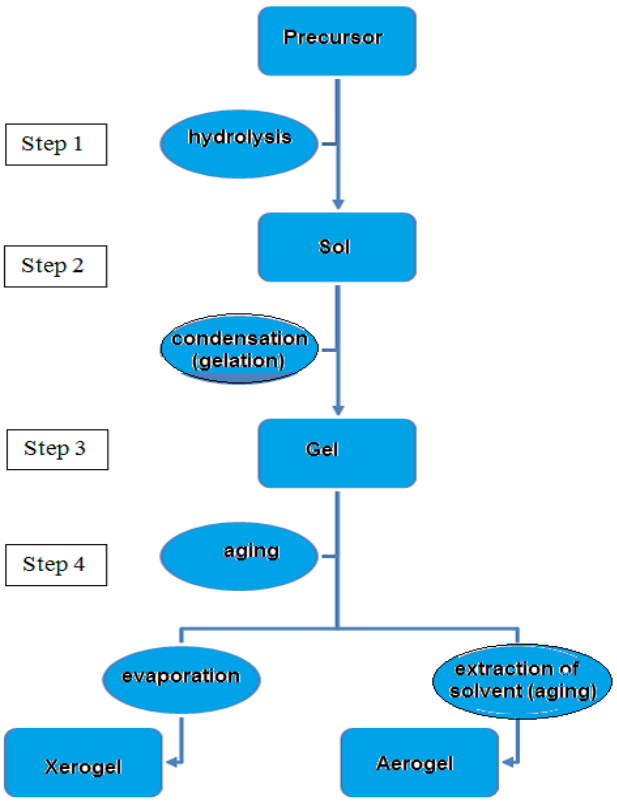

Figure 2. 14: Aerogel production steps[105]

Step 4: Aerogels are high surface area and nanoscale mesoporous materials of low density. After the gel is formed and shaped, it is dried. In this step, the solvent is eliminated. The way the liquid phase is withdrawn from the wet-gel establishes if the dried material is a denser Xerogel or a highly porous aerogel. Xerogel is produced by the evaporation of the solvent from the wet gel. This results in the breakdown of the wet-gel structure. Regarding the compliant network, the gel is distorted as a consequence of the capillary forces created by the liquid. Additionally, ambient pressure drying, or supercritical drying of the wet gels give rise to aerogels. Depending on which process is employed to remove the pore fluid from the wet gel, a dry solid with variable porosity is acquired.

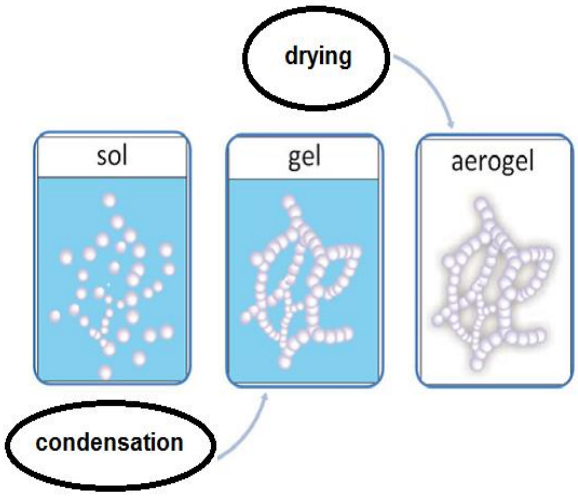

Figure 2. 15: Representation of the agglomeration of nanoparticles during the aerogel production process[105]

Weak capillary forces create an ambigel, whereas strong capillary forces produce a xerogel. Furthermore, zero capillary forces form an aerogel which ostensibly maintains the low-density framework of the wet gel.

Sol-gel is especially susceptible to the following parameters shown below:

• pH – pH relates to the hydrolysis phase, which is essential in creating the nanoparticles and gel network.

• Solvent – the solvent dissolves the nanoparticles and permits the nanoparticles to be linked together.

• Temperature – temperature has a crucial role to play in the creation of nanoparticles and it enables the nanoparticles to enter a gel network.

• Time – overall, if a gel is created slowly, it typically has a structure that is much more uniform, while the aerogel which is produced shows improved mechanical properties.

• Catalysts (both acids and bases) – quicken chemical reactions and have a considerable impact on the gelation period. In several instances, catalysts can lessen gel time.

• Agitation – combining a sol during the gelation procedure is essential to control the uniform improvement of the chemical reactions in the solution.

2.7 Sol-gel process

Alkoxide gelation is the most familiar method applied to produce silica gels. This method comprises the reaction of a silicon alkoxide with water in a solvent, for example acetone or ethanol, regularly in the presence of a basic catalyst. In this procedure, each specific component performs individually:

• Silicon alkoxide (typically tetramethoxysilane TMOS or tetraethoxysilane TEOS) acts as the source for the silica, whilst water performs as a reactant that allows the alkoxide molecules to combine

• A catalyst (like ammonium hydroxide or ammonium fluoride) enables the underlying chemical reactions to be quick enough to be beneficial

• A solvent (for instance ethanol, methanol, or acetone) which is miscible with both silicon alkoxides and water sets off the chemical reactions in one stage. When a silicon alkoxide reacts with water to form a silica gel, the following effects take place at the molecular level:

• Hydrolysis - Silicon alkoxide undergoes a reaction with water to produce silanol (Si-OH) groups where R is the alkyl group:

$$\equiv \mathrm{Si} - \mathrm{OR} + H_2O \rightleftarrows \equiv \mathrm{Si} - \mathrm{OH} + \mathrm{ROH}$$

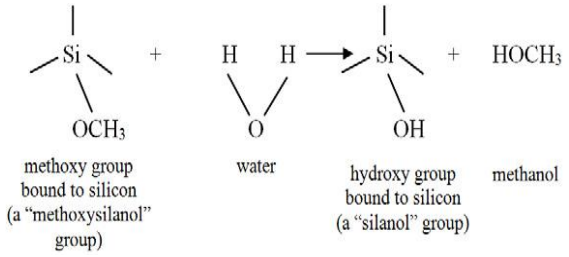

• Water condensation - Silanol groups react with one another:

$$\equiv \mathrm{Si} - \mathrm{OH} + \mathrm{HO} - \mathrm{Si} \equiv \rightleftarrows \equiv \mathrm{Si} - \mathrm{O} - \mathrm{Si} \equiv + \mathrm{H_2}O$$

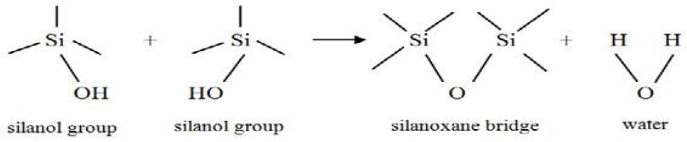

• Alcohol condensation

Silanol groups react with alkoxide groups (Si-OR) to create a siloxane bridge (Si-O-Si). This results in two molecules combining to form a larger molecule, where is R – alkyl group:

$$\equiv Si - OH + RO - Si \equiv \rightleftarrows \equiv Si - O - Si \equiv + ROH$$

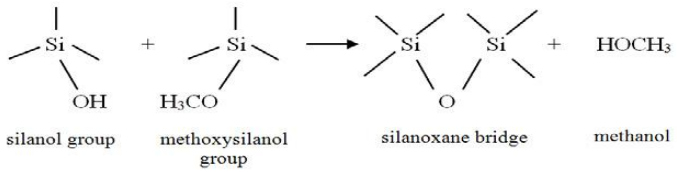

Individually, every silicon atom can create four siloxane bridges, where small molecules connect to the giant molecules that contain thousands of silicon-oxygen bridges. These large gatherings of oxygen and silicon bridges are termed silica nanoparticles and comprise diameters of a few nanometres. Consequently, the collection of nanoparticles forms a continuous network through the liquid solution, and hence, results in the formation of the gel.

2.8 Conclusion

This chapter explained the experimental technique that used to synthesised silica aerogel doped with Ni nanoparticles and silica aerogel doped with Zn_4Sb_3 nanoparticles and characterised the prepared materials to evaluate the ZT.

The sol-gel method has used to synthesise the silica aerogel doped with nanoparticles. The samples have been cut in a dimension that fit characterisation equipment such as SThM and CASK4200. The samples thermal conductivity has been measured using two different techniques, SThM and HotDisk analyser. The SThM allows the investigation of the thermal properties of the samples at submicron whereas the HotDisk has been used to confirm the SThM thermal conductivity measurements. XRD is used for the characterisation of crystalline materials, and the identification of fine-grained minerals such as clays, size of particles, the determination of unit cell proportions. The TEM is also used for the determination of nanoparticles size and shape. The measured particle size using the TEM has been compared with the measured size particle using XRD.

The Van Der Pauw structure on the CASK4200 equipment has used to measure the electrical resistivity. The measured sample's parameters have been used to evaluate the sample's thermoelectric figure of the merit.

Chapter 3

Thermal conductivity and seebeck coefficient measurement using SThM

3.1 Introduction

The characterisation of materials at the micro and nanoscale are proving a challenging task.[108] For instance, measuring thermal conductivity in thin films regularly requires the creation of a microscale test structure on the surface of the sample. Typically, this is often a complex process and has inadequate spatial resolution.[109] Scanning probe methods can offer micro and possibly nanoscale characterization at high spatial resolution and also require nominal preparation of the sample.[110] The implementation of AFM more recently has enabled the thermal properties of individual nanostructured materials, thin film, besides bulk materials with nanometer resolution to be mapped.[111]

SThM is an alternative to AFM that utilises a temperature sensitive probe. SThM is capable of imaging temperature distributions in the submicron regime with high spatial resolution using a sharp temperature-sensing tip as well as obtaining topographical images at the same time. SThM can operate in two different active and passive modes.[112] In passive mode, the resistive part of the thermal probe is employed as a resistance thermometer. Moreover, as the tip scans the surface, its temperature changes according to the temperature of the surface. A temperature change in the resistive element generates a change in relation to its resistance. By running a continuous current via the tip and measuring the resistance, the temperature of an extremely small area can be determined. In active mode, the resistive element of the thermal probe is operated as a resistive heater. Sufficient energy is utilised by the tip of the probe to preserve it at a set temperature by means of a feedback loop. The energy that is necessary to sustain the temperature signifies local thermal conductivity. Previous SThM probes such as the Wollaston wire are unable to deliver appropriate spatial and thermal resolution, given that they are restricted by the wire-based geometry.[113] The SThM tip serving as a resistance thermometer or heater is mounted on a microcantilever such that a constant tip-sample contact force is maintained by the force feedback loop and a thermal image is recorded simultaneously by imaging the surface topography.

The use of SThM for measuring sample temperature and local thermal conductivity is unable to determine the thermal conductance of heat flow within the probe (G_p) and at the probe-to-sample interface (G_c).[114-115] The SThM probe apex temperature (T_{apex}) is always estimated and considered as a constant value in order to extract values of G_p and then G_c. This increases the uncertainty of thermal conductivity measurement. The T_{apex} is estimated to be 3/2 times bigger than of the probe body temperature (T_{probe}).[115] However, the variation of T_{apex} and T_{probe} at higher than room temperature is not shown yet. Seeing as the probe apex is down to a scale compared to the average free path of the probe material, the thermal conductivity of the probe apex differs at different temperatures. G_p varies with temperatures more than the ambient temperature. However, the influence of this variation in relation to thermal conductivity measurement has not been identified.

In this chapter, the effect of the G_p on the thermal conductivity measurement is reported. The measured thermal conductivity has been validated using a HotDisk Analyser. The thermal conductivity using these techniques allows a comparison of the thermal conductivity measurement at the micro and submicron scale. The thermal conductivity measurement using the SThM enables the electronic and lattice thermal conductivity contributions to be individually examined. The procedure has been utilised to measure the thermal conductivity of silica aerogel doped with nickel nanoparticles (NiNP). In addition, the SThM technique permits the thermal conductivity of the NiNP to be measured separately, in contrast to the silica aerogel.

In this chapter a technique that measures seebeck coefficient within the bulk sample is also demonstrated. In this technique, a thermometer and a thermal probe that serves as a heater are utilised to measure the seebeck coefficient between the thermal probe and heated region of the sample. The thermal probe is used in conjunction with a Peltier heater and temperature controller to measure the local seebeck coefficient of the bulk sample. Additionally, the proposed method has been employed to determine the thermal conductivity of silicon.

3.2 Scanning thermal microscopy (SThM)

In scanning thermal microscopy**,** a thermal probe allows the thermal properties of samples to be determined. The SThM thermal probe along with an AFM configuration permits simultaneous topographical images of the sample top surface.[116-119] With resistive

probe, the temperature of a sample top surface (passive mode) and local thermal conductivity of sample top surface (active mode) could be determined.[120]

3.2.1 Resistive SThM probes type

In both the active and passive modes, the probe electrical resistance of the SThM and hence the temperature is controlled via an electrical circuit. Three types of resistive probe are typically applied in the operation of the SThM; specifically, the Wollaston wire probe, silicon nanoprobe and the Kelvin Nanotechnology (KNT) probe. In the Wollaston wire, the resistive element is a wire which is 5 µm in diameter and 200 µm in length.[121-122] It is made of Rh 10% Pt 90% and bent in a V-shape (Figure 3-1a). Figure 3-1b illustrates the schematic diagram of the Wollaston probe, whilst its properties are summarised in Table 3-1.[123]

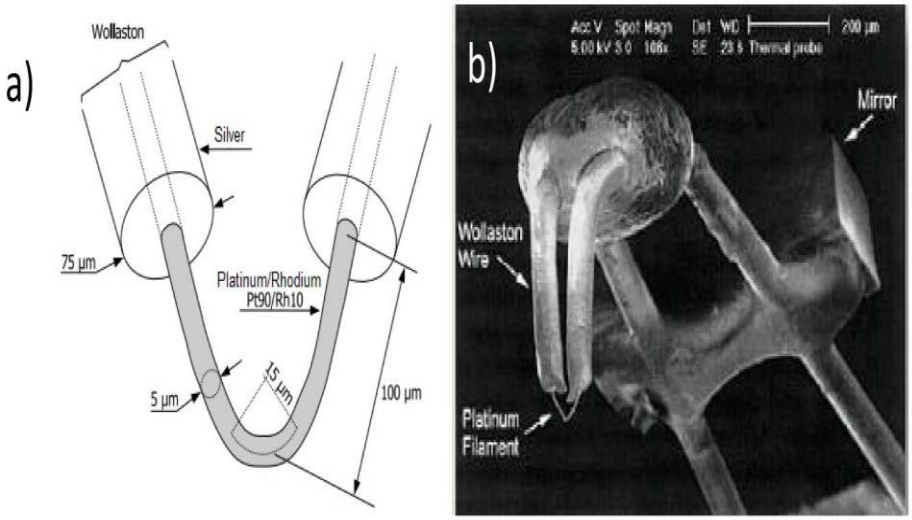

Figure 3. 1: a) Description of the Wollaston probe b) SEM (Scanning Electron Microscope) image of the Wollaston probe [123]

Tip	Resistive wire length (µm)	Resistive wire diameter (µm)	Radius of curvature of the apex (µm)	Spring constant (Nm^{-1})	Cut-off frequency (KHz)
Wollaston wire probe	200	5	15	5	240

Table 3. 1: Properties of the Wollaston wire probe [123]

The KNT probe contain Pd thin film as the resistor and pads are made of gold deposited on a cantilever (Figure 3-2). The cantilever was originally created from silicon dioxide (SiO_2) and subsequently changed to silicon nitride (Si_3N_4).[124] The cantilever's length, width and thickness are 150 µm, 60 µm and 0.4 µm respectively. The height and thickness of the tip are 10 μm and 40 nm respectively, whereas its width varies between 1.5 and 6 µm. The radius of the tip is smaller than 100 nm. SEM images of the KNT probe shown in Figure 3-3.

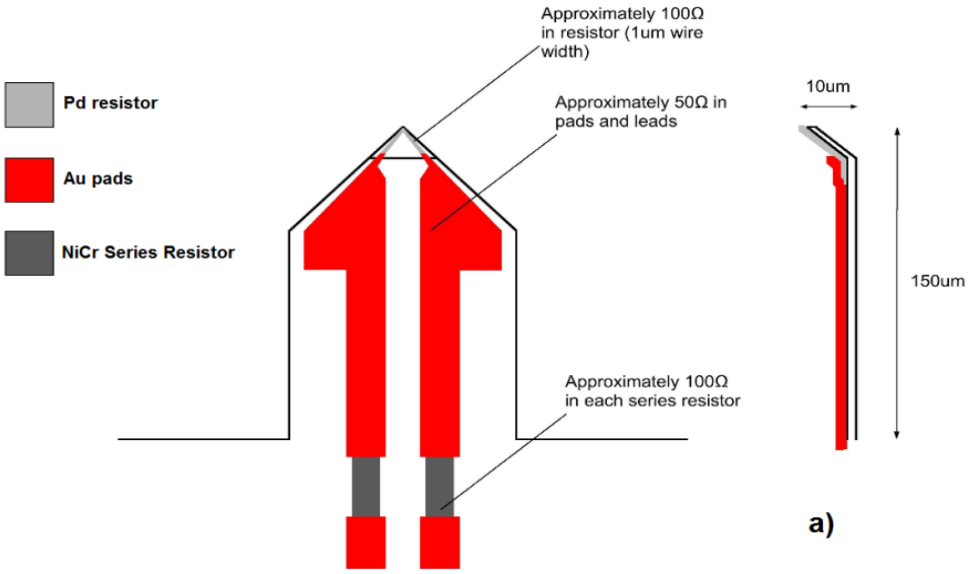

Figure 3. 2: Description of the KNT probe (courtesy of Kelvin Nanotechnology)[124]

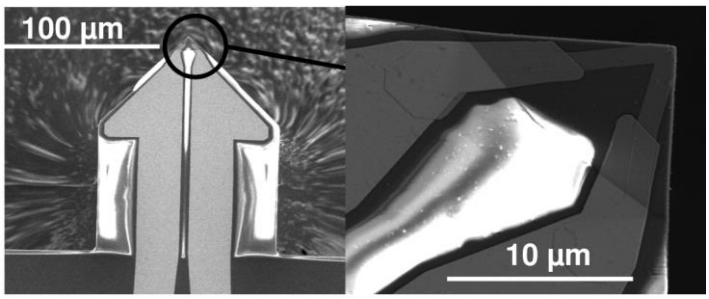

Figure 3. 3: SEM images of the Palladium probe [124]

The silicon nanoprobe incorporates two micrometric legs with a high-level doping and a low doped resistive element. The tip has a curvature nanometric radius with a shape that can be described as pyramidal (conical in the case of the IBM probe) and is installed on the top of the resistive element (Figure 3-4). Table 3.2 summarises the dimensions of the IBM silicon probes.[125]

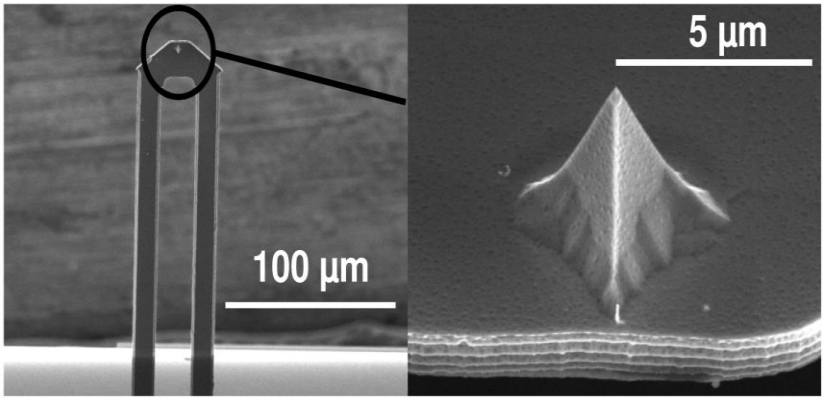

Figure 3. 4: SEM images of the Anasys Instruments probes (Anasys instruments) [125]

Tip	Leg length (µm)	Leg width (µm)	Leg thickness (µm)	Tip height (µm)	Tip radius (nm)	Spring constant ($N.m^{-1}$)	Resonant Frequency (KHz)
IBM [10]	50	10	0.5	2	< 20	1	200

Table 3. 2: Dimensions of silicon nanoprobes

In this work, the KNT thermal probe is made use of in order to demonstrate the sample's thermal properties.

3.2.2 SThM measurement approaches

In SThM probe resistivity measurements, the examination and understanding of the measurements involves a particular model that connects the electrical measurement to the sample's thermal properties (Figure 3-5). The heat balance equation on element dx of the Wollaston probe, as shown in Figure 3-6 is: [126]

$$\frac{\partial^2\theta}{\partial x^2} - \frac{hp}{\lambda S}\theta + \frac{\rho I^2}{\lambda S^2}(1 + \alpha\theta) = \frac{1}{\alpha}\frac{\partial\theta}{\partial t} \qquad \text{Equation 3- 1}$$

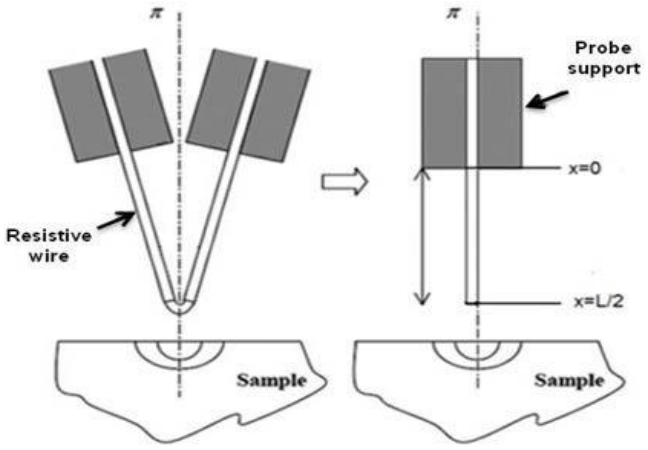

Figure 3. 5: Schematic of the Wollaston probe [126]

$\theta = T\text{-}Ta$ is the abscissa x relative temperature of the fin. In this case, λ, S, ρ, p and α are respectively the thermal conductivity, section, electrical resistivity, and perimeter of the Pt90/Rh10 wire. *h* represents the heat transfer coefficient of the losses in regard to the ambient environment. In view of the fact that the section of the Pt90/Rh10 wire is much smaller in comparison to that of the Wollaston wire, the boundaries are presumed to be heat sinks ($T=T_a$ at x=0). In addition, the probe's average temperature is regularly established electronically (Wheatstone bridge).[126] The thermal probe can be heated by means of a DC or AC current.

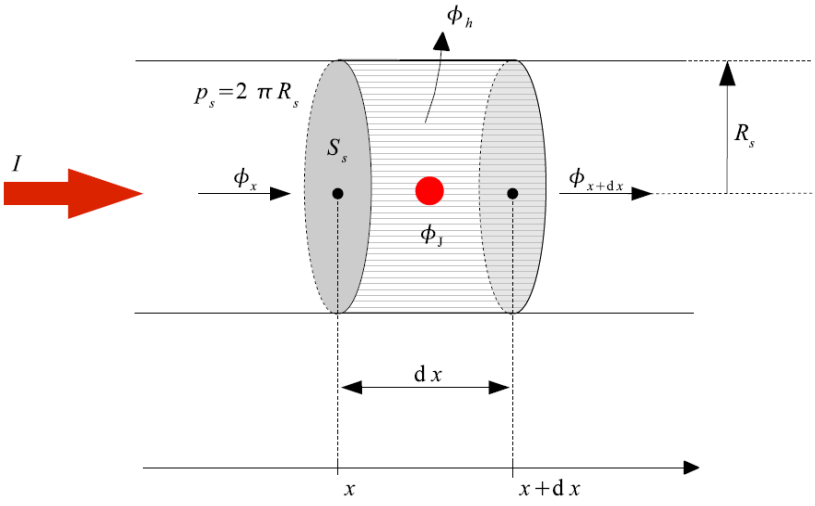

Figure 3. 6: The heat balance on an element $\boldsymbol{dx}$ of the Pt90/Rd10 wire[126]

A. DC regime

When a DC current is used to heat the probe, the time the probe takes to attain its equilibrium does not pass 3 ms.[126-127] As soon as this time is passed, Equation (3.1) is:

$$\frac{\partial^2\theta}{\partial x^2} - \frac{hp}{\lambda S}\theta + \frac{\rho I^2}{\lambda S^2}(1 + \alpha\theta) = 0 \qquad \text{Equation 3- 2}$$

When the probe is distant from the contact, the boundary condition at the tip apex is:

$$\frac{\partial\theta}{\partial x}\left(x = \frac{L}{2}\right) = 0 \qquad \text{Equation 3- 3}$$

When the probe is in contact with the sample,

$$\lambda S\frac{\partial\theta}{\partial x}\left(x = \frac{L}{2}\right) = G_{eq}\theta(x = \frac{L}{2}) \qquad \text{Equation 3- 4}$$

where G_{eq} (WK^{-1}) signifies the equivalent thermal conductance between the sample thermal conductance G_s and the probe-sample contact conductance G_c:

$$G_{eq} = \frac{G_s G_c}{G_s + G_c} \qquad \text{Equation 3- 5}$$

An explanation of the series of thermal conductance of the probe-sample is demonstrated in Figure 3-7. [127-129]

The heat methods that function between the sample and the probe are presented in G_c. According to the explanation of the sample (bulk, layered samples …) and the heat source; different expressions of G_s can be employed.

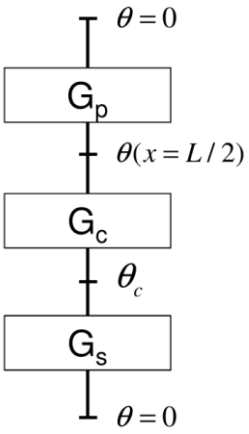

Figure 3. 7: Network of the thermal conductance's of the probe-sample system[129]

Let $m^2=hp/\lambda S$ and $\Omega=Geq/Gp$ where $Gp=\lambda S/L$ is the thermal conductance of the probe. Solving Equation (3.2) with the two conditions (Equations (3.3) and (3.4)), the Joule power of the probe when it is in contact is:[129-131]

$$P_c = \frac{\lambda SL^2 m^3 \bar{\theta}[2mLch\left(\frac{mL}{2}\right)+\Omega sh\left(\frac{mL}{2}\right)]}{mL\left[-4sh\left(\frac{mL}{2}\right)+2mLch\left(\frac{mL}{2}\right)\right]+\Omega[4\left(1-ch\left(\frac{mL}{2}\right)\right)+mLsh\left(\frac{mL}{2}\right)]} \qquad \text{Equation 3- 6}$$

and when the probe is not in contact

$$P_o = \frac{2\lambda SL^2 m^3 \bar{\theta} ch\left(\frac{mL}{2}\right)}{\left[2mLch\left(\frac{mL}{2}\right)\right]-4sh\left(\frac{mL}{2}\right)} \qquad \text{Equation 3- 7}$$

The expression $\Delta P/P_c = (P_c - P_o)/P_c$ was utilised in the calibration of the SThM probes for the measurements of the thermal conductivity of the bulk samples.[131] Here, the heat losses by way of convection (h=0) were not considered. Under this condition, Equation (3.2) produces:

$$\frac{\Delta P}{P_c} = \frac{P_c - P_o}{P_c} = \frac{3}{4}\frac{G_c G_s}{4(G_p G_s + G_p G_c) + G_c G_s} \qquad \text{Equation 3- 8}$$

B. AC regime

Puyoo (2012), made use of an old palladium probe (with SiO_2 cantilever) in the AC regime to ascertain the thermal conductivity of silicon nanowires embedded in silicon dioxide sample.[132] In his measurement approach, Puvoo modified Lefèvre's model to the palladium probe by explaining the probe as two thermal fins created from two adjacent materials (Pd and SiO_2).[133] The term diffusion was just taken for the SiO_2 part, given that this part has a bigger part in contrast to that of the Pd ($S_{SiO2}/S_{Pd} \sim 25$). Moreover, the same boundary conditions as seen in Equations (3.3) and (3.4) were appropriated and the measurements completed. Seeing as the dimensions at the tip apex are down to distances compared to the average free path of the material, the thermal conductivity of the probe apex can vary contrary to the one assessed in the diffusive regime. Essentially, regarding the silicon nitride (Si_3N_4) cantilever, the average free path of the phonon at room temperature is of the order of 20 nm and the tip radius is roughly 50 nm.[133]

Tovee *et al. (2012)* recommended that heat transfer in the probe based on the diffusive regime is a rational calculation. They suggested that their method is related to the fact that the Knudsen number is insignificant with regard to SiO_2 (old cantilever) - $Kn \simeq 0.2$. Nevertheless, the thermal resistance of the probe (Rp) measured experimentally in the vacuum environment ($Rp = 8 \times 10^4$ K W^{-1}) is greater than anticipated in relation to numerical simulations ($Rp = 5.35 \times 10^4$ K W^{-1}). This could be because the probe section decreases at the probe apex and hence, for the additional thermal resistance brought about by the boundary scattering within the probe apex to be considered.[133] Additionally, in the numerical simulations, these effects were disregarded, as deliberated by the authors.[134] In effect, the radius of the tip-sample mechanical contact may possibly be smaller than the average free path of the heat carriers in the sample.

3.2.3 Heat transfer mechanism

The working of a heated AFM cantilever is dependent on the temperature dispersal within the cantilever and the cantilever tip. Figure 3-8a displays the heat flow paths from and within a heated cantilever. The heat generated in the tip flows to the substrate either through the environment or through the cantilever and then to the substrate. Heat flows through the cantilever heater and legs by conduction and from the cantilever to the environment by conduction and thermal radiation.[134] The thermal conductance of the silicon-heated cantilever

is roughly 1 μWK^{-1} when it is operated to heat a substrate as shown in Figure 3-8b. Approximately 30% of the total heat created emanates from the heater, across the air gap and into the substrate.[135] The rest of the heat flows down the legs, although virtually all of this heat cascades into the substrate in the end. Generally, convection and radiation are negligibly small.

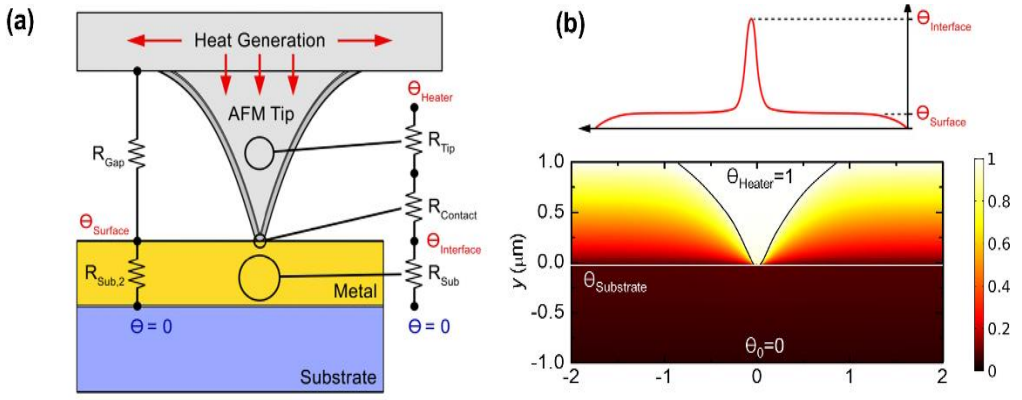

Figure 3. 8: (a) Thermal resistance network model and expected temperature profile on the substrate. (b) Non-dimensional temperature profile on the surface of a silicon substrate treated with a 100 **nm**–thick gold film.[135]

Many applications of heated AFM cantilevers depend on locally raising the temperature at the tip-substrate interface. Heat transfer via the tip is either by means of the direct solid contact or through a water meniscus formed near the contact. When the tip is in contact with the substrate closer than the average free path of the medium molecule, ballistic conduction through the gap determines the tip-sample heat transfer (Figure 3-9).[133-135] Thermal conduction via the tip-sample contact is crucial for heated cantilever applications, due to the small size of the contact and also due to thermal boundary resistance at the tip substrate interface. Typical thermal contact thermal conductance is in the range $0.1-100\ nWK^{-1}$. For a tip radius of 30 nm, a typical contact diameter is approximately 10 *nm* with a contact force of 10 nN. In humid air, a water meniscus forms at the tip-sample contact. For a wetting surface and relative humidity of 0.5%, the liquid contact diameter is about 30 nm, somewhat larger than a typical solid contact diameter of about 10 nm.[135] Typically, the contact thermal conductance dominates the total thermal conductance through tip-sample contact.

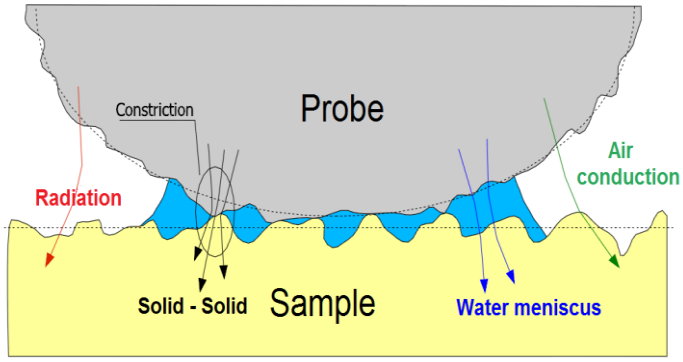

Figure 3. 9: Schematic of the different heating method that operates between the sample and the probe [135]

When the cantilever is in air, heat transfer to the air is dominated by conduction rather than convection. However, when a heated cantilever is operated in water, the heat transfers by convection.[136]

3.3 Experimental model of thermal conductivity measurement

The experimental model of thermal conductivity measurement using SThM is based on Joule heat dissipation in the probe-sample system. As soon as the probe makes contact with the surface of a sample, the induced electrical power in the probe is relative to the heat flux regarding the sample and, consequently, to the sample's thermal conductivity. The probe and probe-sample thermal interface conductance was determined with the aim of measuring the sample's thermal conductivity. Measurement of the SThM included establishing the probe's Joule power relative difference $\Delta P/P_c = (P_c - P_a)/P_c$, where P_c and P_a signify the probe's Joule power when the probe has in and out of contact with the surface of the sample.[116-117]

In this work, a SThM nanothermal probe that comprises a thin resistive Pd film and pads of gold deposited on a silicon nitride (Si_3N_4) cantilever is employed in the contact mode of the AFM in both the active and passive methods of SThM. The tip radius is ≤ 100 nm with a spring constant $\sim 0.45\ \mathrm{Nm}^{-1}$. A calibration method for the SThM probe based on international temperature standards was employed. In this method, the benzophenone melting point ($55\ ℃$) is used as a calibration reference for SThM equipment and the calibration of the equipment was undertaken prior to each set of measurements.[118] The AFM XE150 from Park Systems was mounted with the SThM module used to evaluate the thermal conductivity.

A HotDisk thermal conductivity (HDTh) analyser TPS 2500 S was used to compare measured thermal conductivity with the values extracted from the SThM.

A thermal conductance network model shown in Figure 3-7 was used to understand the heat flow from probe to sample and to extract the sample equivalent thermal conductance. The quantitative relationship between the relative joule heat power and thermal conductance is described in Equation 3-8 and has been used to extract the probe to sample thermal conductance's:[117]

$$\frac{\Delta P}{P_c} = \frac{V_c^2 - V_o^2}{V_c^2} = \frac{3G_cG_s}{16(G_pG_s + G_pG_c) + 4G_cG_s} \qquad \text{Equation 3. 9}$$

where V_c^2 and V_o^2 are the calculated voltage in and out of contact and G_p, G_s, and G_c signify the thermal conductance of the probe, sample and the contact of the probe-sample. Extracting the sample's thermal conductivity is dependent on determining these parameters carefully.

3.3.1 The SThM thermal and current calibration

The SThM in active mode was placed in contact with an ultra-fine thermocouple. The ultra-fine thermocouple is Cu-Con, type T (class 1) with an effective temperature measurement range of $-40\ to + 300$ ℃ with an accuracy of ± 0.5 ℃ and probe diameter of the < 25 μm. The temperature of the thermal probe was increased to different temperatures by applying I_{probe}. The SThM thermal probe scans the thermocouple surface at a low rate scan (0.5 Hz) which lasts for 30 minutes. The generated heat flows to the thermocouple through the SThM probe apex and allows measurements of the T_{apex}. The SThM module from park systems provides a probe temperature profile image from which T_{probe} can be extracted.

It is a simulation based on the variation of the probe's current as the probe examines the surface of the sample. Figure 3-10 shows the measured temperature by the thermocouple (T_{apex}) at different applied I_{probe} of the SThM along with the extracted T_{probe}. There is a difference in the measured T_{apex} and T_{probe} for the applied I_{probe} to the SThM thermal probe. The generated heat conduct through the probe apex to the thermocouple and it is appropriate to consider that the temperature measurement in thermocouple is the T_{apex}.

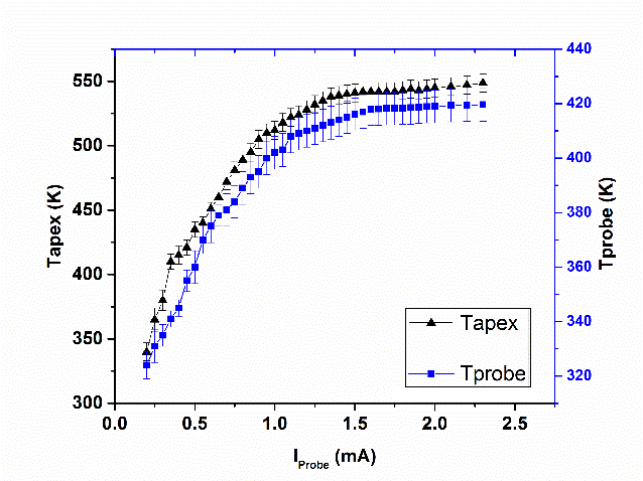

Figure 3. 10: $\boldsymbol{T_{probe}}$ and $\boldsymbol{T_{apex}}$ measurement of the SThM thermal probe at different driven current

Figure 3-11 shows the probe temperature profile, probe current and the surface topography of the thermocouple.

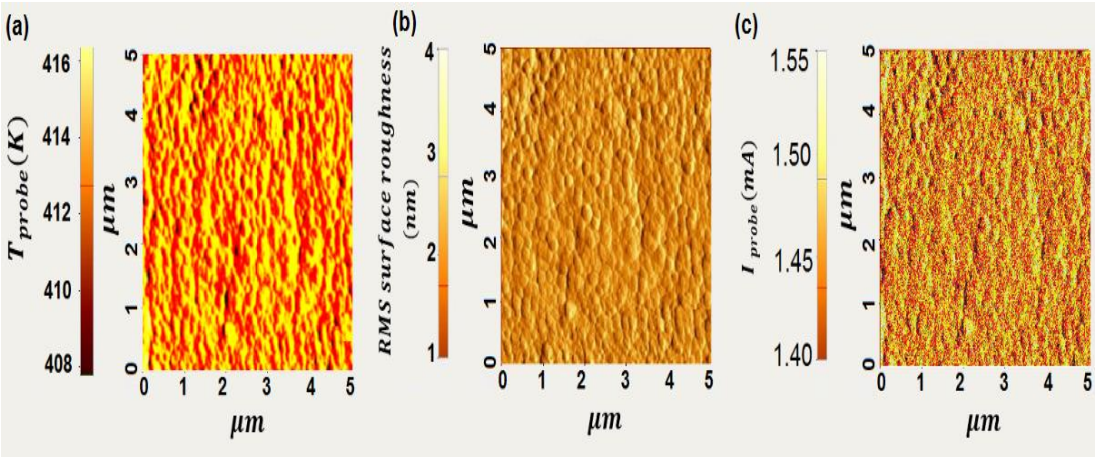

Figure 3. 11: SThM (a) $\boldsymbol{T_{probe}}$, (b) topographical measurement and (c) $\boldsymbol{I_{probe}}$of the heating stage

To validate the measured T_{apex}, the SThM in passive mode has been used in conjunction with a Peltier heater temperature controller. The SThM thermal probe was placed in contact with a Peltier heater at different temperatures and I_{probe} of the thermal probe has been measured. In Figure 3-12, the I_{probe} increases linearly with temperature. However, at temperatures higher than 500 K of the heating stage, for a small change in the heating stage temperature, the probe current will change considerably. The scanning of the heater phase at

different temperatures was completed at low scan rate (0.5 Hz) to permit the tip to achieve thermal equilibrium with the heater surface. The measured I_{probe} for a given heating temperature are in accordance with the correspondent T_{apex} at the applied I_{probe} in active mode of the SThM thermal probe.

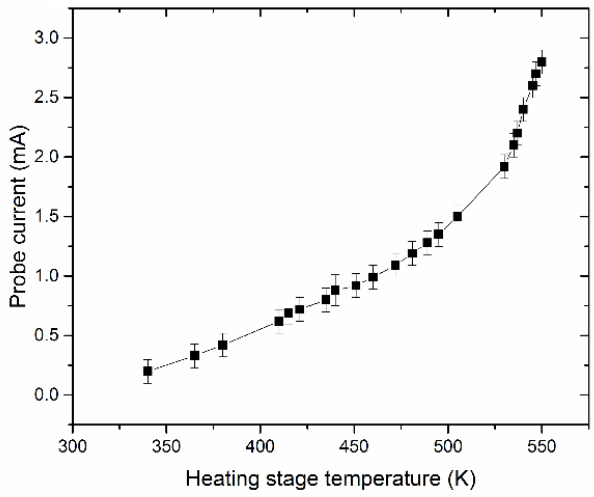

Figure 3. 12: SThM $\boldsymbol{I_{probe}}$measurements of the Peltier heating stage in active mode

3.3.2 Determining the mean probe temperature ($\boldsymbol{T_{probe}}$) and probe apex temperature ($\boldsymbol{T_{apex}}$)

G_p is defined as the ratio of dissipated electrical power in the probe (P_p) and its temperature rise and is given by the relationship:

$$G_p = \frac{P_p}{|\Delta T|} = \frac{I^2 R}{|T_{apex} - T_a|} \qquad \text{Equation 3. 10}$$

In this equation P_p and T_a are the Joule heating generated by the movement of the electric current (I_{probe}) by way of the probe and the ambient temperature respectively. R is electrical resistance of the probe that is measured using a Keysight 34420A Micro-Ohm meter and verified using the manufacturer's specified value.

To measure G_p, the SThM probe was placed in contact with a very low thermal conductivity material. Silica aerogel was used because it has sufficiently low thermal

conductivity, whereby the heat transfer from the thermal probe to the sample is exceedingly low. The SThM thermal probe was positioned in contact with the surface of the silica aerogel in passive mode and the T_{probe} was measured for an applied I_{probe}. The relationship is shown in Figure 3-13. T_{probe} increases linearly with I_{probe} up to 0.6 mA. However, by $I_{probe} =$ 1.8 mA the T_{probe} is in a steady state and no further change in T_{probe}. Figure 3-14 shows the SThM T_{probe} of the silica aerogel doped with NiNPs at concentration of 700 ppm. The bright dots are NiNPs clusters. The measured joule power (P_p) and temperature difference (ΔT) used to extract the G_p using equation 2.

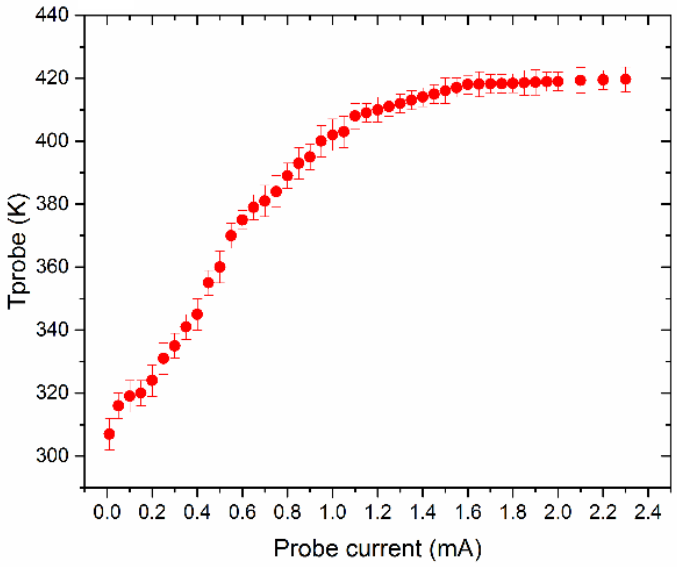

Figure 3. 13: Variation of the SThM thermal temperature $\boldsymbol{T_{probe}}$ of the silica aerogel sample

3.3.3 Determining the SThM probe thermal contact conductance (G_c)

The SThM probe thermal contact conductance (G_c) is obtained by measuring the probe's temperature when it makes contact with a high thermal conductivity material (λ_s) at a known temperature using the relationship:[117]

$$\lim_{\lambda_s \geq \infty} \left(\frac{I_c^2 - I_o^2}{I_c^2}\right) = \frac{3}{4}\frac{G_c}{G_c + G_p} \qquad \text{Equation 3. 11}$$

where I_c^2 and I_o^2 are the measured probe electrical current in and out of contact. The temperature of the sample is controlled and fixed at a temperature close to ambient temperature, while the heated SThM probe is placed in contact with its top surface. The measured G_p from the previous stage (section 3.3.2) based on T_{apex} is used to extract G_c. Specific precautions must be considered, as contact conductance depends on parameters like surface roughness.[119] Simultaneous scanning was carried out on samples of bulk silver and bulk copper. The I_{probe} is determined before and after contact and the term $I_c^2 - I_o^2/I_c^2$ extracted.

The measured values of G_c are compared with the predicted value of G_c according to classical theory using the relationship:

$$\frac{1}{G_c} = \frac{1}{\pi a}\frac{2k_s + k_{tip}\,tan\theta}{k_s k_{tip}\,tan\theta} \qquad \text{Equation 3. 12}$$

where a is the diameter of the point of contact with a diameter of 100 nm for a contact force of $0.45\ nN$, and it is estimated to be 100 nm due to coating with 5 nm$/140$ nm NiCr/Au on top of the SThM probe tip. The k_{tip} (11.3 $\mathrm{Wm^{-1}K^{-1}}$ for NiCr) and k_s (29 $\mathrm{Wm^{-1}K^{-1}}$) for silicon nitride as well as the thermal conductivities of the tip and the cantilever base respectively and θ (34°) is the half-angle of the conical tip, according to the manufacturer's specifications.

Heat transfer between the sample and the probe not only occurs via solid-to-solid contact but also through thermal radiation and water meniscus.[113]

$$G_c = G_{solid-solid} + G_{liquid-solid} + G_{air-solid} \qquad \text{Equation 3. 13}$$

Thermal radiation (air-solid) in SThM measurements is derived from the difference between T_{probe} and T_{tip}. Thermal conductance owing to a water meniscus at the-tip-sample contact has been reported,[120] although at high temperatures the water starts to evaporate, and the liquid-to-solid thermal conductance can be neglected.

3.3.4 Determining the sample thermal conductance (G_s)

The parameters identified in the previous steps (section 3.3.2 and 3.3.3) are used to identify the sample thermal conductance G_s. The heat flow via contact of diameter a on a

planar bulk sample with thermal conductivity of λ_{sample} can be approximated by an semi-spherical geometry, associated with thermal conductance as follows:[120]

$$G_S = 2.776\,\lambda_{sample}\,a \qquad \text{Equation 3. 14}$$

3.4 Extracting T_{apex} and T_{probe} from the thermal probe

The SThM in active mode in contact with an ultra-fine thermocouple is used to measure the T_{apex}. The generated heat in the SThM caused by I_{Probe} conduct to the thermocouple through the probe apex. The SThM probe was scanned using very slow scan rate (0.5 Hz) for 30 minutes to allow the thermocouple and probe apex to be thermal equilibrium. T_{probe} was extracted from the probe temperature profile provided by the SThM module. Figure 3-10 shows T_{probe} and T_{apex} when the SThM is in contact with a thermocouple with an applied I_{Probe}. At lower $I_{Probe,}$ the T_{apex} and T_{probe} are almost at the same temperature and then the temperature difference is increased as I_{Probe} increased. For $I_{Probe} = 0.1$ mA the difference between T_{apex} and T_{probe} is 1.025, whereas at $I_{Probe} = 2.3$ mA the difference between the T_{apex} and T_{probe} is 1.30. Figure 3-11 presents the variation in the I_{Probe}, thermocouple topographical image and probe temperature. For $I_{Probe} = 1.44$ mA, $T_{probe} = 413$ K has been extracted from the probe temperature profile in Figure 3-11. The thermocouple surface roughness confirms beneficial contact between the SThM thermal probe and the top surface of the thermocouple as the RMS surface roughness of the thermocouple is less than 3nm.

The T_{apex} results were validated with the SThM probe in passive mode in conjunction with the Peltier heater stage. The Peltier heating stage set in different temperature and the I_{Probe} of the SThM thermal probe has measured. Figure 3-12 shows the measured I_{Probe} of the SThM probe and heating stage temperatures. The SThM probe current has increased linearly as temperature increases. However, at a temperature above 520K, the probe current is more sensitive to temperature increase. The measured I_{Probe} for the given temperature is in good agreement with the measured temperature and probe current of the SThM in active mode in contact with an ultra-fine thermocouple.

The SThM in active mode placed in contact with a silica aerogel sample doped with nickel nanoparticles at a concentration of 700 ppm. The silica aerogel sample with extreme

low thermal conductivity was used with the intention of minimising the heat transfer between the SThM probe and sample. Thermal conductivity of $0.020\ \mathrm{Wm^{-1}K^{-1}}$ was noted for silica aerogel. Figure 3-13 shows the T_{probe} for the given I_{Probe}. The T_{probe} has increased linearly with I_{Probe} , however at higher I_{Probe} there is a small variation in T_{probe} as the I_{Probe} increases.

Figure 3-14 shows the variation of the T_{probe} of the silica sample at $I_{Probe} = 1.2$ mA. The yellow colour is the nickel nanoparticle clusters, whereas the red colour is silica aerogel. G_p has been extracted using Equation 3-10 for the given I_{Probe} and measured T_{probe}. The corresponding T_{apex} for the measured T_{probe} has been extracted from Figure 3-10.

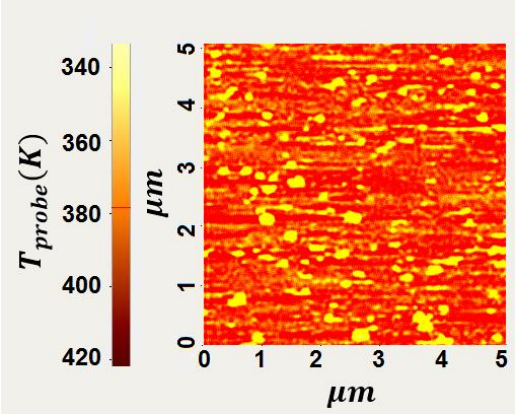

Figure 3. 14: SThM image of the silica aerogel doped with NiNPs

Silica aerogel has extreme low thermal conductivity and it has used to measure I_{probe} and extract T_{probe}. This allows to determine the T_{probe} at different temperatures rather than only at room temperature. The measured T_{probe} has compared with T_{apex} measured with the thermal probe when it is in contact with an ultra-fine thermocouple.

3.5 Extracting the G_p and G_c thermal conductance

G_p is extracted based on Equation 2 for T_{apex} and is plotted in figure 3-15. At lower I_{probe}, G_p is almost the same for both T_{probe} and T_{apex}. However, at higher I_{probe} there is almost an order of magnitude difference observed in values of G_p. The values of $6.18 \times 10^{-4}\ \mathrm{WK^{-1}}$ and $1.27 \times 10^{-3}\ \mathrm{WK^{-1}}$ has been extracted for G_p for both T_{apex} and T_{probe} respectively at an applied $I_{probe} = 2.1$ mA. This deviation in measurements

originates from the difference in T_{apex} compared with T_{probe}. Any variation in G_p must be considered to measure the heat flow mechanisms between the probe and the sample. The heat generated in the SThM probe flows to the substrate either by solid-to-solid contact (probe apex) or through the probe legs by air conduction and thermal radiation. The temperature difference between T_{probe} and T_{apex} in the SThM thermal probe could be used to determine the amount of heat generated and flow to the substrate by air conduction and thermal radiation. Figure 3-10 shows that approximately 40% of the total heat generated in the probe flows to the substrate through air conduction and thermal radiation mechanisms. Roughly 60% of the heat generated flows to the substrate through probe-to-sample contact. This expect to be due to changes in the probe's apex thermal conductivity with increasing temperature.

Given that the majority of the heat generated in the probe emanates from the tip to the sample, it is appropriate to consider that T_{apex} is the temperature of the probe contact point with the sample. Considering the extracted G_p, the G_c is measured by way of Equation 3-11 and outlined in Figure 3-15.

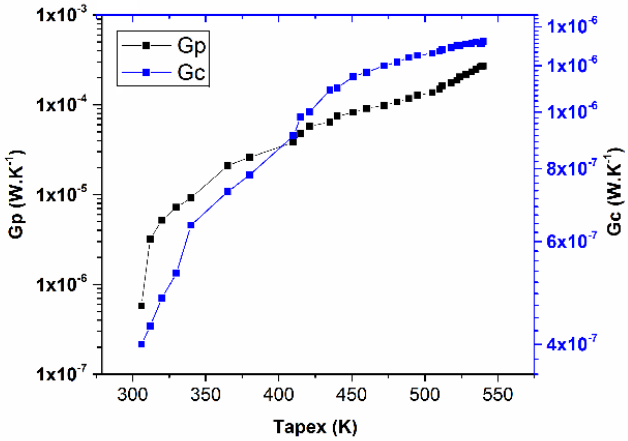

Figure 3. 15: Variation of the probe conductance ($\boldsymbol{G_p}$) and ($\boldsymbol{G_c}$) as a function of the probe temperature ($\boldsymbol{T_{apex}}$)

The value G_c exhibits a smaller change compared with G_p. The G_c values of $1.17 \times 10^{-6}\mathrm{WK}^{-1}$ and $1.19 \times 10^{-6}\mathrm{WK}^{-1}$ has measured at $T_{apex} = 460$ K for Ag and Cu respectively.

A value for liquid-to-solid conductance of around $\approx 2 \times 10^{-7}\mathrm{WK}^{-1}$ has been reported in the case of a nanothermal probe.[13] The water meniscus has almost vanished at

temperature above 373 K and therefore it can be assumed that thermal conduction through the liquid to solid is negligible. However, at lower temperature the thermal conduction through the liquid to solid has to be taken to the account. The estimated value of the G_c according to classical theory is in the range of $10^{-7}\mathrm{WK}^{-1}$, which is in good accordance with the measured value. The measured G_c value is noted to be consistent owing to the coherence of the high thermal conductivity data.

3.6 Extracting the G_s thermal conductance

The identified parameters are applied in order to examine the thermal conductivity of the silica aerogel doped with nickel nanoparticles at 700ppm. The SThM thermal probe enables the metal contents to distinguish from the silica aerogel since they have different thermal conductivity. Both topographical and thermal images for the top surface of the sample were simultaneously gathered. The SThM measurements were attained by way of the same experimental atmospheric conditions at room temperature, excepting the number of pixels creating the images used to improve image resolution. Thermal images measuring at $5\ \mu\mathrm{m} \times 5\ \mu\mathrm{m}$ are presented in Figure 3-14 for silica aerogel. In order to reduce uncertainty in the measurements; they were undertaken on six different locations on the sample. Every single scan lasted approximately 30 min and is composed of 256×256 pixels, while the changing scanning rate improved the uncertainty concerning the SThM measurements.

The SThM voltages V_c^2 and V_o^2 were measured when the thermal probe was in contact with the top surface of the silica aerogel and in the air. The identified $G_p$and G_c was substituted in Equation 3-9 and G_s was extracted. The thermal conductivity (λ_{sample}) was extracted using G_c in Equation 3-14. Temperature dependent thermal conductivity measurements using SThM is presented in Figure 3-11 when the T_{apex} and T_{probe} measurements were used to extract the G_p. Median values of thermal conductivity is $30 \times 10^{-3}\ \mathrm{Wm}^{-1}\mathrm{K}^{-1}$ at room temperature for T_{apex} and T_{probe}. The median values of the thermal conductivity are $43 \times 10^{-3}\ \mathrm{Wm}^{-1}\mathrm{K}^{-1}$ and $45 \times 10^{-3}\ \mathrm{Wm}^{-1}\mathrm{K}^{-1}$ at 410 K for T_{apex} and T_{probe} respectively. There is almost 5% difference in thermal conductivity measurements when the T_{apex} and T_{probe} are considered. This is due to the temperature difference in the SThM thermal probe compared with the probe apex.

The measured thermal conductivity was then compared with measurements using a HotDisk analyser. There is a good agreement in the thermal conductivity measurement using

the HotDisk analyser and SThM. The median value of thermal conductivity is 30×10^{-3} $\mathrm{Wm^{-1}K^{-1}}$ at 300 K for silica aerogel doped with NiNPs at a concentration of 700ppm using the HotDisk analyser.

3.6.1 Submicron Thermal analysis using SThM

Measuring thermal conductivity using the SThM allows the investigation of thermal conductivity in the sub-micron scales. The SThM enables independent contributions to thermal conductivity to be investigated, seeing as the dimensions of the probe are comparable to the average free path of the material examined. Therefore, the measured thermal conductivity utilising SThM can be presumed to be intrinsic thermal conductivity. Additionally, the total thermal conductivity is a combination of the electronic and lattice components. The thermal conductivity of the copper material in the heating phase was applied to examine the essential and electronic thermal conductivity measurement via the SThM. A thermal conductivity of $\sim 25 - 32$ $\mathrm{Wm^{-1}K^{-1}}$ at room temperature has been found for copper using SThM measurement. The four-point probe station in Keithley 4200A-SCS Parameter Analyser has been used to measure the electrical resistivity of the copper. The value of $1.68 \times 10^{-8} \Omega\mathrm{m}$ was measured and used to calculate the electronic thermal conductivity. The value of 435 $\mathrm{Wm^{-1}K^{-1}}$ was extracted for the electronic part of the thermal conductivity of copper material. The calculated electronic thermal conductivity in conjunction with the thermal conductivity measurement using SThM is $\sim 460 - 467$ $\mathrm{Wm^{-1}K^{-1}}$, which is in good agreement with the value of the thermal conductivity ~ 471 $\mathrm{Wm^{-1}K^{-1}}$ provided by the manufacturer.

3.6.2 Thermal conductivity of the NiNP clusters

SThM enables the thermal conductivity of NiNP clusters and silica aerogel to be measured separately. The silica aerogel and nickel nanoparticle clusters are distinct in the SThM thermal image in the Figure 3-14 as the thermal conductivity of the nickel and silica aerogel is different. At room temperature (T = 300 K), the thermal conductivity of bulk nickel is 90.0 $\mathrm{Wm^{-1}K^{-1}}$.[123] A mean thermal conductivity of 16.0 $\mathrm{Wm^{-1}K^{-1}}$ is extracted for the NiNP cluster using SThM. The measured thermal conductivity agrees fully with the calculated thermal conductivity using nonequilibrium molecular dynamics (NEMD).[123] The results show that the thermal conductivity has reduced with the compact size of the nickel to nanoscale dimensions due to a reduction of the phonon mean free path.

3.6.3 Silicon thermal conductivity measurement

SThM was applied to bulk silicon material to determine the thermal conductivity and the results compared with the thermal measurements using the Raman temperature spectroscopy technique. Silicon material thermal properties are known and is well characterised. Figure 3-16 shows the thermal image and topography image of the silicon material surface using SThM.

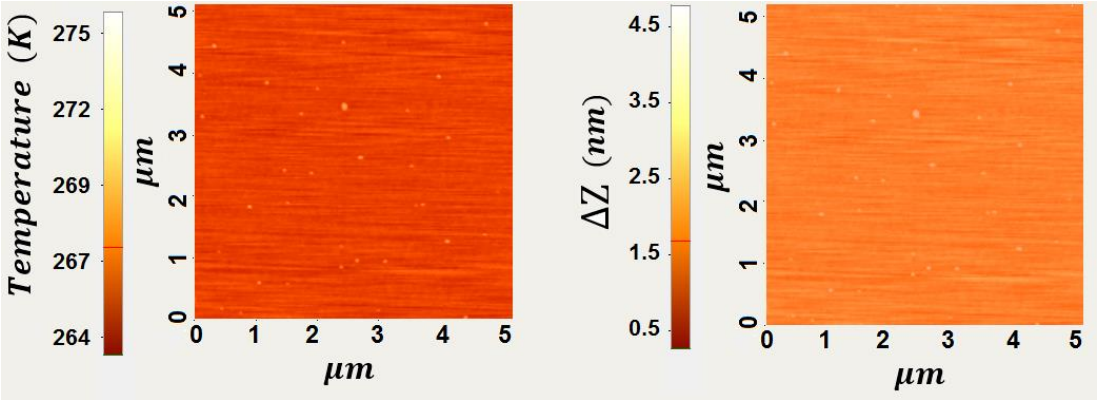

Figure 3. 16: Thermal (left) and topography (right) image of the silicon sample

The silicon wafer was cut and measured by Raman spectroscopy. Dimensions of the silicon sample is 1 cm × 1cm in length and width respectively. The thickness was 525 μm. The silicon sample was mounted on a heating stage to evaluate the thermal properties at various temperatures.

The Raman peak positions of the silicon sample and also the peaks at different temperatures are shown in Figure 3-17. The correlation between the Raman peak position and the temperature of the silicon sample can then be regulated, as Figure 3-18 illustrates.

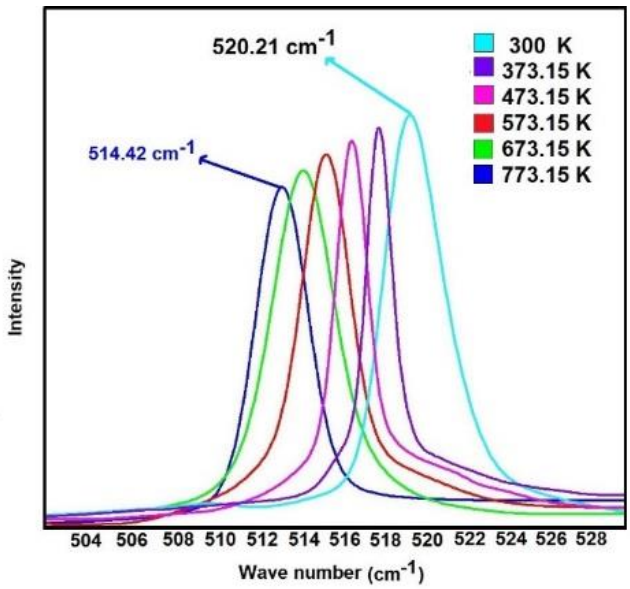

Figure 3. 17: Raman spectra and peak position of the silicon sample at various temperatures

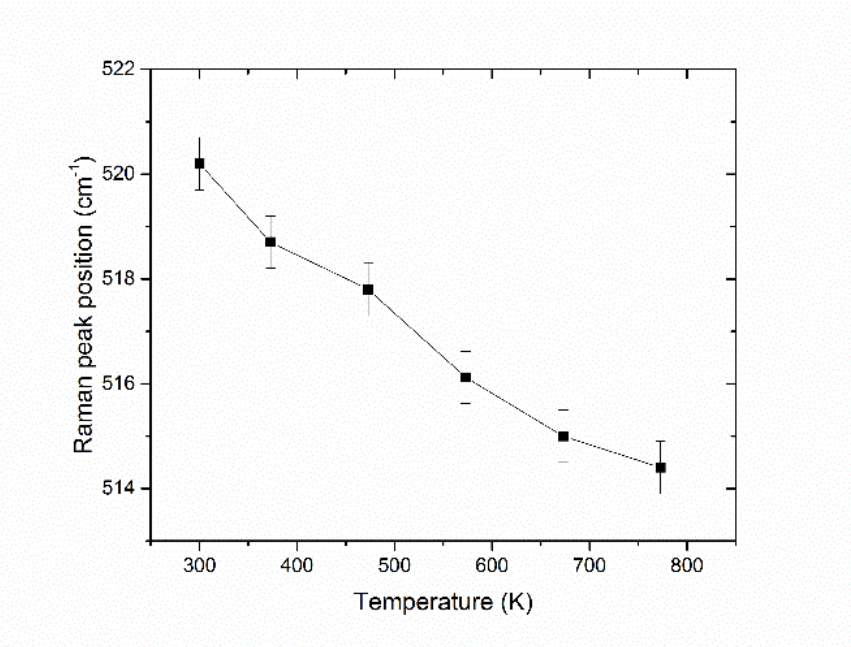

Figure 3. 18: Raman peak position vs the temperature of the silicon sample at a low laser power P=1.8mW

Figure 3-18 specifies a near linear correlation between the Raman peak positions and the temperature of the silicon sample. Moreover, as the temperature rises, the Raman peak position declines.

The thermal conductivity measurements using SThM and Raman spectroscopy are shown in Figure 3-19. There is agreement in thermal conductivity by the two measurement

techniques. However, the thermal conductivity measurement using Raman spectroscopy is slightly higher than that measured by SThM technique. This could be attributed to additional heat induced by the laser power during the thermal conductivity measurement.

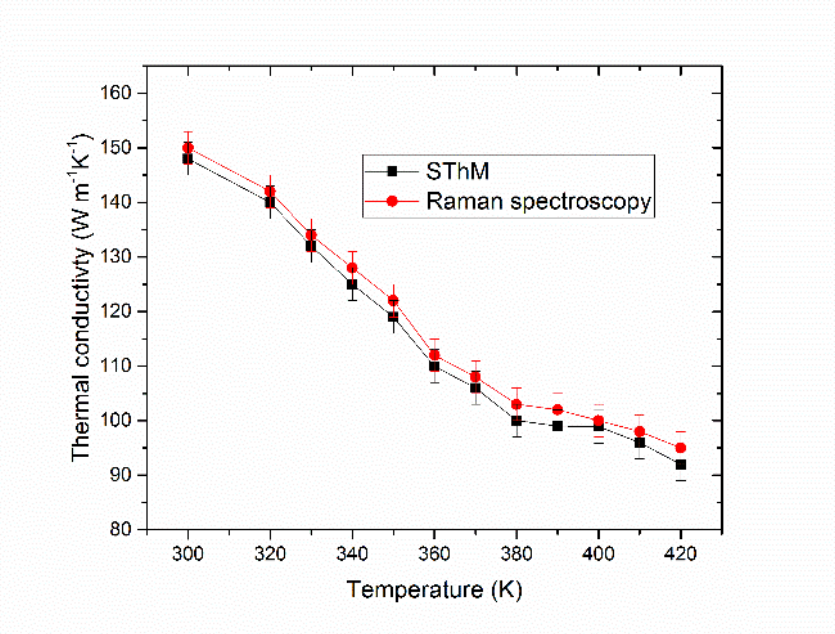

Figure 3. 19: Thermal conductivity measurements of silicon using SThM and Raman spectroscopy

3.7 An approach to measure seebeck coefficient using SThM thermal probe

In this section, a technique that measures seebeck coefficient within a bulk sample is demonstrated. In this technique, a thermal probe that serves as a thermometer in conjunction with a Peltier temperature heater is used to measure local thermovoltage. The seebeck coefficient has been measured between the thermal probe contact area and the heated region of the sample.

Previous techniques for measuring seebeck coefficient using SThM required a considerable amount of sample preparation and were costly and time-consuming, whereas in this technique, there is no sample preparation and it is direct measurement. In this technique, a resistive nano thermal SThM probe which comprises pads of gold deposited on a silicon nitride (Si_3N_4) cantilever and a thin resistive Pd film is utilised in the contact mode of the AFM in the both active and passive modes of the SThM. A calibration method was employed for the SThM probe based on international temperature standards. In this method, the benzophenone melting point is used as a calibration reference for SThM equipment, while the calibration of the equipment was undertaken prior to each set of measurements.[123] seebeck

coefficient was evaluated using an AFM XE150 from Park Systems instrument scanning thermal microscopy (SThM).

The SThM has employed in two different mode, active and passive mode. Regarding the passive mode, the probe acts as a thermometer that can measure the temperature of a locally heated place, whereas in active mode, the probe performs as a heater, whereby the probe to sample heat exchange can be measured.

Figure 3-20 illustrates a schematic diagram of the setup of the seebeck coefficient measurement. A temperature sensor was embedded in the heating stage to measure its temperature. A resistive nano thermal SThM probe which comprises pads of gold deposited on a silicon nitride (Si_3N_4) cantilever and a thin resistive Pd film was utilised in the contact mode of the AFM in the passive mode of the SThM. The tip radius is $\leq 100\text{nm}$ with spring constant $\sim 0.45\ \text{Nm}^{-1}$.

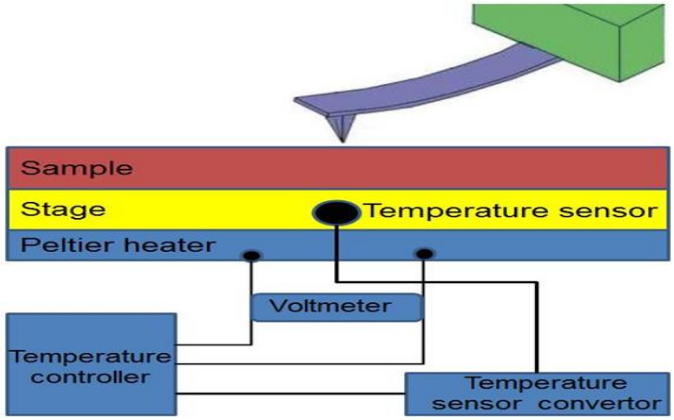

Figure 3. 20: Schematic diagram of the seebeck coefficient measurement setup

The seebeck coefficient *S* is defined as the ratio of $S = \Delta V_s/\Delta T$ when an induced temperature difference ($\Delta T = T_{apex} - T_{stage}$) gives rise to a seebeck coefficient ($\Delta V_s = V_{apex} - V_{stage}$).[137]

A DC electrical power in the Peltier heating stage raises the temperature of the sample (T_{stage}) with a DC voltage (V_{stage}) maintaining the heating stage temperature. V_{stage} was measured using a digital voltmeter. The sample was polished with a fin grinder to make a good contact between the sample and heating stage. The sample was mounted directly on the heating stage for 8 min prior to the measurements. The stage was heated to different temperatures while the voltage maintained these temperatures measured using a sensitive digital multimeter. Figure 3-21 shows the voltage measured using the digital multimeter at the Peltier heating stage as temperature was increased from room temperature up to 370K. To

ensure that the temperature displayed on the temperature controller was like the temperature on the heating stage, a highly sensitive thermometer was also attached to the heating stage to monitor the temperature. The displayed temperature on the controller was similar to the temperature measured by a thermometer. The response is plotted in Figure 3-21.

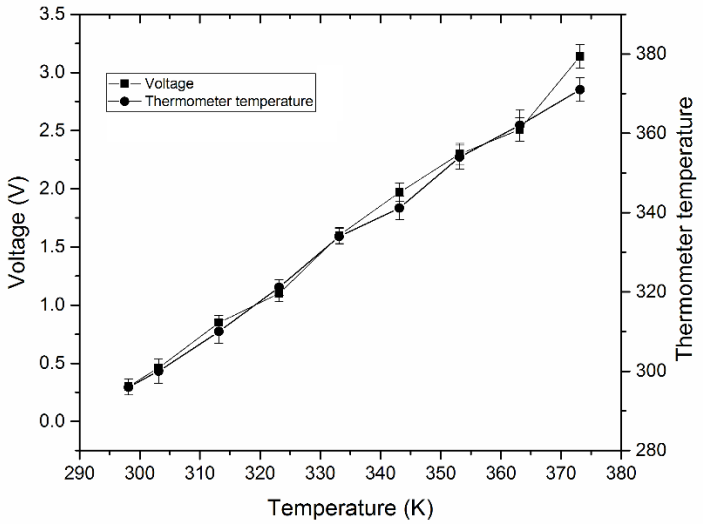

Figure 3. 21: The relationship between the voltage and temperature of the Peltier heater

The sample was mounted on the heating stage at different temperatures while the SThM thermal probe scanned the sample top surface in passive mode and the probe current and probe temperature was measured. The corresponding apex temperature (T_{apex}) was extracted using the apex-probe temperature relationship described in Figure 3-10. The apex temperature represents the induced Seebeck temperature.

Considering the electrical resistivity of the probe (ρ_0) at the ambient temperature $T_0 = 300\ K$ and the temperature coefficient of resistance (TCR) of the probe, and then V_{probe} can be written as $V_{probe} = I_{probe}\,\rho_0\,(1 + \alpha\Delta T)$. The probe's electrical resistance ρ_0 without joule heating was measured using an Agilent 34401A multimeter. The manufacturer stipulates that the probe's TCR must be 0.00165 mK^{-1}, which was established by means of measuring the probe's electrical resistance as a function of temperature yielding the same result. The TCR does not change noticeably with temperature, causing a linear relationship between its temperature and resistance. The measured I_{probe} and T_{apex} was used to extract the V_{probe} which represent the induced Seebeck voltage.

3.7.1 Seebeck coefficient measurement of silicon sample

The technique was also applied to measure the seebeck coefficient of silicon. The silicon wafer was cut to a $1\ \text{cm} \times 1\text{cm} \times 525\ \mu\text{m}$ sample. The silicon sample was mounted on the heating stage to evaluate the seebeck coefficient at different temperatures. The induced temperature and voltage of the silicon sample were measured at various temperatures and the value of ΔT and ΔV_s were calculated and the sample seebeck coefficient extracted. Figure 3-22 shows the seebeck coefficient measurement of the silicon sample at different temperatures. The seebeck coefficient increased with temperature, indicating p-type silicon.

At room temperature, the seebeck coefficient is $200\ \mu\text{VK}^{-1}$. This is close to the measured reported value for this material.[32] The silicon sample exhibits a value of $480\ \mu\text{VK}^{-1}$at 420 K which shows an increase of $280\mu\text{VK}^{-1}$. This agrees with literature at elevated temperature.

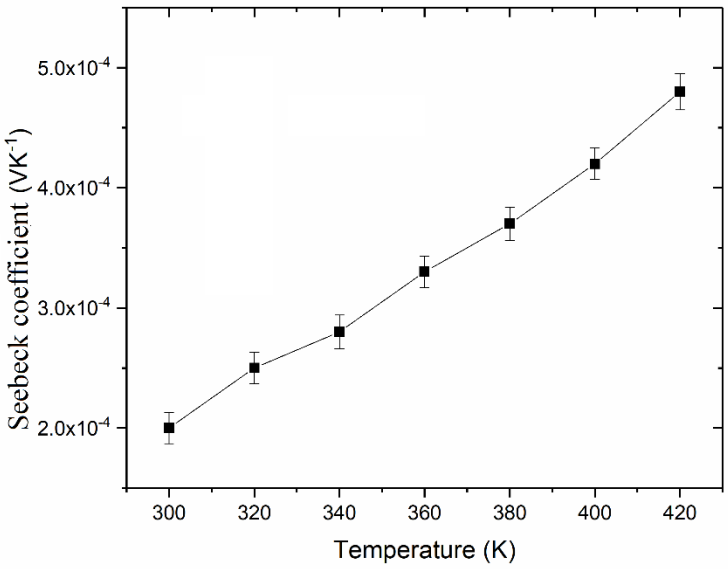

Figure 3. 22: Seebeck coefficient measurement of silicon

3.8 Conclusion

Experimentally probe and probe-to-sample thermal conductance based on the electrical power dissipation in the probe and the sample, and several samples thermal conductivity have been measured. The experimental results show the temperature of the

SThM thermal probe varies by one order of magnitude that leads to a 5% different in the thermal conductivity measurements.

The SThM enables individual contributions to thermal conductivity to be determined. As the dimensions of the SThM probe are at a submicron scale, effective thermal conductivity can be ascertained. The intrinsic thermal conductivity of the copper material has been examined using SThM. The calculated electronic contribution of the thermal conductivity in conjunction with the intrinsic thermal conductivity measurement using the SThM confirm the total thermal conductivity of the copper material.

The SThM allows individual metal content cluster such as nickel nanoparticles, to be studied. The thermal conductivity of nickel nanoparticles in silica aerogel has been studied and shows that the thermal conductivity of the nanoparticle cluster changes notably compared with the bulk nickel.

A technique to measure the seebeck coefficient using the SThM was proposed. In this technique the SThM thermal probe in passive mode in conjunction with a Peltier heater was used to measure the temperature and the induced current. Considering the thermal probe electrical resistance and probe current the induced seebeck coefficient has been extracted. The proposed method has been used to measure the seebeck coefficient of the silicon. The results are in good agreement with reported seebeck coefficient for these materials.

Chapter 4

Thermoelectric characterization of nickel-nanoparticles embedded in silica aerogels

4.1 Introduction

The challenge in creating high-performance thermoelectric materials lies in simultaneously achieving high Seebeck coefficients, high electrical conductivity, besides low thermal conductivity. These parameters are temperature dependent and are closely associated in such a way that by enhancing one parameter the other parameter changes and most often deteriorates.[140]

Thermal conductivity can be significantly reduced by increasing the number of phonons scattering centres within materials.[140-143] Phonon scattering inside porous materials can be controlled by the porosity because phonons scatter from pore boundaries. Pore size, shape and orientation affect thermal conductivity.[143-145] The incorporation of nanostructures also lowers thermal conductivity and improves the thermoelectric properties by introducing phonon scattering centres.[141]

Silica aerogel is of interest to thermoelectricity fundamentally and at applied level due to its extremely low thermal conductivity ($0.017\ \mathrm{Wm^{-1}K^{-1}}$)[147-149]. Potential applications include not only thermal insulation, but also infrared detectors,[145] microelectronic devices[146] and in space exploration.[147]

The thermal and electrical properties of silica aerogel can be modified by incorporating nanomaterials. Metal nanoparticles inserted into the aerogel improve its electrical conductivity [148-150] to values relevant to thermoelectric materials and enabling potential applications in carbon capture.[151]

Investigations of the thermal properties of silica aerogels by the addition of nanostructures have been reported.[152] The thermal conductivity of a nanowire can be reduced substantially by embedding it in an aerogel medium. For instance, the thermal conductivity of ZnO nanowires has been diminished by more than a factor of ten in the temperature range of 150 to 300 K when they were embedded into silica aerogel.[152] This reduction of thermal conductivity resulted from scattering of ballistic phonons at nanowires boundaries.[152] Bi_2Te_3 and $Bi_{2-x}Sb_xTe_3$ aerogels prepared by the sol-gel method have also been synthesised and characterised.[153] The thermal conductivity was decreased from $1.7\ \mathrm{Wm^{-1}K^{-1}}$ to

$0.5\ \mathrm{Wm^{-1}K^{-1}}$ for Bi_2Te_3, while it remained unchanged for $Bi_{2-x}Sb_xTe_3$.[153] However, the room temperature thermoelectric power factor, which relates to electrical conductivity, was $3.3 \times 10^{-4}\ \mathrm{Wm^{-1}K^{-2}}$ for $Bi_{2-x}Sb_xTe_3$ and $5.0 \times 10^{-4}\ \mathrm{W\,m^{-1}K^{-2}}$ for Bi_2Te_3.[153]

A highly versatile silica sol–gel process has increased the electrical conductivity of Pd embedded in silica aerogel by three orders of magnitude.[154] This increase results from the formation of Pd metallic percolation networks.[154] RuO_2 nanoparticles similarly generated a wired RuO_2 network at the surface of silica, with an electrical conductivity as high as $10^{-3}\mathrm{S\ cm^{-1}}$,[155] while similarly a porous silica-graphene nanocomposite exhibits a conductivity of $0.5\ \mathrm{S.cm^{-1}}$.[156] Despite the promising results from the development of these materials, their characterisation remains incomplete since several key thermoelectric properties have not yet been evaluated. In particular, there are no reports of silica-based aerogel materials that provide information on both the thermal and electrical conductivity.

This chapter describes the characterisation of nickel nanoparticles (NiNPs) embedded in silica aerogels at various temperatures with the aim of evaluating key thermoelectric properties. Although silica aerogel is not the ideal thermoelectric material, it is being used to assess the potential of the material and explore whether characterisation technique work on this porous material. Electrical conductivity is studied by four-point probe measurements[157] and by Hall effect equipment, while thermal conductivity is measured by using the Hot Disk Transient Plane Source method (with a Hot Disk TPS 2500 S) and with SThM. In this thesis a full thermoelectric evaluation of silica-based aerogels with embedded Ni nanoparticles has reported. The work shows that by optimising the concentration of NiNPs, a silica aerogel composite may be potentially considered as a valuable thermoelectric material.

4.2 Experimental details

Silica aerogel materials containing embedded NiNPs were fabricated via the sol-gel process and ambient pressure drying.[151] The concentrations of NiNPs embedded in silica aerogels were 500, 700, 900, and 0 ppm. The sample sizes were prepared into $0.5\ \mathrm{mm} \times 0.6\ \mathrm{mm} \times 0.1\ \mathrm{mm}$ for the length, width and thickness, respectively using a sharp scalpel. An average diameter of $40\ nm$ of NiNPs was established by way of statistical analysis of the TEM images.[151] A TEM image of NiNPs is shown in Figure 4-1.

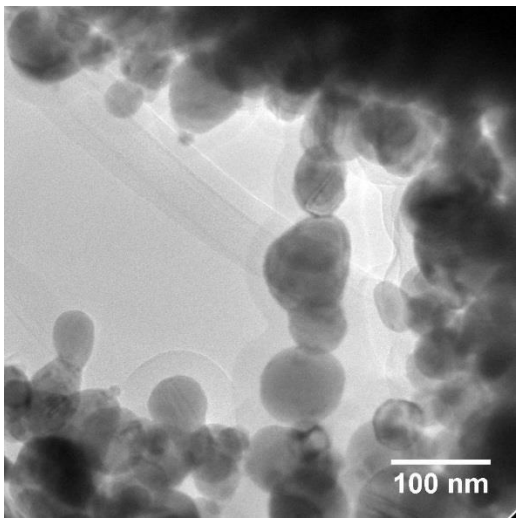

Figure 4. 1: TEM image of NiNPs[151]

The thermoelectric properties of the silica aerogel samples at various temperatures have been examined and reported in this chapter, except for the silica aerogel embedded with NiNPs at 900 ppm concentration. This is because during the silica gel preparation with 900 ppm of NiNPs, nickel nanoparticles will collect at the bottom during synthesis and the sample did not show any further increase in the NiNPs concentration in the final aerogel product.[151]

The electrical resistivity was measured by the van der Pauw method using two techniques. Four-point probe measurements were made with a CASCADE 4200SCS probe station from Keithley, and a Hall effect system was also used. The benefit of using van der Pauw's technique is that it avoids inaccuracies arising from the sample geometry.[157] Four small gold contacts were deposited using a thin film deposition system (Kurt Lesker PVD 75) on the edges of the samples. The electrical resistivity was measured from ambient temperature (300 K) to 423 K under atmospheric conditions. The uniformity of the material was assessed in terms of electrical resistivity, thermal conductivity by making multiple measurements on each sample.

Temperature dependent thermal conductivity and Seebeck coefficients in the range of 300 K to 423 K were also measured using an atomic force microscope (AFM XE150 Park Systems) in SThM mode with a heating stage in passive mode. The SThM is based on Joule dissipation within the probe-sample system. The SThM experiments were conducted in conjunction with a Peltier heating stage controller, which enables the measurement of the Seebeck coefficient. The thermal conductivity results were obtained using the Hot Disk Transient Plane Source method.

4.2.1 Determining error in the test system

Electrical resistivity measurements were performed using the van der Pauw method on the silica aerogel doped with NiNPs at two different concentrations of 500 ppm and 700 ppm.

The error in the test system was determined by repeating measurements at the same place on the surface of the sample without lifting the contact probes.

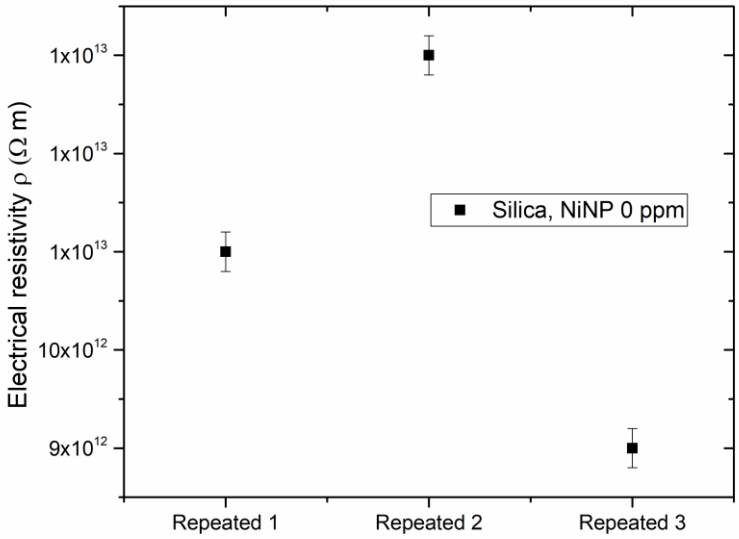

Figure 4-2: Electrical resistivity measurements of undoped silica aerogel

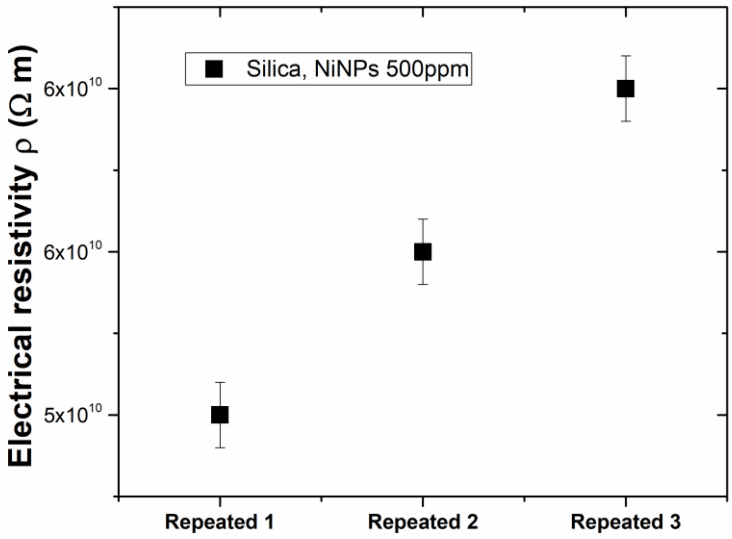

Figure 4-3: Electrical resistivity measurements of silica aerogel at a concentration of 500ppm

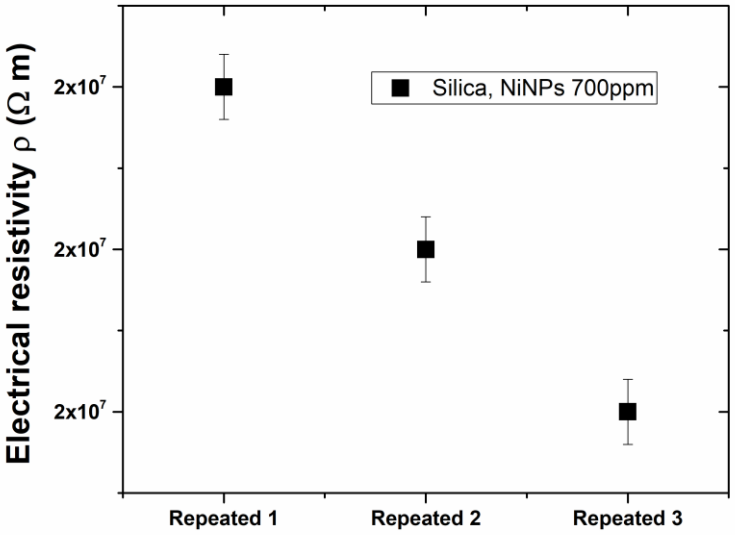

Figure 4-4: Electrical resistivity measurements of silica aerogel at a concentration of 700ppm

Figures 4-2 to 4-4 show that there is no trend in electrical resistivity within the repeated measurements. In order to compare the error within the test system between the samples having very different values of resistivity, the standard deviation of data / median data point for each sample were calculated (Figure 4-5).

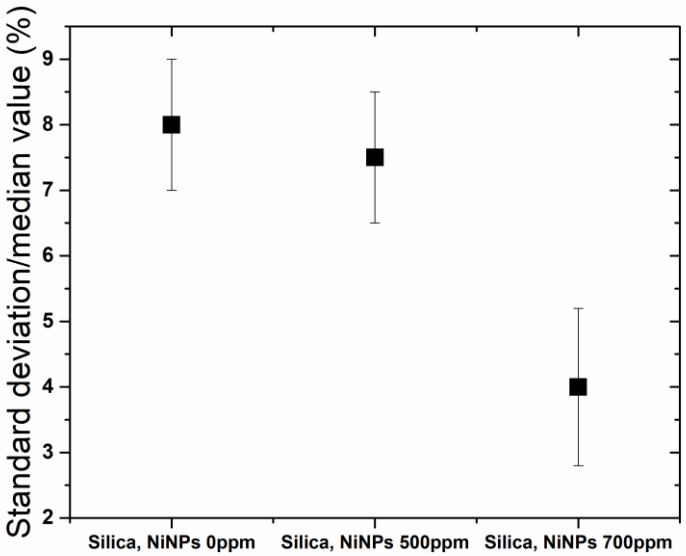

Figure 4-5: Standard deviation of data / median data point for silica aerogel doped with NiNPs at three different concentrations

Figure 4-5 shows that the Ni-doped samples have less variation than the control. However, there is no reason for the test system repeatability (variation) to be larger for Ni-doped samples compared with silica aerogel. Therefore, the error due to the test system for future measurements is considered to be in the range 4-8% of the standard deviation / median for all samples.

4.2.2 Impact of contact resistivity on electrical resistivity measurement

To determine the effect of the probe contact resistivity on the resistivity measurements, three measurements were performed in the same location on the sample after lifting and re-contacting the probes on the surface of the sample each time.

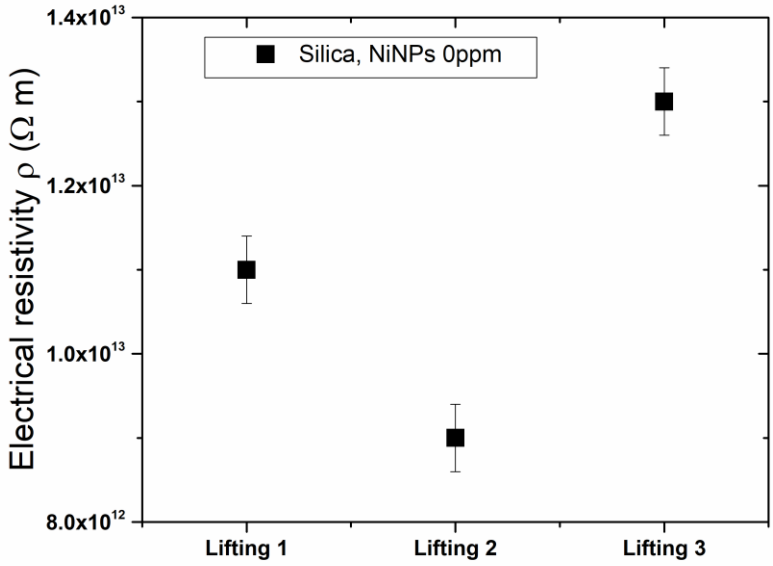

Figure 4-6: Electrical resistivity measurements of silica aerogel

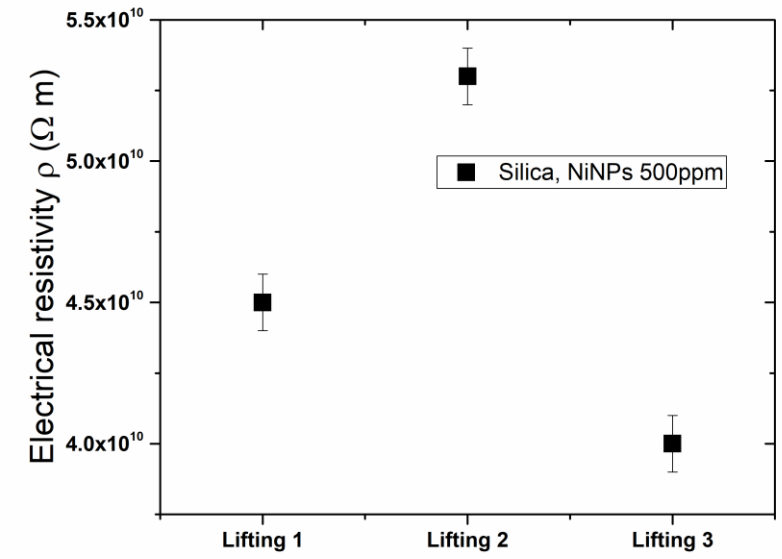

Figure 4-7: Electrical resistivity measurements of silica aerogel NiNPs at 500 ppm

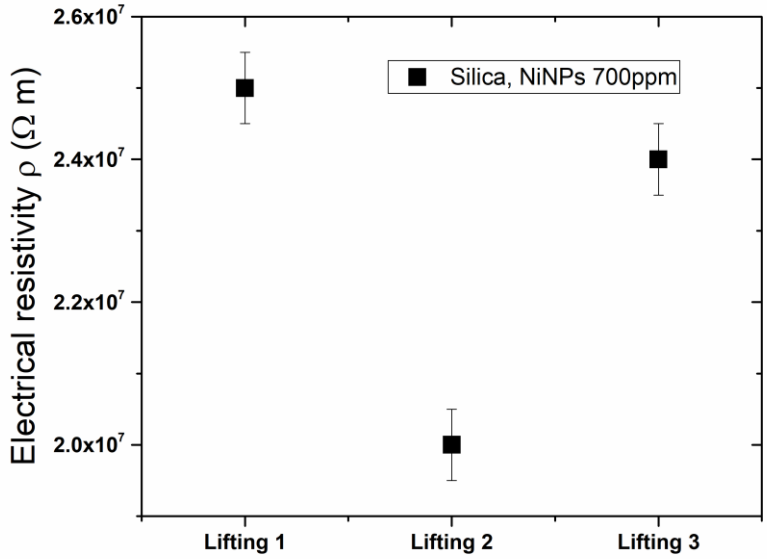

Figure 4-8: Electrical resistivity measurements of silica aerogel Ni at 700 ppm

Figures 4-6 to 4-8 shows that contact resistance (placing the probes) affects the measured resistivity but there is no consistent trend with the number of measurements.

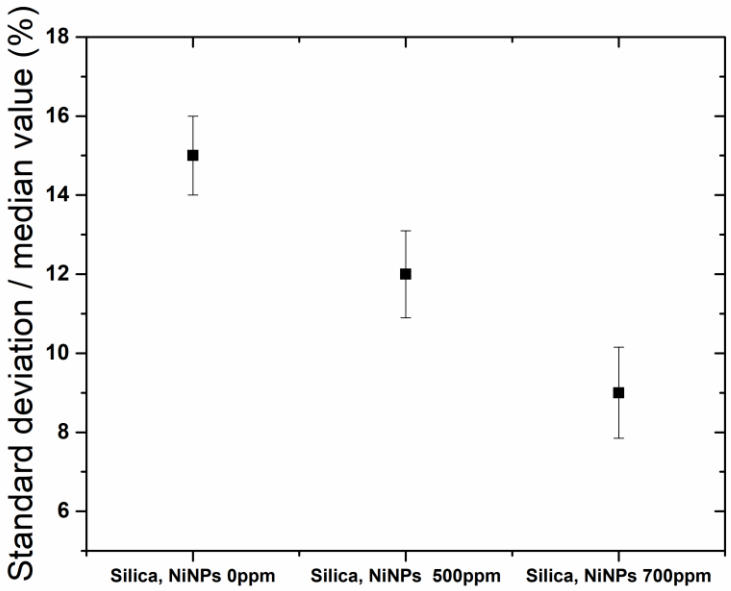

Figure 4-9: Comparison of variation due to the lifting probe for each sample

The variation in resistivity due to replacing the probe is 9-15%. The standard deviation of the median as shown in Figure 4-9, is greater than the variation as a result of repeating the measurements at the same place without lifting the probes is 4-8%, as shown in Figure 4-5.

4.3 Electrical resistivity measurement

The temperature dependence of electrical resistivity for silica aerogel with NiNPs concentrations of 0, 500 and 700 ppm were investigated (see Figure 4.10). Median values of electrical resistivity were found to be in the range of 10^{13}, 10^{10} and 10^{7} Ωm at room temperature (300K) for undoped silica aerogel, silica aerogel with 500 ppm NiNPs and silica aerogel with 700 ppm NiNPs, respectively.

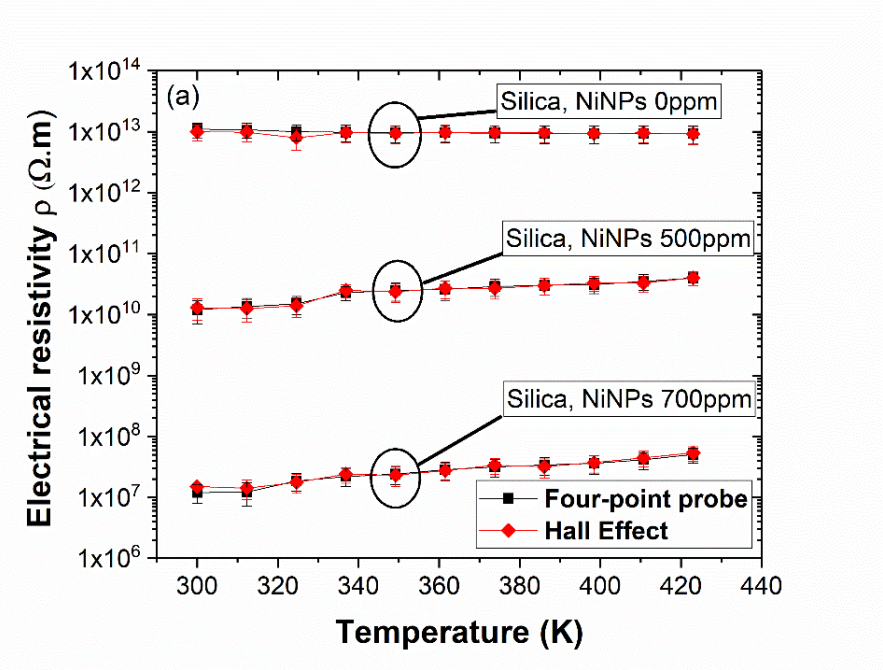

Figure 4-10: The electrical resistivity temperature dependence for silica aerogel at two different concentrations (500 and 700 ppm) of NiNPs and pure silica aerogel (0 ppm) using two different techniques

The electrical resistivity of silica aerogel is reduced by six orders of magnitude when embedded with 700 ppm NiNPs compared with undoped silica aerogel, whereas the silica aerogel embedded with 500 ppm NiNPs exhibits three orders of magnitude resistivity reduction compared with the undoped silica aerogel.

The variation in electrical conductivity with weight fractions (Wt%) of NiNPs in silica aerogels is shown in Figure 4-11. There is a six orders of magnitude increase in the electrical conductivity when the weight fraction of NiNPs in silica aerogels is increased from 0 to 4.9 Wt%. Electrical conductivities of composite silica samples have been analysed in relation to the threshold weight concentration of NiNPs fractions. The scaling law of percolation theory was used, $\sigma \propto (W - W_c)^t$, where W is the weight fraction of the filler, W_c is a critical weight fraction of the filler and σ is an electrical conductivity.[159-160] It should be stated that the conductivity exponent, t, mostly reflects the system's dimensionality. For example, in carbon systems it has a typical value of 1-1.3 and 1.6-2.0 for 2D and 3D, respectively.[161] In this work, to obtain the best fit values were used for the conductivity exponent of t~ 2.2 for NiNPs in aerogels. The insets in Figure 4-11 represent the most appropriate fit for the experimentally measured electrical conductivity data as a function of $W - W_c$, stated as a fraction of weight. Moreover, this analysis demonstrates a percolation threshold of approximately 0.08-0.1 Wt%

for NiNPs in silica aerogels, respectively. The calculated percolation threshold for silica aerogels are in good agreement with the reported percolation threshold for silica aerogel composites.[162] Electrical measurements showed that the additional NiNPs in silica aerogels make an effective interaction between fillers and form a conductive percolation network, thereby enhancing the electrical conductivity.

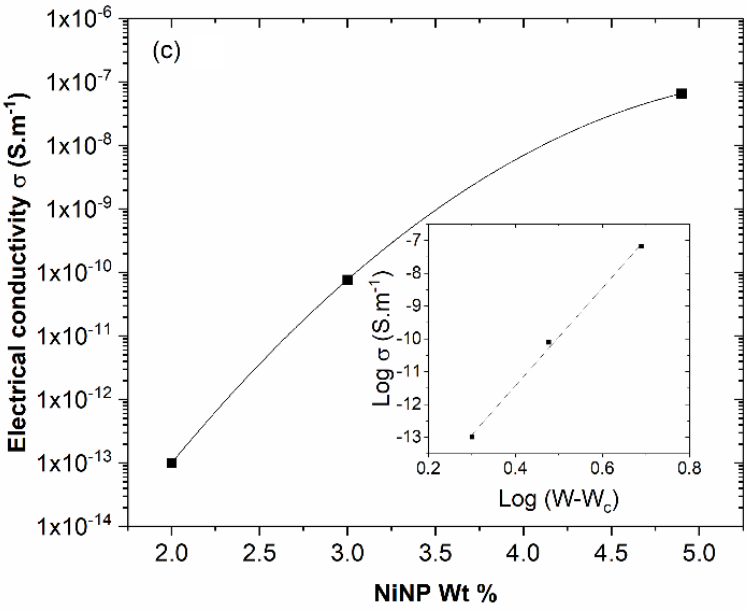

Figure 4-11: Variation in electrical conductivity with weight fractions of embedded silica at a weight fraction. Inset: variation in electrical conductivity with $(W - W_c)$, NiNPs

At room temperature, the standard deviations of the median values of nine resistivity measurements for the NiNPs aerogel samples were within 5-6% (using four-point probe techniques) and 5-7% (using Hall effect equipment). The insignificant variations in electrical measurements for all the samples demonstrates that incorporation of NiNPs does not degrade material uniformity, which is essential for device-grade material. Figure 4-10 shows that there is a small decrease in the resistivity of pure silica aerogels as the temperature increases, whereas the aerogels containing NiNPs exhibit a metallic behaviour[163], showing an increasing resistivity with increasing temperature. The electrical resistivity of silica aerogel embedded with 700 ppm NiNPs increases by approximately 250% at 420 K compared with its resistivity at 300 K, whereas the increase is approximately 200% for silica aerogel embedded with 500 ppm NiNPs. The electrical resistivity of pure silica aerogels decreases by 16% at 420 K compared with that at 300 K.

SThM was used to measure the Seebeck coefficient (S) for all silica aerogel samples. The Seebeck coefficient was used to extract the sample thermoelectric power factor, $s^2\sigma$. The

Seebeck coefficient of a material is a measure of the extent of the voltage generated regarding a temperature change. Median values of room temperature (300 K) Seebeck coefficient almost the same for all the samples. It is in the range of 1.824×10^{-3} VK^{-1} for pure silica aerogel, and silica aerogel embedded with 500 ppm NiNPs and 700 ppm NiNPs.

The standard deviation of the median values of the Seebeck coefficient from nine measurement locations of all NiNP samples is within 8-9%, showing good material uniformity.

The thermoelectric power factor of the samples is calculated for different temperatures and data are shown in figure 4.12. Figure 4.12 also shows there is a 10^6 increase in power factor due to the increase in NiNP concentration from 0 to 700 ppm, while a 10^3 increase in power factor is observed as the density of the NiNPs increases from 0 to 500 ppm. These results confirm previous reports that nanostructuring is a promising method to improve thermoelectric properties of materials.[164] Nanostructures offer an opportunity to split the connection between electrical and thermal transport by establishing new scattering mechanisms.[164]

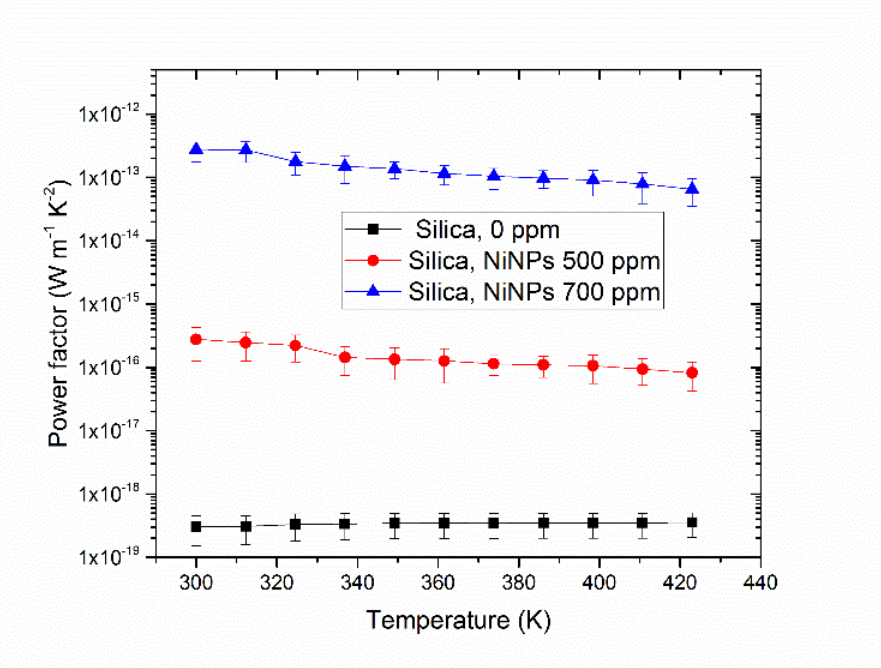

Figure 4-12: Thermal properties showing the enhancement in power factor compared with pure silica aerogel (0 ppm) for the NiNPs samples

4.4 Thermal conductivity measurement

The thermal conductivity of the samples was measured using SThM and the results were validated with a HotDisk analyser. Data for temperature dependent thermal conductivity measurements are presented in the figures 4-13 and 4-14 for the NiNPs samples using SThM and HotDisk analyser, respectively. There is an excellent agreement between the two techniques. At 300 K, the thermal conductivity remains constant as the density of the NiNPs increases from 500 ppm to 700 ppm and there is only a slight increase in thermal conductivity (5×10^{-3} W.m^{-1}. K^{-1}) compared with the pure silica aerogel. Median values of thermal conductivity from nine SThM measurements around the samples are 25×10^{-3} $Wm^{-1}K^{-1}$, 30×10^{-3} $Wm^{-1}K^{-1}$and 30×10^{-3} $Wm^{-1}K^{-1}$ for the pure silica, silica with 500 ppm NiNPs and silica with 700 ppm NiNPs, respectively. The median value of thermal conductivity from nine HotDisk analyser measurements are 25×10^{-3} $Wm^{-1}K^{-1}$, 29×10^{-3} $Wm^{-1}K^{-1}$ and 30×10^{-3} $Wm^{-1}K^{-1}$ for the pure silica, silica with 500 ppm NiNPs and silica with 700 ppm NiNPs, respectively. The lower thermal conductivity in the NiNPs samples could be due to grain boundary scattering, since the grain boundary scattering plays a major role in conductivity decrease as the size approaches the electron mean free path.[165]

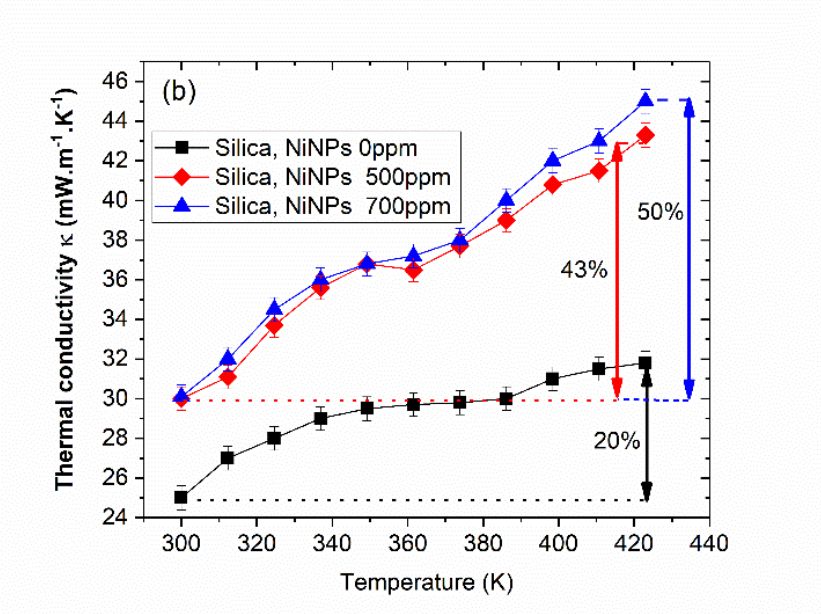

Figure 4-13: Thermal conductivity of the silica aerogel embedded with NiNPs samples by SThM

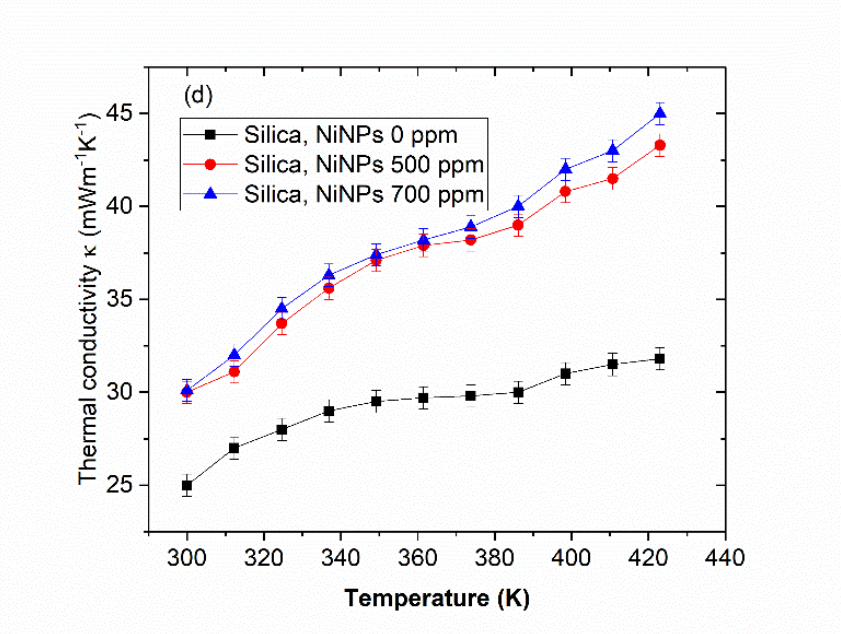

Figure 4-14: Thermal conductivity of the silica aerogel embedded with NiNPs samples by HotDisk analyser

The thermal conductivity of the pure silica aerogel is in good agreement with values reported in the literature.[166] The improvement in electrical resistivity by incorporating NiNPs, while simultaneously maintaining a low thermal conductivity, demonstrates the huge potential of these NiNPs embedded in aerogel as thermoelectric materials.

The total thermal conductivities of the NiNPs silica composites are a combination of lattice and electronic thermal conductivity.[167] It is essential to distinguish between the lattice and electronic thermal conductivity to understand the role of electrons and phonons in thermal conduction. The electronic component of the thermal conductivity k_e was calculated by the Wiedemann-Franz equation, $k_e = LT/\rho$, where T is temperature and L is the Lorentz number, $L = 2.44 \times 10^{-8}\ \mathrm{V^2K^{-2}}$.[27] Additionally, the electronic element in relation to the thermal conductivity has a negligible effect on the total thermal conductivity, because it is very small, of the order of $10^{-19}\ \mathrm{Wm^{-1}K^{-1}}$ in the undoped silica aerogel at 300 K. Therefore, it is assumed that the measured thermal conductivity of undoped silica aerogel is a lattice (effective) thermal conductivity.

As the temperature increases from 300 to 420 K in the silica samples, the phonon mean free path increases and the lattice vibrations dominate the thermal conductivity. Consequently, the thermal conductivity increases and causes a reduction in the Seebeck coefficient of both the pure silica aerogel and the silica aerogel embedded with NiNPs. The

increase in thermal conductivity at elevated temperatures is substantially larger for the silica aerogel embedded with NiNPs than for the pure silica aerogel. This is attributed to radiative heat transfer. [168] Heat transfer through radiation takes place in the form of electromagnetic waves, which is a consequence of the thermal agitation of the material's molecules or charged particles. For the pure silica aerogel at 420 K, the thermal conductivity is 20% higher than the thermal conductivity at 300 K. However, for the silica aerogel embedded with 500 ppm NiNPs it is 43% larger than at 300 K, and for the silica aerogel embedded with 700 ppm NiNPs, it is 50% larger that at 300 K. At 400 K, the thermal conductivity of silica aerogel embedded with 700 ppm NiNPs is increased by 7% compared with the 500 ppm NiNPs silica. This increase in thermal conductivity with an increase in temperature is due to the domination of lattice vibrations that are responsible for heat conduction.

Water presence inside the aerogel pores can have effect on thermal conductivity, so the thermal conductivity of the silica (700 ppm NiNPs) was measured using SThM, firstly as the temperature was increased from 300 to 420 K and then when the temperature was decreased from 420 to 300 K. There is a 2×10^{-3} $\mathrm{Wm^{-1}K^{-1}}$ difference in measured thermal conductivity at 300 K and a difference of 3×10^{-3} $\mathrm{Wm^{-1}K^{-1}}$ at 410 K. The silica aerogel sample was placed in contact with the heating stage for 30 minutes prior to performing the measurement to obtain the thermal equilibrium condition. However, the thermal conductivity which sweeps at 423 K was completed simultaneously. Figure 4-15 contains the thermal conductivity sweep measurement. The change in thermal conductivity measurements is likely to be due to the evaporation of water inside the pores when the temperature starts to increase. The increased thermal conductivity at higher temperature explains the reduced power factor observed at higher temperature in Figure 4-12.

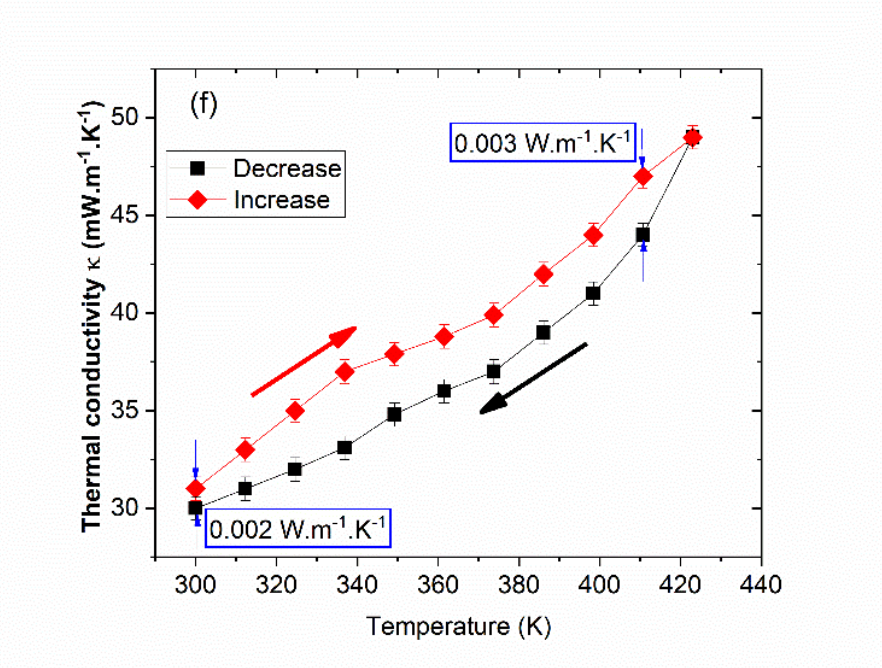

Figure 4-15: Effect of water on thermal conductivity using SThM for silica aerogel embedded with 700 ppm NiNPs.

4.5 Thermoelectric figure of merit (ZT)

All measured thermal and electrical parameters have been used to calculate the overall ZT (see Figure 4-16). There is an improvement in ZT of 3 and 6 orders of magnitude for silica with 500 ppm and 700 ppm NiNPs, respectively, compared with pure silica at room temperature (300 K). Room temperature ZT values reached 5.27×10^{-15}, 4.8×10^{-12}, and 4.8×10^{-9}, for pure silica, silica with 500 ppm NiNPs and silica with 700 ppm NiNPs, respectively. The results show that the thermoelectric properties of silica aerogel material can be improved further by utilising silica aerogel with an increased NiNP concentration. This may decrease electrical resistivity further, thereby enabling this material to become a potential thermoelectric material in the future.

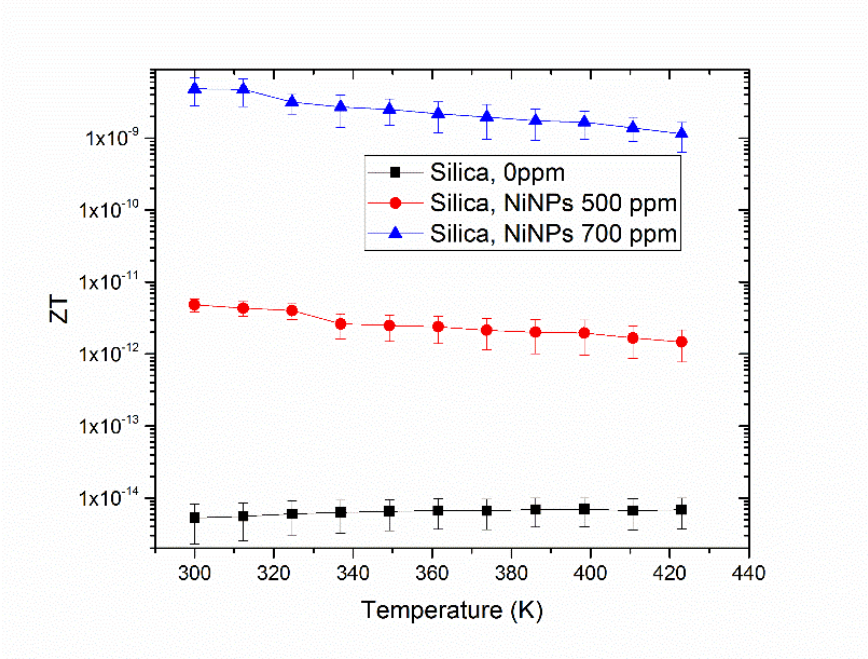

Figure 4-16: ZT of the samples at different temperatures

4.6 Conclusion

Embedded NiNPs in silica aerogels at three different concentrations are characterised by scanning thermal microscopy, a Hot disk method and four probe measurements to consider them as potential thermoelectric materials. NiNPs samples exhibit a 6 orders of magnitude improvement when the concentrations are increased from 0 to 700 ppm. The electrical resistivity is highly sensitive to the concentration NiNPs in the silica aerogels, while the thermal conductivity remains largely unchanged. The electrical conductivity σ is shown to follow a percolation scaling law of the form $\sigma \propto (W - W_c)^t$ with critical weight fraction (W_c) to form a conductive network of approximately **0.08-0.1** Wt% for embedded NiNPs, respectively. The preliminary investigation and results suggest that optimising the concentration of NiNPs could yield promising thermoelectric properties.

Chapter 5

Development and characterisation of Zn_4Sb_3 based material

5.1 Introduction

Zn_4Sb_3 is one of the best thermoelectric materials for operation at room temperature. The extremely high ZT value of Zn_4Sb_3 is due to its low thermal conductivity, as discussed in Section 1.8.[169-171] The high ZT value combined with the low cost and availability of its raw materials make Zn_4Sb_3 one of most the interesting thermoelectric materials. Its low thermal conductivity arises from high levels of interstitials and corresponding local structural distortions.[172-175] The dimensionless ZT of bulk Zn_4Sb_3 reaches a values of 1.3 at a temperature of approximately 600K which is much higher than that of bulk Bi_2Te_3 material at this temperature.[176-178] The ZT of bulk Bi_2Te_3 decreases with temperature, whereas for bulk Zn_4Sb_3 material, it increases with temperature.[171] Bi_2Te_3 is one of best room temperature thermoelectric materials and it is used widely in thermoelectric generators. The value of ZT can be improved either by increasing electrical conductivity (increasing the power factor) or by means of reducing the thermal conductivity. Further improvements in thermoelectric properties are necessary to increase efficiency in practical applications. Doping is effective in improving the ZT value by increasing electrical conductivity and consequently improving the power factor. However, it has been established that doping Zn_4Sb_3 is challenging because it decreases the Seebeck coefficient and consequently decreases the power factor.[176] Moreover, nanostructuring has been noted to be an valuable method in regard to diminishing thermal conductivity, while maintaining the electrical properties of thermoelectric materials (see Section 1.7).[176] Zn_4Sb_3 nanowires have been reported to have the highest ZT=1.59 as a result of the extremely low thermal conductivity of the material.[177]

In this chapter, a method is shown that can lessen the thermal conductivity of Zn_4Sb_3 by employing porosity, consequently improving ZT. The molecular dynamic (MD) simulation of Zn_4Sb_3 demonstrates that nanopores could possibly reduce the thermal conductivity as a result of the phonon scattering effect created by the nanopore boundaries.[176] The MD study indicates that at a porosity of 40%, the ZT value could be increased to 2.32 at room

temperature (300K). This enhancement in ZT can increase the efficiency of devices by a factor of 14, as discussed in Section 1.6.

Chemical synthesis is one method that can potentially improve the ZT value. Here, a chemical solution connects the nanocomposites together so that the material consists of the same chemical constituents.[179] This can be achieved by using an aerogel. In addition to material synthesis, the gel that is attained by means of this specific method offers extra pore-matter interfaces that will further scatter heat-carrying phonons, causing a reduction in regard to the lattice thermal conductivity.[179] The thermoelectric characterisation of silica aerogel embedded with nickel nanoparticles has been demonstrated in Chapter 4. The silica aerogel embedded with nickel nanoparticles exhibits a reduction of six orders of magnitude in electrical resistivity compared with pure silica aerogel while thermal conductivity stays constant.[179-180] This produced the characterisation and synthesis of the thermoelectric properties of Zn_4Sb_3 material embedded in silica aerogel. In this chapter, the thermoelectric properties of bulk Zn_4Sb_3 are first characterised. Then the synthesis and characterisation of embedded Zn_4Sb_3 nanoparticles in porous silica aerogel are described. Finally, a comparison is made of the thermoelectric properties of Zn_4Sb_3 nanoparticles in porous silica aerogel compared with those of bulk Zn_4Sb_3.

5.2 Silica aerogel preparation

The synthesis of aerogel involves the transition of a system from a liquid ‘sol’ into a solid ‘gel’ phase. Sol-gel processing implies one of two techniques. It can be produced in a network that is inorganic by way of a chemical reaction in solution at low temperatures. Alternatively, it can involve the development of an amorphous network as against crystallisation from solution. The sol-gel process can be separated into the following stages; forming the solution, gelation, ageing, drying, in addition to densification.[181-182]

It is important to note that a sol is a colloidal suspension of solid particles in a liquid, which means that the dispersed stage is extremely small (1–1000 nm). It can be made using one of the following two techniques: the dispersion of particles or condensation. The condensation method includes the nucleation growth of particles to the appropriate size; however, dispersion comprises a reduction in the size of much bigger particles down to the colloidal dimensions. The size and properties of the subsequent particles is dependent on the relative rates of both methods.[181-183]

5.3 Preparation and characterisation of Bulk Zn_4Sb_3

The synthesis and compaction of bulk Zn_4Sb_3 was achieved using spark plasma sintering (SPS). The bulk Zn_4Sb_3 synthesised using SPS came from Aarhus University in Denmark. In this technique, zinc powder with a purity of 99.99% and grain size of < 45 µm was provided by MERCK KGaA. The antimony powder with a purity of 99.5% and grain size of < 150 µm has been provided by SIGMA-Aldrich CHEMIE GmbH. They were weighed to a molar ratio of 4:3 (Figure 5-1). The SPS instrument uses both temperature and pressure to make the Zn_4Sb_3 bulk. The Zn_4Sb_3 bulk size is 2 mm in thickness and 2.2 cm in diameter.[184]

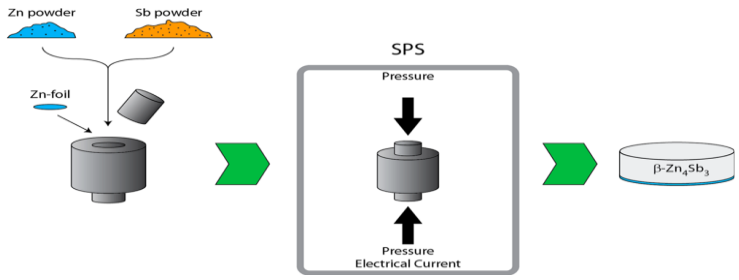

Figure 5. 1: SPS technique used to make bulk Zn_4Sb_3 [184]

The thermoelectric properties of the bulk Zn_4Sb_3 were studied using various techniques such as the four-probe method and SThM. The electrical resistivity of the sample has been measured using the four-point probe and the results compared with Hall-effect measurements. The Seebeck coefficient and thermal conductivity were measured using SThM and the thermal conductivity values were validated using a HotDisk analyser and Raman measurement. The bulk Zn_4Sb_3 was cut into $2\ mm \times 2\ mm \times 2\ mm$ rectangles using a CNC wire-cutting machine. This small size enables the sample to be handled more easily using the characterisation tool.

5.3.1 Electrical characterisation of bulk Zn_4Sb_3

In order to measure the electrical resistivity of the Zn_4Sb_3, four gold contacts were deposited using e-beam evaporators in the fabrication clean room at the corners of the sample. The temperature dependence of electrical resistivity was measured using the four-point probe on CASK4200 and the results are displayed in Figure 5.2. The measured electrical resistivity data are then compared with Hall-effect measurements. Furthermore, the electrical resistivity measurements in relation to the bulk Zn_4Sb_3 at room temperature are $1.62 \times 10^{-5} \Omega$ m and

$1.65 \times 10^{-5}\Omega$ m for the four-point probe and Hall effect technique respectively where the difference is statistically significant at room temperature. These results are in good agreement with reported electrical resistivity measurements for bulk Zn_4Sb_3 thermoelectric material.[185] The median value of electrical resistivity was established to be in the range of $1.6 \times 10^{-5}\Omega.\,\mathrm{m}$ at room temperature. The electrical resistivity increased by 50% as the temperature rose from 300K to 420K.

The electrical resistivity of the sample was analysed against temperature and the results are observed to be in good agreement with the reported electrical resistivity of the Zn_4Sb_3 thermoelectric material.[185-186] At increased temperature, the atoms within the Zn_4Sb_3 material vibrate more. This vibration prevents the electrons from flowing and they are more likely to collide with each other, thus increasing resistance.

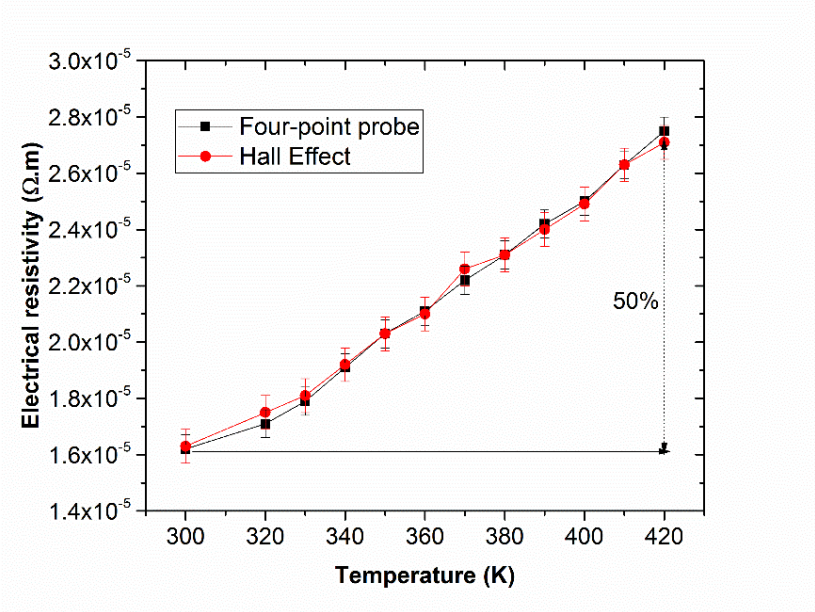

Figure 5-2: Electrical resistivity of bulk Zn_4Sb_3 measured using two techniques at various temperatures

A. Analysis material uniformity of bulk Zn_4Sb_3

To investigate the uniformity of the bulk Zn_4Sb_3, resistivity was measured in three different locations on the sample. The standard deviation of median values at three different locations are then plotted. The error bars show small variations in the electrical measurements for the sample, suggesting good material uniformity as shown in Figure 5-3. At room temperature, the standard deviations of the median values of three resistivity measurements

for the bulk Zn_4Sb_3 sample were between 4-5% using the four-point probe techniques and between 5-7% using Hall effect equipment.

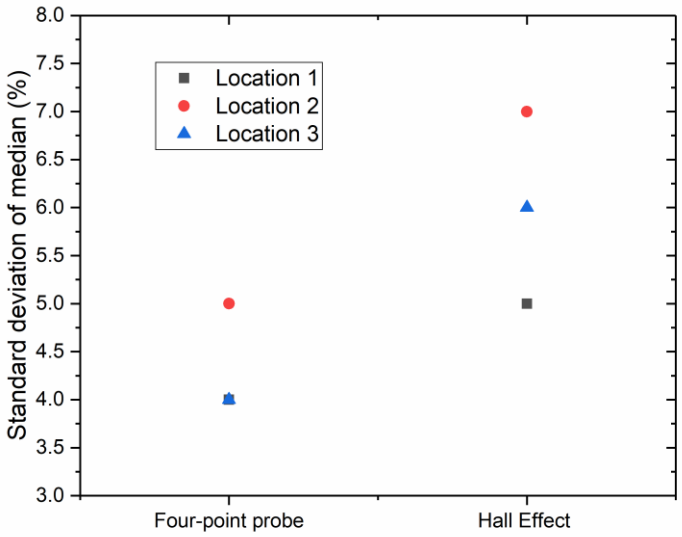

Figure 5. 3: Standard deviation of median value at three different locations

B. Impact of contact resistivity on electrical resistivity

In order to determine the effect of the probe contact on the resistivity measurements of Zn_4Sb_3, three measurements were performed in the same location on the sample after lifting and re-contacting the probes with the surface of the sample each time. The electrical resistivity measurements show that contact resistance due to the placing of the probes affects the measured resistivity but there is no consistent trend according to the number of contact placements. The variation in resistivity measured due to replacing the probe represents 6-7% of the standard deviation of the median value of resistivity. This shows that the change in measured resistivity is due to the probes themselves and not the testing system.

5.3.2 Thermal analysis of bulk Zn_4Sb_3

SThM and temperature dependent Raman spectroscopy techniques have been employed to determine the thermal conductivity of the bulk Zn_4Sb_3. SThM has been performed on the top surface of the Zn_4Sb_3. Figure 5-4 shows the thermal (left) and AFM images (right) of the Zn_4Sb_3 at three different locations. The Zn_4Sb_3 surface was smoothed

using a fin grinder for better contact of the SThM cantilever. The AFM data confirmed that the RMS surface roughness of the sample was ≈ 50 nm.

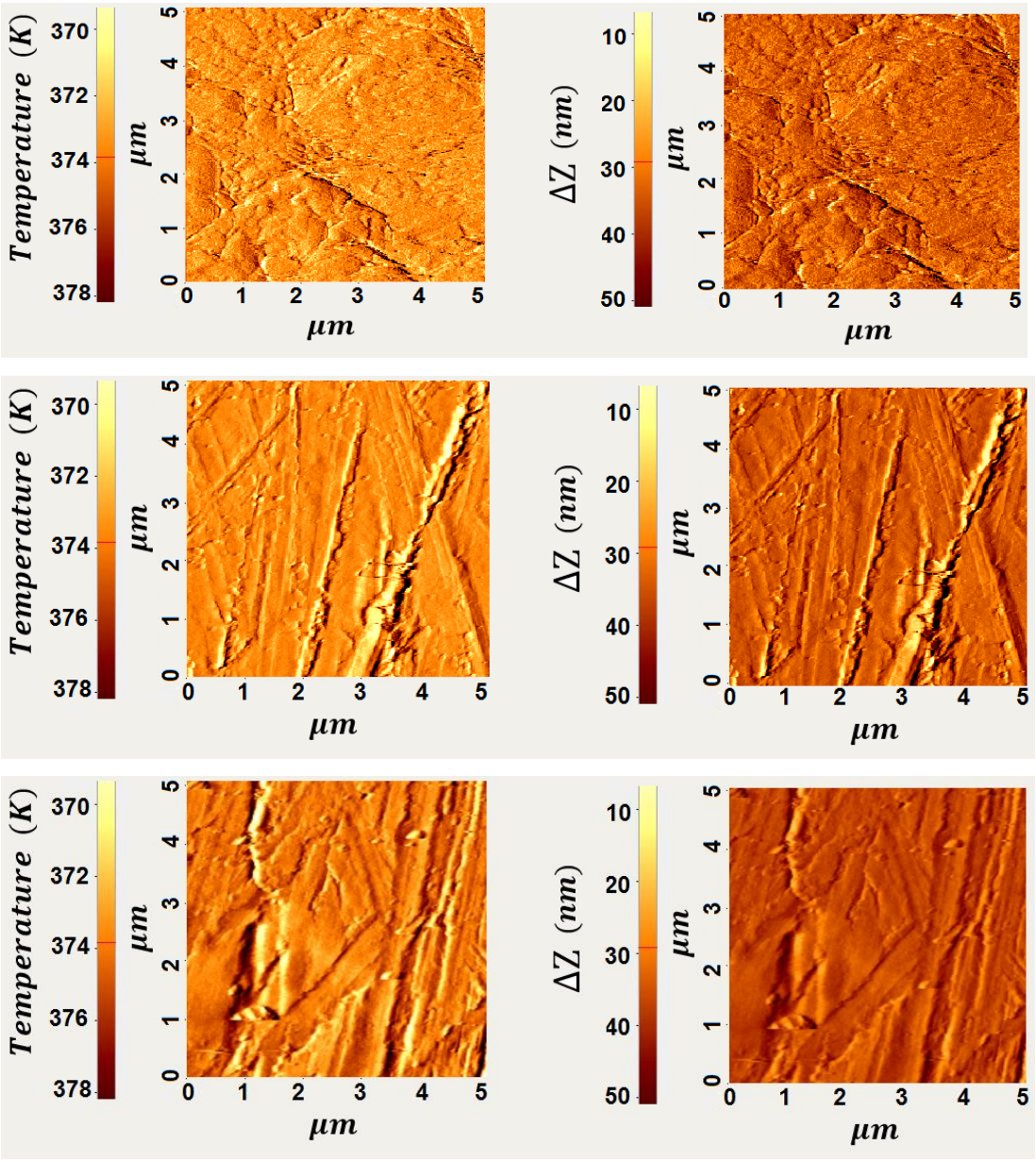

Figure 5. 4: Typical thermal (left) and AFM (right) images of bulk Zn_4Sb_3

The SThM technique described in Chapter 3 was used to extract the thermal conductivity of the sample at different temperatures. The measured thermal conductivity was compared with values derived using Raman spectroscopy measurements using the device described in Chapter 2. The measurement range of the Raman spectrum was 50-4000 cm^{-1}. In the experiment, an Ar^{+}-ion laser with a wavelength of 532 nm was utilised. Furthermore, the power distribution of the laser beam is Gaussian in nature and possesses an area of 1 μm. The sample was heated to temperatures from 300 to 600 K with intervals of 50 K using a heating

stage with precision of 1°C, with the aim of calibrating the correlation between the Raman peak position and sample temperature. The heating phase was maintained for a period of 10 minutes at each temperature in order to ensure that the sample was heated. Subsequently, the Raman spectrum was attained at each temperature. The acquisition time was 12 seconds and the power of the laser was 1.8 mW. Additionally, a low power laser was employed in the calibration to ensure that an additional temperature increase was not induced.

The room temperature Raman peak positions of the Zn_4Sb_3 sample's thermoelectric bulk are shown in Figure 5-5[19] and the peaks at different temperatures are shown in Figure 5-6. The peak at 152 cm^{-1} which is the Zn_4Sb_3 phase is disappeared with temperature increase whereas the intensity of the peak at 117 cm^{-1} is reduced with increasing temperature.[19] The link between the Raman peak position of Zn_4Sb_3 thermoelectric bulk and temperature could then be calibrated, as shown in Figure 5-6. Two peaks are easily observable in the Raman spectrum of the Zn_4Sb_3 as shown in Figure 5-5: one peak at 117 cm^{-1} corresponds to the Sb phase and the peak at 152 cm^{-1} to both Sb and Zn_4Sb_3 phases.[187]

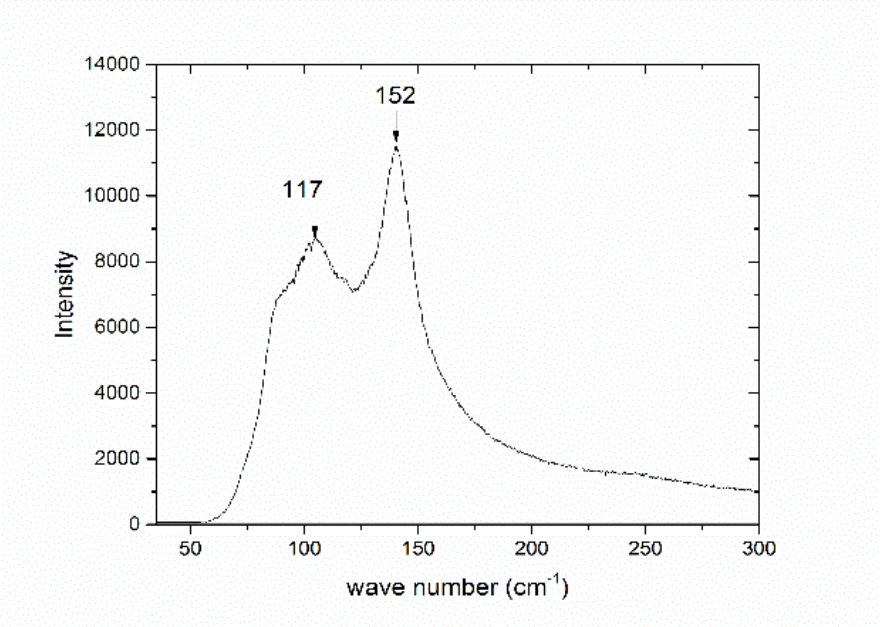

Figure 5. 5: Raman peak positions of the bulk Zn_4Sb_3 phase[19]

Figure 5-7 suggests a near linear correlation between the Raman peak positions and temperature, with a shift downwards at 152 cm^{-1} in the Zn_4Sb_3 thermoelectric bulk, whilst the Raman peak position is observed to decline as the temperature increases.[187] The equation for the trend in Figure 5-7 is $y = -0.154\,x + 523.63$. The error bar in Figure 5-7 corresponds to

the variation in the peaks upon repeating the Raman measurements at three different locations in the sample.

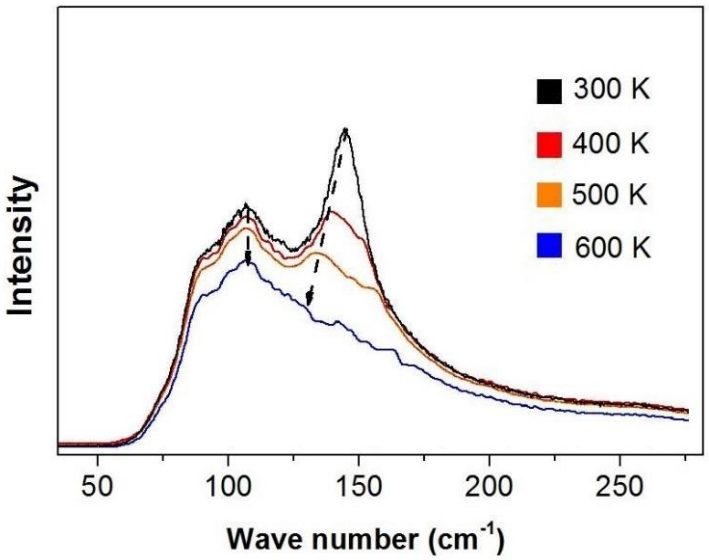

Figure 5. 6: Raman spectra and peak positions of the bulk Zn_4Sb_3 at different temperatures

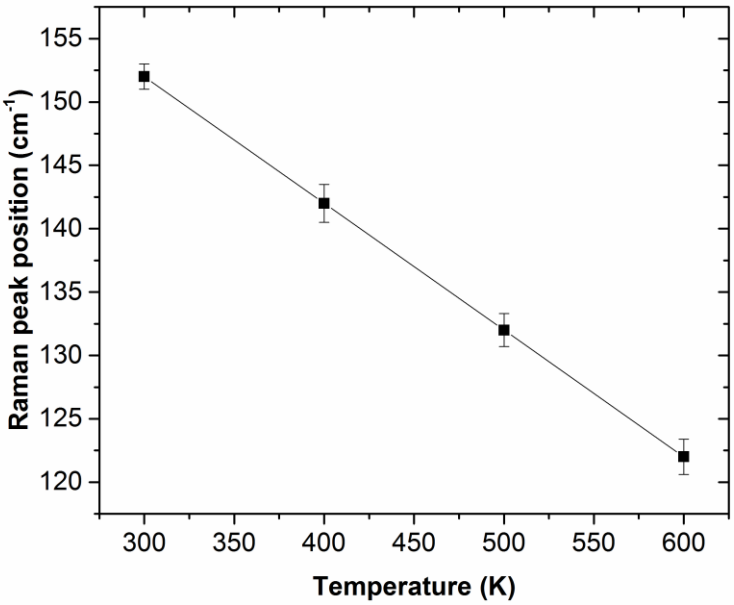

Figure 5. 7: Raman peak position vs the temperature of the bulk Zn_4Sb_3 at low laser power with P=1.8mW

A higher-power laser beam with $P = 9$ mW was concentrated on the Zn_4Sb_3 thermoelectric bulk at room temperature and the equivalent Raman spectrum attained. The ambiguity of the Raman peak position was valued at ±0.25 cm^{-1} as a result of the resolution of the micro-Raman spectroscopy device. The quality of the Raman spectrum could possibly be enhanced by ensuring the acquisition time to be longer than 12 seconds, therefore permitting the Raman peak position to be achieved accurately. By using the value of the Raman peak position produced by high power laser irradiation, the equivalent temperature value was determined (Figure 5-7). This equivalent temperature signified the result of local heating upon the Zn_4Sb_3 thermoelectric bulk brought about by means of laser irradiation with power $P = 9$ mW. The sample thermal conductivity is extracted using Equation 2-16. The corresponding sample temperature at a laser power of $P = 9$ mW has been extracted using the equation of the trend line in Figure 5-7.

The thermal conductivity measurement data using SThM and Raman spectroscopy are shown in Figure 5-8. There is broad agreement in the thermal conductivity between measurement techniques. However, the thermal conductivity measurements using Raman spectroscopy are slightly higher than those measured by the SThM technique. This could be due to additional heat induced by laser power during measurement.

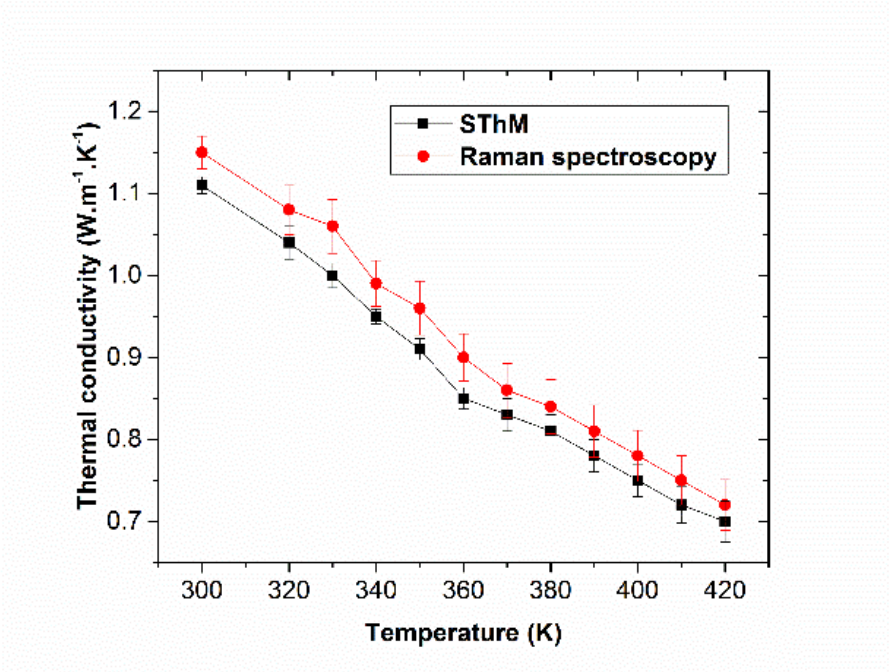

Figure 5. 8: Thermal conductivity measurements of bulk Zn_4Sb_3 using SThM and Raman spectroscopy

The electronic component of thermal conductivity has been calculated by the Wiedemann-Franz Equation 1-13. A value of $0.457\ \mathrm{Wm^{-1}K^{-1}}$ has been extracted at room temperature (300K) and this reduced to $0.348\ \mathrm{Wm^{-1}K^{-1}}$ at 400K. At a higher temperature, the electronic element of the thermal conductivity is dominant over the lattice thermal conductivity. As the size of the SThM thermal tip (< 100 nm) is close to the mean free path of electrons, the contribution of the electrons to heat conduction is insignificant, and therefore, the calculated thermal conductivity is the lattice thermal conductivity. However, in the case of thermal conductivity measurement using Raman spectroscopy, the contribution of electrons is not small. This can be observed in the thermal conductivity measurements revealed in Figure 5-8, so that the thermal conductivity measurement using Raman spectroscopy is total thermal conductivity.

A. Material uniformity

The uniformity of the bulk Zn_4Sb_3 has been investigated in three different locations on the samples. Figure 5-9 demonstrates the standard deviations of the median values of thermal conductivity at three different locations. At room temperature, the standard deviations of the median values of thermal conductivity measurements for the bulk Zn_4Sb_3 sample were within 7-8% using the SThM techniques and 8-10% using temperature Raman spectroscopy. The statistically insignificant variation in thermal conductivity measurements for the sample demonstrates the material's uniformity, which is essential for device-grade material.

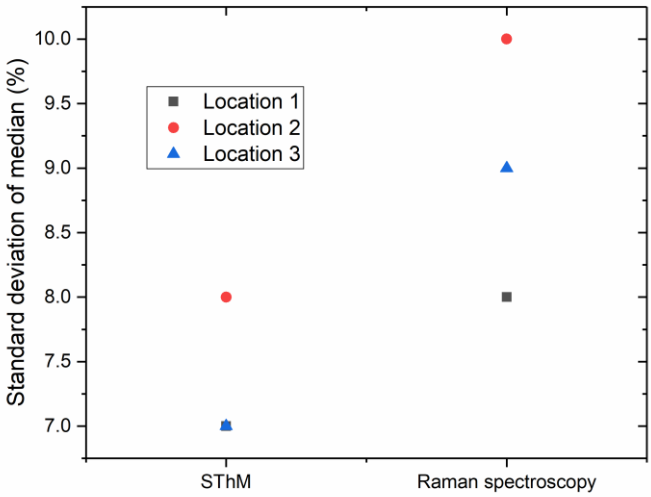

Figure 5. 9: Standard deviations of median values of thermal conductivity measurements for bulk Zn_4Sb_3

B. Effect of surface roughness on thermal characterisation using SThM

To investigate the effect of surface roughness on nanoscale thermal conductivity measurements, SThM was performed on a sample before and after being polished with a fin grinder. The RMS surface roughness of the unpolished sample was ≈ 1 µm whereas the values of surface roughness decreased to ≈ 50 nm in the polished Zn_4Sb_3 sample. The thermal conductivity measurement for the unpolished sample was also lower than that of the polished sample. At room temperature, the thermal conductivity of the unpolished sample was 0.98 $Wm^{-1}K^{-1}$ whereas for the polished sample it was 1.1 $Wm^{-1}K^{-1}$. Since the SThM probe apex is sized at nanoscale, therefore the thermal characterisation is also at nanoscale. At submicron scale, phonon scattering due to the rough surface dominates all of other bulk scattering agents such as point defects, dislocations, and grain boundaries. This scattering due to surface roughness could cause the reduction in thermal conductivity in the unpolished sample.[188]

5.3.3 Seebeck coefficient of bulk Zn_4Sb_3

The SThM technique was utilised to measure the Seebeck coefficient of bulk Zn_4Sb_3. The method is explained in Section 3.5. The sample dimensions are $6\ mm \times 6\ mm \times 2\ mm$ in length, width and depth respectively. The sample was polished to ensure good contact with the heating stage and thermal probe. In order to minimise the effect of any sort of contamination on the thermal probe contact, the Zn_4Sb_3 was cleaned with acetone and methanol prior to establishing probe contact. The sample was mounted directly on to the heating stage and, to make sure the sample was in thermal equilibrium with the heating stage, the samples were placed on the heating stage 8 min prior to the SThM measurements. All the measurements taken on the sample were performed under the same experimental condition.

The induced temperature and voltage of the Zn_4Sb_3 thermoelectric sample measured at different temperatures and values of ΔT and ΔV_s were calculated and the sample's seebeck coefficient was extracted. Figure 5-10 shows the thermoelectric measurement of the Zn_4Sb_3 thermoelectric sample. The seebeck coefficient temperature dependence increases as the temperature increases above room temperature. Additionally, repeated measurements at different locations on the same sample led to a variation of $< 0.5\%$ in seebeck coefficient measurements. A seebeck coefficient value of $102\ \mu VK^{-1}$ was estimated at room temperature. The Seebeck measurements are in good agreement with those reported elsewhere for this material. At room temperature, a value of Seebeck coefficient $90\ \mu VK^{-1}$ for bulk Zn_4Sb_3 has been reported.[184] This particular value is similar to the measured value of seebeck coefficient applying Seebeck microprobe scanning.[184] The Zn_4Sb_3 thermoelectric sample given a value of $173\ \mu VK^{-1}$at 420 K which shows an increase of $71\mu VK^{-1}$.

The value of the Seebeck coefficient shows an increase with temperature. The Seebeck coefficient strongly depends on the Fermi level, which in turn depends on the carrier concentration, carrier effective mass, and temperature as shown in Equation 1-8. For bulk Zn_4Sb_3 material with constant carrier concentration, electrical conductivity diminishes with a rising temperature (Figure 5-2). The electrical conductivity is thus inversely proportional to the Seebeck coefficient. Therefore, the Seebeck coefficient increases by 69% as temperature increases from 300K to 420K, as Figure 5-10 illustrates.

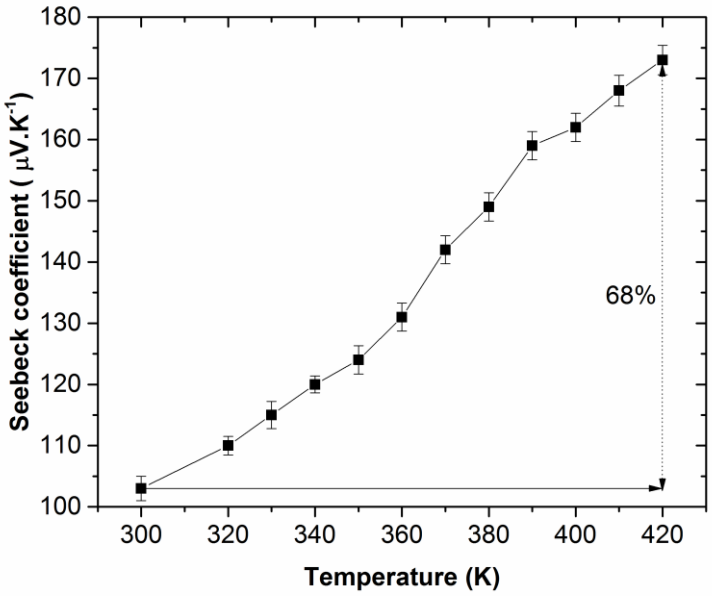

Figure 5. 10: Seebeck measurement of the Zn_4Sb_3 at various temperatures

5.3.4 Thermoelectric power factor

The Seebeck coefficient was used to extract the thermoelectric power factor ($S^2\sigma$) which is a combination of the Seebeck coefficient and electrical conductivity. It should be noted that the value of the power factor at room temperature is 6.5×10^{-4} $\mathrm{WmK^{-2}}$ and thus, increased to 1.12×10^{-3} $\mathrm{WmK^{-2}}$ at 420K. The power factor shows an increase with temperature, as Figure 5.11 illustrates.

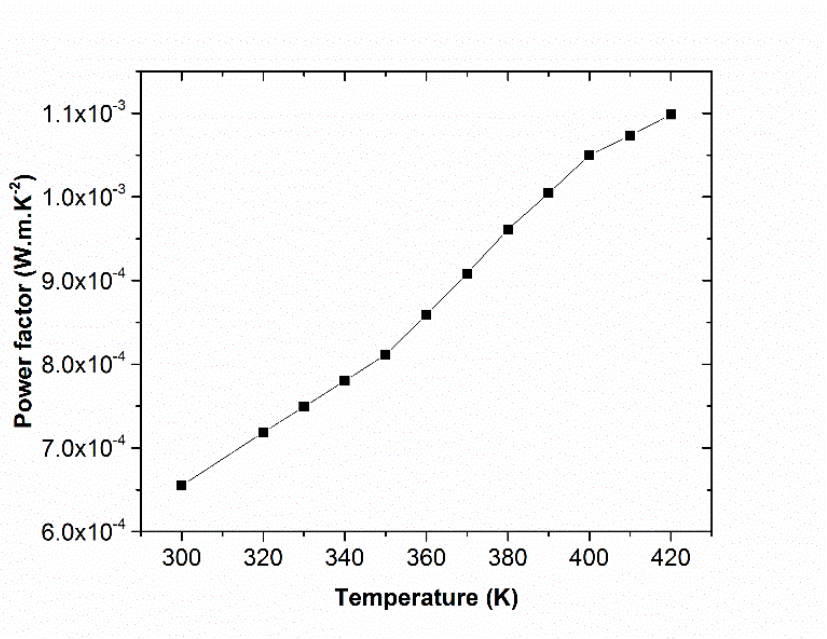

Figure 5. 11: Thermoelectric power factor of bulk Zn_4Sb_3

5.3.5 Thermoelectric figure of merit (ZT)

The measurements of the thermoelectric parameters have been used to extract the value ZT using the equation $ZT = S^2\sigma\, T/k$. Figure 5-12 shows an increase in ZT with temperature. The measured values are noted to be in good agreement with values reported for this material[183-184] including a value of ZT=0.17 reported for bulk Zn_4Sb_3 at room temperature.[184] The bulk Zn_4Sb_3 exhibits a ZT=0.16 at room temperature this increases up to 0.65 at 420 K.

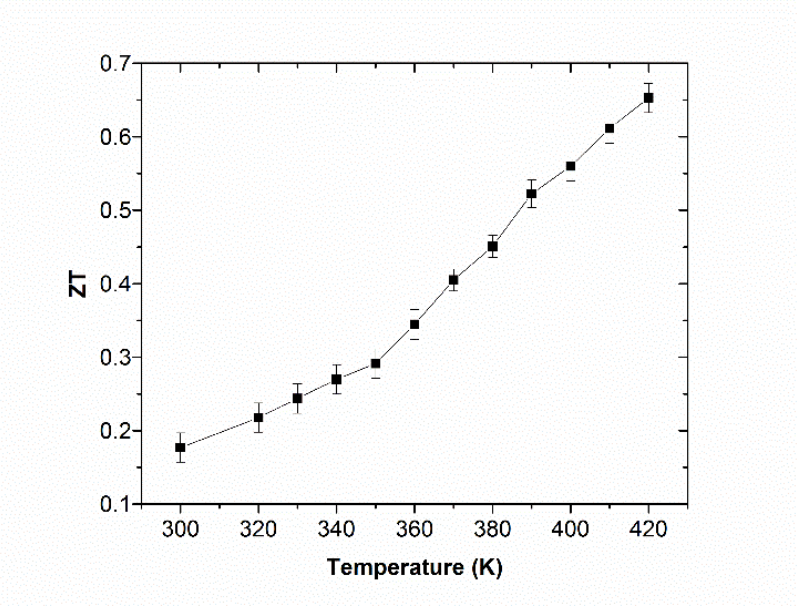

Figure 5. 12: ZT values of bulk Zn_4Sb_3 against temperature

5.4 Nanostructuring of Undoped Zn_4Sb_3 by Ball-Milling

The Zn_4Sb_3 bulk was crushed into powder and ball-milled with a BioSpec 3110BX machine made by Mini-BeadBeater. A ball mill is a device that breaks materials into smaller pieces by crushing. It works on the principle of impact and attrition. The Zn_4Sb_3 powder was mixed with Zirconium dioxide (ZrO_2) with a diameter of $0.02\ mm$ in a container and shaker for approximately 1 min. Ball-mill shaking causes an increase in container temperature. Therefore, the container was filled with N_2 which prevents the nanoparticles from sticking to each other. The container was then centrifuged (6000rpm, 3000 g force) for 5 min in order to separate the Zn_4Sb_3 nanoparticles and ZrO_2. Then the separated nanoparticles were left at room temperature for some time to dry.

The size distribution profile of the Zn_4Sb_3 particles in the ball-milled powders was measured using dynamic light scattering (DLS) approaches made by Malvern Zetasizer, by suspending the powder particles in ethanol. Ethanol is a versatile solvent, which is miscible water with many organic solvents. It can be evaporated under lab atmospheric conditions and at room temperature. The structures of the milled powders were characterised utilising XRD and TEM. Simple mean particle sizes were determined by measuring the full width at half maximum (FWHM) of the diffraction peaks in XRD using OriginPro data analysis software.

Figure 5-13 shows the average size distribution profile obtained frequently from up to 6 h of powder ball milling.

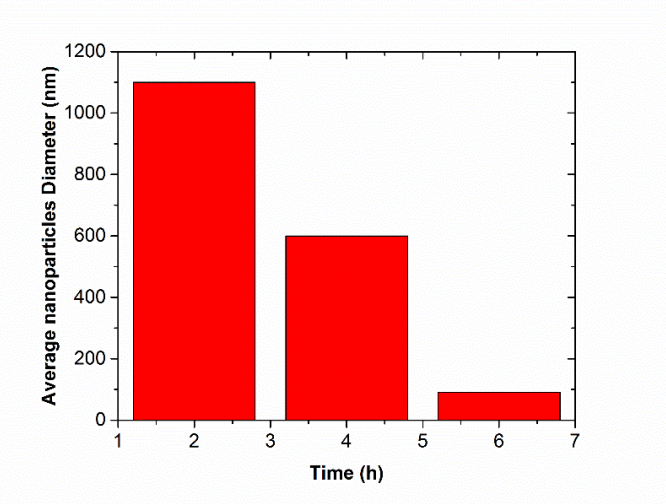

Figure 5. 13: Average size distribution profile of the Zn_4Sb_3 nanoparticles obtained by DLS

TEM has been performed on the Zn_4Sb_3 nanoparticles in order to measure the particle sizes. Figure 5-14 shows TEM images obtained for the Zn_4Sb_3.

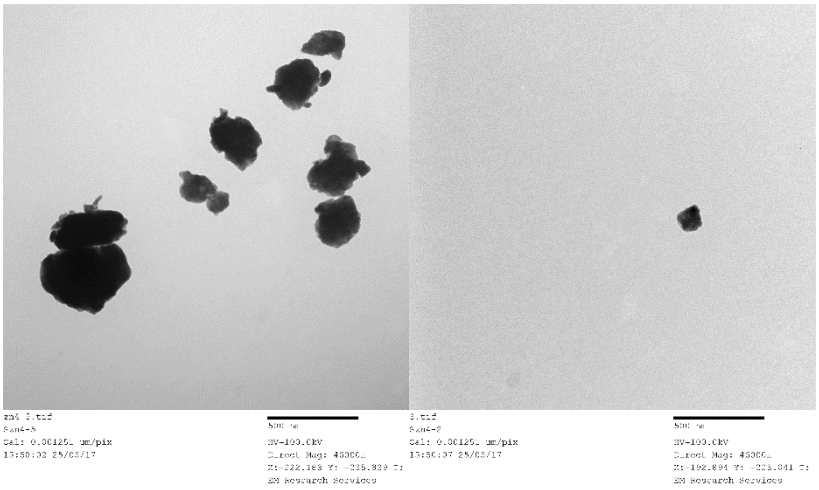

Figure 5. 14: TEM images of the Zn_4Sb_3 nanoparticles

The average size of nanoparticles after 10 measurements obtained using TEM is in the order of 110 nm. The TEM was performed after 6 hours. The size distribution of Zn_4Sb_3 nanoparticles are presented in Figure 5-15. The DLS values are lower than the values measured by XRD and TEM by 20 nm. The mixtures size distribution and presence of dispersants induced error to DLS sizing measurement. Measuring the particle size with DLS in different aqueous media might improves the size measurement error of the nanoparticles.

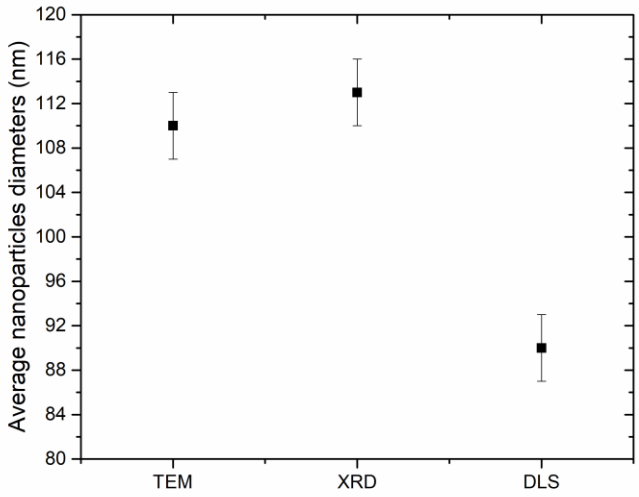

Figure 5. 15: Average nanoparticle diameter measured using TEM and XRD

XRD diffraction has also been performed on the Zn_4Sb_3 in order to confirm the purity of the nanoparticles. The size of Zn_4Sb_3 nanoparticles was also determined using peak FWHM. The XRD has been performed before and after ball-milling. Figure 5-16a shows the main phase of the Zn_4Sb_3 powder. The main phase has been compared with the Zn_4Sb_3 spectrum in the datasheet to confirm the peak position in Figure 5.16b. The XRD analysis of the powders identified the main phase of the Zn_4Sb_3 and confirm the purity of the material (Figure 5.15).

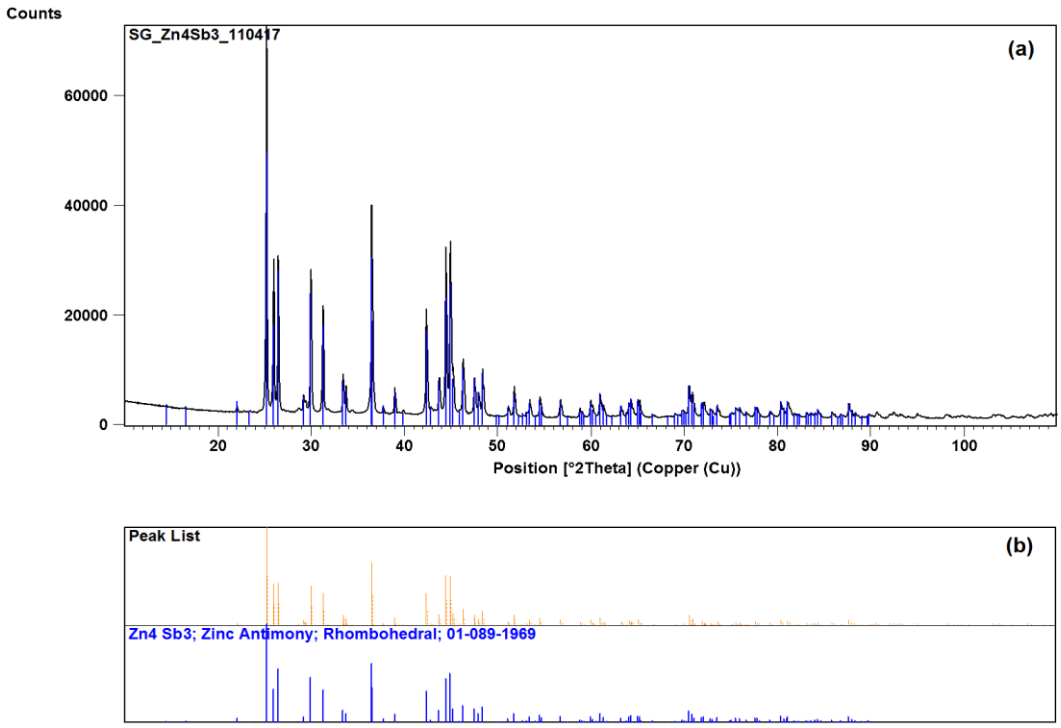

Figure 5. 16: (a) X-ray diffraction pattern of the Zn_4Sb_3 nanoparticles (b) Zn_4Sb_3 nanoparticles peak list

Scherrer's equation ($\tau = K\lambda/\beta cos\theta$) was used to determine the size of Zn_4Sb_3 nanoparticles in the form of powder. In Scherrer's equation, τ is the mean size of the particles, K is a dimensionless shape factor that has a representative value of in the region of 0.9, λ is the X-ray wavelength at 0.15406 nm, β is the line broadening at half the maximum intensity (FWHM), whilst θ is the Bragg angle. The peak position and FWHM has been determined from XRD data using the OriginPro data analysis. The extracted data has been put in Scherrer's equation for the calculation of crystallites size. Table 5-1 shows the results from XRD peak FWHM examination before and after ball-milling.

Before-milling (nm)	After-milling (nm)
900	113

Table 5.1. XRD FWHM average size of the Zn_4Sb_3

5.5 Zn_4Sb_3 nanoparticles Embedded in silica aerogel

The thermoelectric characterisation of silica aerogel was discussed in detail in Chapter 4. Aerogel was prepared as described in sections 2.4-2.5. The same approach was used to synthesise the nickel nanoparticles implanted in silica aerogel, as Chapter 4 describes. Then it is used to synthesise the Zn_4Sb_3 nanoparticles embedded in silica aerogel.

Silica gels were made by way of the hydrolysis of the precursor tetraethoxysilane (TEOS) (98%), ethanol (≥ 99.8%) and de-ionised water with a 2:38:33 molar ratio of TEOS:ethanol:water. Furthermore, 2 ml of Zn_4Sb_3 nanoparticle suspension and 33 ml precursor were utilised with 1 ml of catalyst, which is a mixture of ammonium hydroxide (28-30%), ammonium fluoride (≥ 98%) and de-ionised water with a 1:8:111 molar ratio of NH4F:NH4OH:H2O, which is employed to speed up the gelation process. These compounds were utilised without any additional purification. Zn_4Sb_3 nanoparticles were spread in deionised water by way of ultrasonication made by Sonopuls Bandelin in order to attain Zn_4Sb_3 nanoparticle suspensions. Ultrasonication process helps to disperse the nanoparticles in the solution.[181]

The Zn_4Sb_3 nanoparticle gel was removed and placed in 500 ml of ethanol to be cleansed and aged for 24 hours. The cleansing/ageing solvent was subsequently replaced by 250 ml of ethanol. After 24 hours, the solvent was swapped with 250 ml of hexane. This procedure was performed three times. Next, the gel was dried out at an ambient temperature for a period of 48 hours.

5.6 Thermoelectric properties of Zn_4Sb_3 nanoparticles embedded in silica aerogel

The thermoelectric characterisation of the Zn_4Sb_3 nanoparticles embedded in silica aerogel sample has been carried out using various techniques.[189-191] The electrical properties of the sample were measured using four-probe measurements via Hall effect equipment and CASCADE 4200. These techniques are described in Chapter 3. The thermal properties were investigated using SThM and a HotDisk analyser. The sample was cut into a rectangular shape with dimensions of $1\text{cm} \times 1\text{cm} \times 0.5\text{cm}$.

5.6.1 Electrical resistivity measurement

The measurement of electrical resistivity has been performed on the Zn_4Sb_3 embedded in silica aerogel sample at different temperatures. Four conductive contacts were coated using a nickel screening compound from Electrolube (THE SOLUTIONS PEOPLE) with a surface resistivity of 0.1 Ω/□ on the four corners of the sample.

The results for electrical resistivity at different temperatures using both techniques are shown in Figure 5-17. At room temperature electrical resistivities of 1.2×10^{10} Ω m and 2.6×10^{10} Ω m were measured using the four-point probe and Hall effect methods respectively.

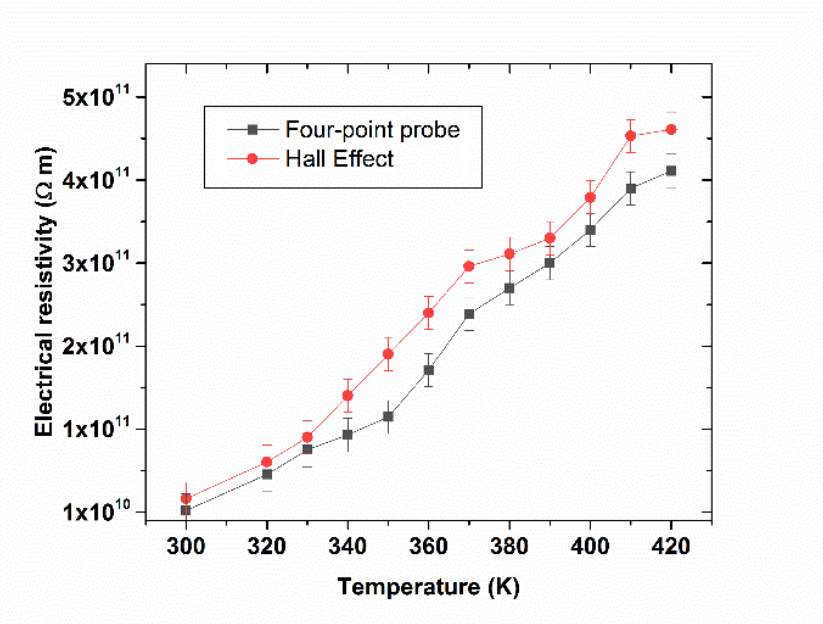

Figure 5. 17: Electrical resistivity measurements of the Zn_4Sb_3 embedded in silica aerogel sample at different temperatures

The sample's electrical resistivity improved with rising temperature. The electrical resistivity of the Zn_4Sb_3 nanoparticles embedded in silica aerogel increased by 16 orders of magnitude compared with Zn_4Sb_3 bulk. The electrical resistivity of pure silica aerogel has been reduced by 3 orders of magnitudes when the silica aerogel was embedded with thermoelectric Zn_4Sb_3 nanoparticles. Figure 5-20 shows the electrical resistivity of pure silica aerogel, bulk Zn_4Sb_3 and Zn_4Sb_3 nanoparticles embedded in silica aerogel at 300 K and 420 K. The increase in electrical resistivity will weaken the power factor and consequently decease the ZT value of the Zn_4Sb_3 nanoparticles embedded in silica aerogel.

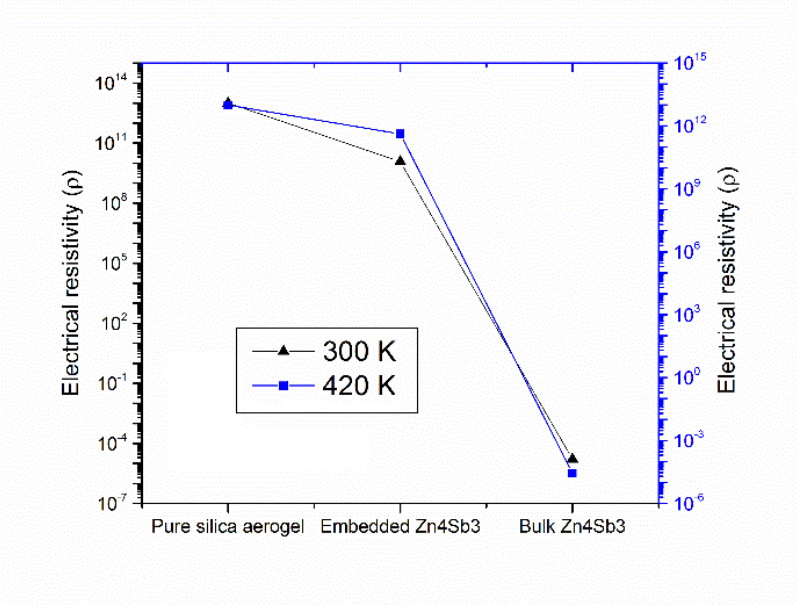

Figure 5. 18: Electrical resistivity of pure silica aerogel, bulk Zn_4Sb_3 and Zn_4Sb_3 nanoparticles embedded in silica aerogel at 300 K and 420 K

To investigate the material's uniformity, resistivity was measured in three different locations on the samples. Figure 5-19 shows the standard deviations of the median values of electrical resistivity for bulk Zn_4Sb_3 nanoparticles embedded in silica aerogel material. At room temperature, the standard deviations of the median values of nine resistivity measurements for the Zn_4Sb_3 nanoparticles embedded in silica aerogel bulk sample were within 6-8% using the four-point probe techniques and 9-11% using Hall effect equipment. The statistically insignificant variations in electrical measurements for the samples demonstrate the material's uniformity, which is essential for device-grade material.

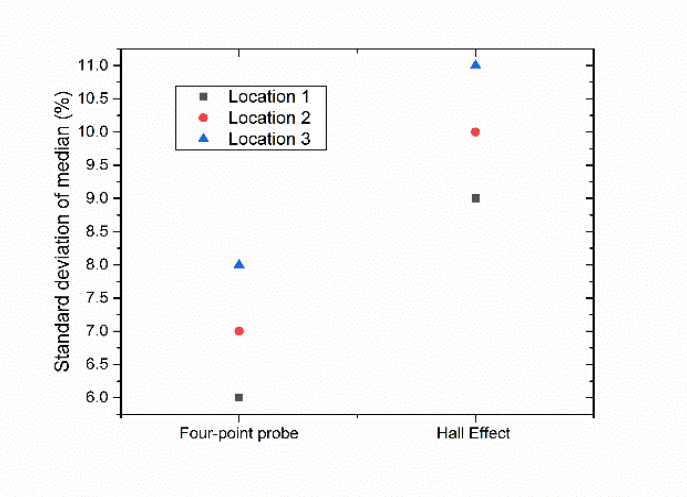

Figure 5. 19: Standard deviations of median values at three different location

5.6.2 Thermal analysis of the Zn_4Sb_3 nanoparticles embedded in silica aerogel

The thermal conductivity of the Zn_4Sb_3 inserted in silica aerogel was determined using SThM. The measured values of thermal conductivity were compared with the values given by the HotDisk analyser.

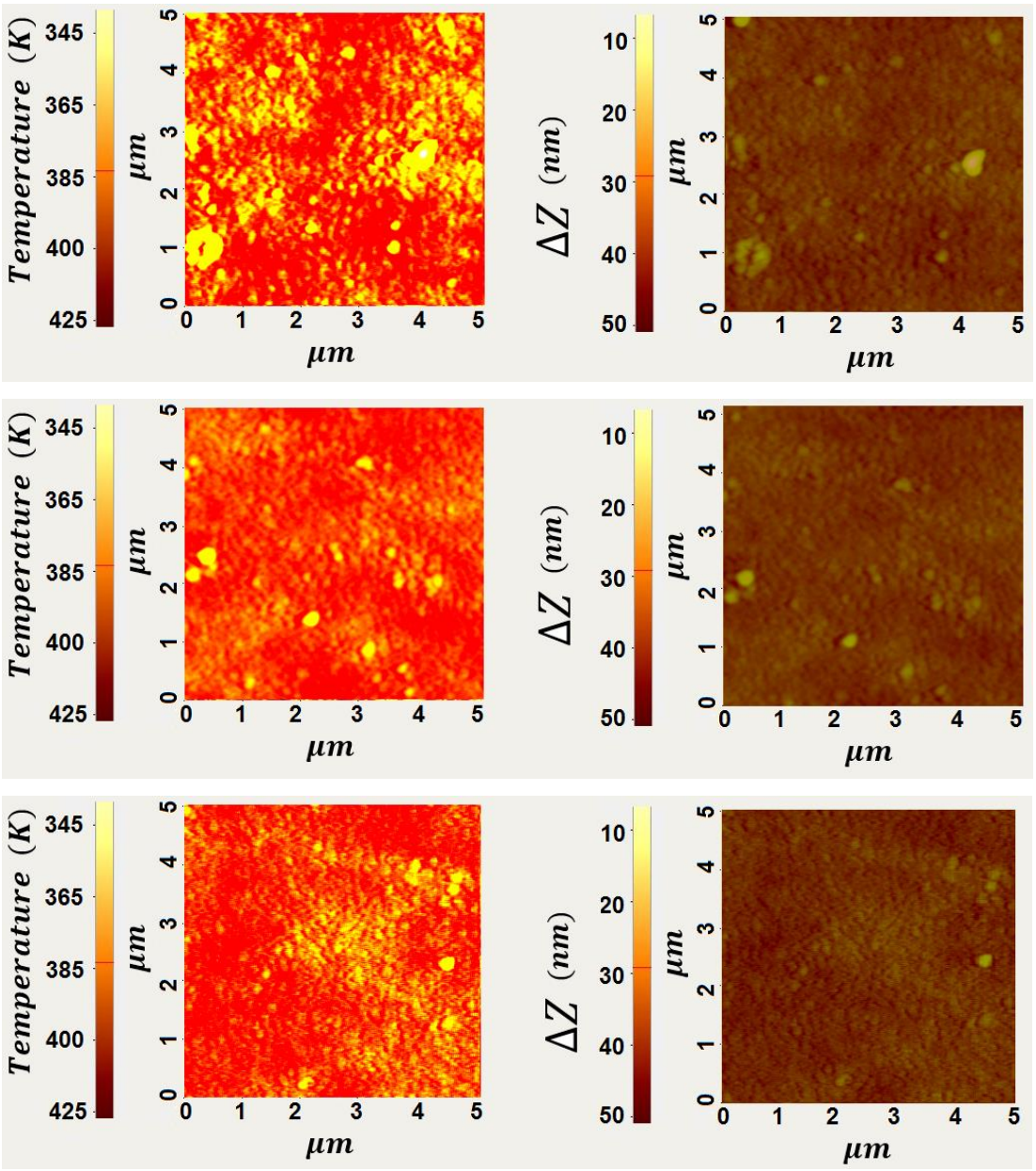

Figure 5. 20: The topographical image (right) and temperature (left) of the Zn_4Sb_3 embedded in silica aerogel sample

In Figure 5-20 the topographical images (right) and temperature scans (left) of the Zn_4Sb_3 embedded in silica aerogel sample at three different locations on the sample is shown. The yellow spots on the thermal image are Zn_4Sb_3 nanoparticle clusters.

Figure 5-21 shows the thermal conductivity measurements using both techniques.

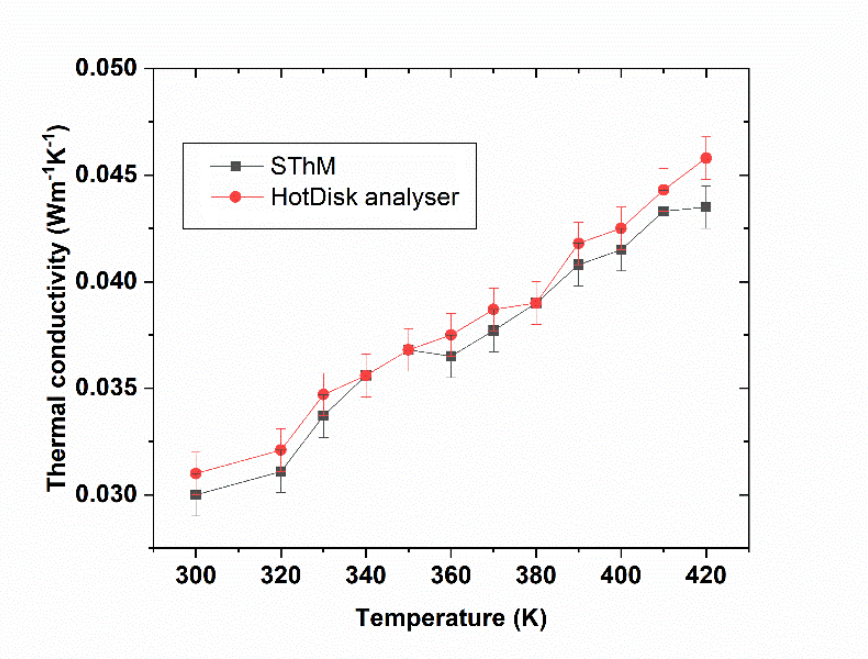

Figure 5. 21: Thermal conductivity measurements of the Zn_4Sb_3 inserted in the silica aerogel sample at various temperatures

The thermal conductivity of the Zn_4Sb_3 embedded in the silica aerogel sample is reduced significantly compared with that of the bulk Zn_4Sb_3 as shown in Figure 5-22. A thermal conductivity value of 1.1 $Wm^{-1}K^{-1}$ was measured using SThM for the Zn_4Sb_3 bulk at room temperature, whereas the thermal conductivity of Zn_4Sb_3 embedded in silica aerogel was 0.030 $Wm^{-1}K^{-1}$ at room temperature. The thermal conductivity measurements of the Zn_4Sb_3 embedded in silica aerogel are very similar to the measurements for silica aerogel. From the thermal conductivity measurements, it is clear that the Zn_4Sb_3 embedded in silica aerogel behaves as a thermal insulator.

The thermal conductivity of embedded Zn_4Sb_3 increased with temperature compared with bulk Zn_4Sb_3. As the temperature increased from 300 to 420 K in the silica samples, the phonon mean free path increased and the lattice vibrations dominated the thermal conductivity. Consequently, the thermal conductivity increased. Figure 5-22 reveals that the thermal conductivity of embedded Zn_4Sb_3 increased compared with that of pure silica aerogel.

Figure 5-22 shows that the impact of the Zn_4Sb_3 nanoparticles to thermal conductivity is exceedingly slight.

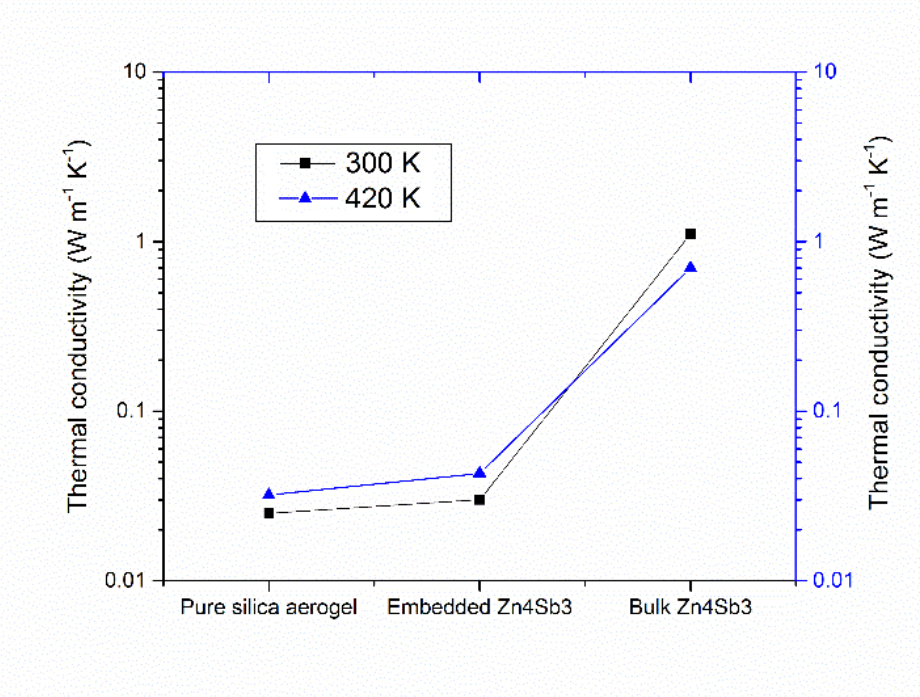

Figure 5. 22: Thermal conductivity of pure silica, Zn_4Sb_3 embedded in silica aerogel, and bulk Zn_4Sb_3 at 300 and 420 K

The use of SThM enables the thermal conductivity of Zn_4Sb_3 nanoparticle clusters and the silica aerogel to be measured separately. The silica aerogel and Zn_4Sb_3 nanoparticle clusters are distinct in the SThM thermal images that are revealed in Figure 5-22, seeing as the thermal conductivity values of the Zn_4Sb_3 and silica aerogel are different.

In order to illustrate the reduction in thermal conductivity in the material, the thermal conductivity of bulk Zn_4Sb_3 and Zn_4Sb_3 nanoparticles has been compared. At room temperature (T = 300 K), the values of thermal conductivity of bulk Zn_4Sb_3 have been measured of 1.15 $Wm^{-1}K^{-1}$. A mean thermal conductivity of 0.73 $W.m^{-1}.K^{-1}$ was extracted for the Zn_4Sb_3 nanoparticles cluster. These measured value of thermal conductivity are in good agreement with thermal conductivity calculated using nonequilibrium molecular dynamics (NEMD), which is given a value of 0.45 $Wm^{-1}K^{-1}$ at 40% porosity.[177,24] The results show that the thermal conductivity of Zn_4Sb_3 decreased with the reduced size of the Zn_4Sb_3 material to nanoscale due to the reduction in the average free path of the phonon.

5.6.3 Thermoelectric Seebeck coefficient measurement

SThM has been applied to measure the Seebeck coefficient of the Zn_4Sb_3 embedded in silica aerogel sample. The method has described in Section 3.5. A median value of $1820\mu\ VK^{-1}$ of the Seebeck coefficient of the Zn_4Sb_3 embedded in silica aerogel sample was measured at room temperature and there is a small decrease in the Seebeck coefficient at 420K (Figure 5-23) where the median value of the Seebeck coefficient at 420K is $1820\mu\ VK^{-1}$.

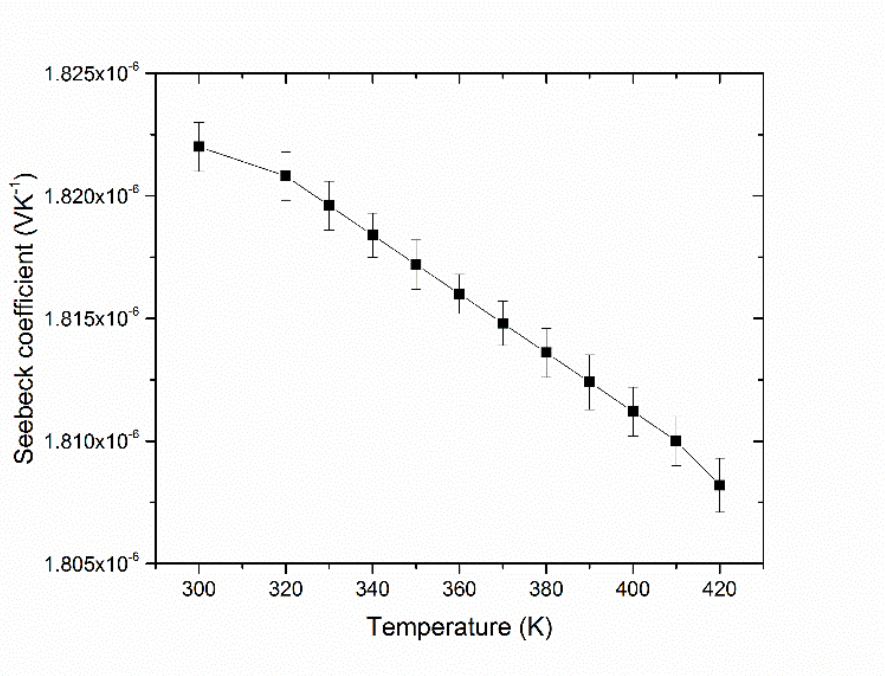

Figure 5. 23: Seebeck coefficient of the Zn_4Sb_3 embedded in silica aerogel sample

The measured values of the Seebeck coefficient are similar to the values of Seebeck measurement for the silica aerogel sample as Figure 5-24 shows. The Seebeck coefficient of the Zn_4Sb_3 embedded in silica aerogel sample has been increased by 18 orders of magnitude compared with the Zn_4Sb_3 bulk.

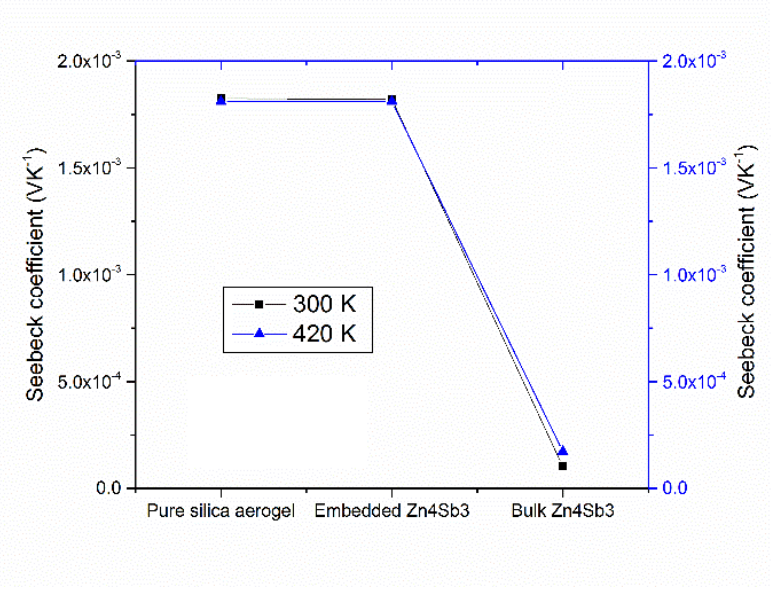

Figure 5. 24: Seebeck coefficient measurements of pure silica, embedded Zn_4Sb_3, and bulk Zn_4Sb_3 at 300 and 420 K

5.6.4 Thermoelectric power factor

The value of the Seebeck coefficient combined with electrical resistivity have been used to calculate the thermoelectric power factor. Figure 5-25 shows the thermoelectric power factor of Zn_4Sb_3 nanoparticles embedded in silica aerogel at various temperatures. The Zn_4Sb_3 embedded in silica aerogel exhibits a Seebeck coefficient of $1820\mu\ VK^{-1}$ which could increase the power factor. However, since the electrical resistivity of Zn_4Sb_3 nanoparticles embedded in silica aerogel increased significantly (Figure 5-25) the power factor is low compared with that of bulk Zn_4Sb_3.

The power factor of Zn_4Sb_3 embedded in silica aerogel was then compared with the power factor of NiNPs embedded in silica aerogel as described in Section 4.3. At room temperature the power factor for embedded NiNP is in the range of $10^{-12}\ Wm^{-1}\ K^{-2}$ whereas it is in the range of $10^{-16}\ Wm^{-1}\ K^{-2}$ for Zn_4Sb_3 nanoparticles embedded in silica aerogel. This difference could be due to concentration of Zn_4Sb_3 compared with NiNP in silica aerogel. The Zn_4Sb_3 nanoparticles at 700 ppm start to collect at the bottom during synthesis so that it is difficult to make a sample with a concentration of 700 ppm.

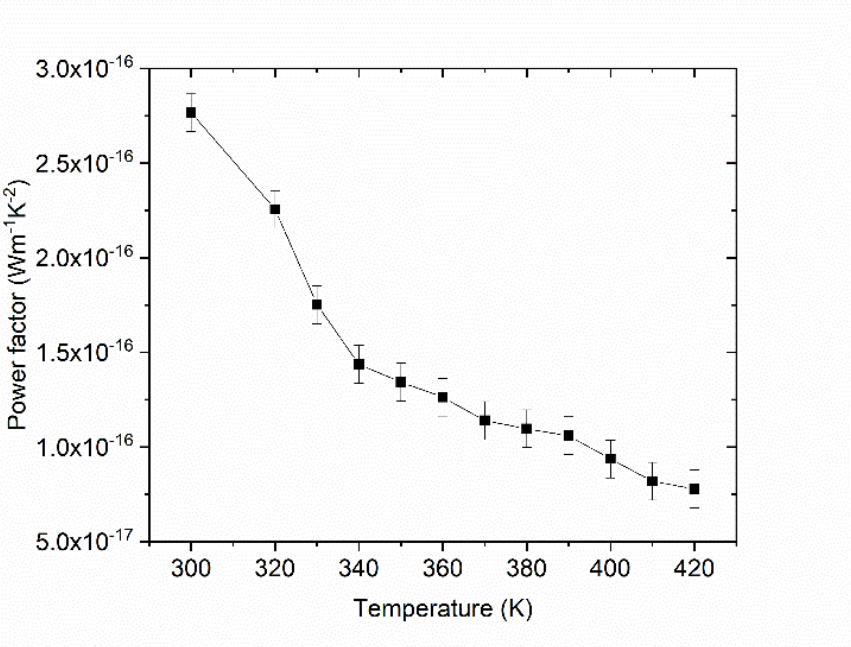

Figure 5. 25: Power factor of Zn_4Sb_3 embedded in silica aerogel at different temperatures

5.6.5 Thermoelectric figure of merit (ZT)

All measured thermoelectric parameters have been used to extract values of ZT using the equation $ZT = S^2\,T/\rho k$. Figure 5-26 shows the value of ZT concerning Zn_4Sb_3 inserted in silica aerogel.

ZT decreases significantly compared with that of bulk Zn_4Sb_3. The thermal conductivity and Seebeck coefficient is higher in comparison with the bulk Zn_4Sb_3; however, the value of ZT is also affected by electrical resistivity. This reduction in ZT mainly comes from the changes in electrical resistivity.

The electrical resistivity has been significantly increased in the Zn_4Sb_3 embedded in silica aerogel sample compared with bulk Zn_4Sb_3 by 16 orders of magnitude.

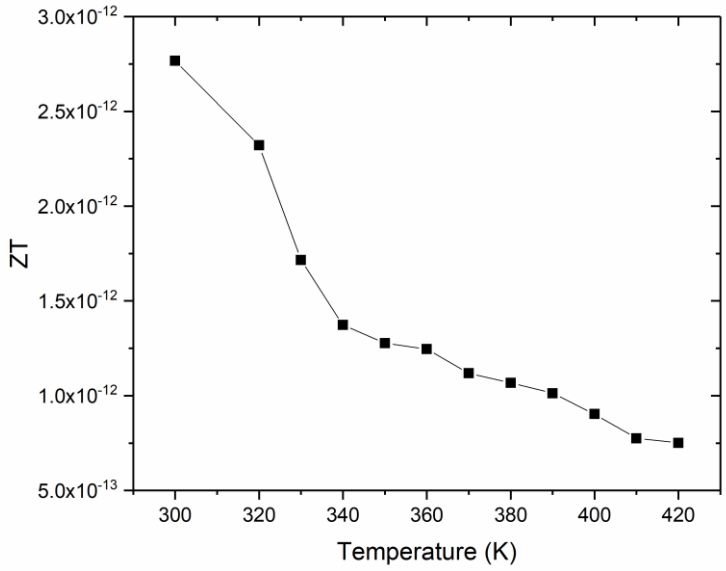

Figure 5. 26: ZT values of Zn_4Sb_3 embedded in silica aerogel sample

The room temperature ZT values reached 10^{-9} for NiNP embedded in silica aerogel at 700ppm, whereas the corresponding values are in the range of 10^{-12} for Zn_4Sb_3 embedded in silica aerogel. The value of ZT in embedded Zn_4Sb_3 is higher by 3 orders of magnitude compared with embedded NiNP in silica aerogel. Meanwhile, the thermal conductivity is noted to be in the same range of $0.02 - 0.03$ W m^{-1} K^{-1} for both Zn_4Sb_3 and NiNP embedded in silica aerogel.

The value of electrical resistivity are in the range of 10^7 Ωm and 10^{10} Ωm respectively for NiNP and Zn_4Sb_3 embedded in silica aerogel. There is a difference of 3 orders of magnitude in the electrical resistivity of NiNP and Zn_4Sb_3 embedded in silica aerogel. The main difference in the value of ZT comes from the differences in electrical resistivity that consequently reduce the power factor and ZT.

5.7 Conclusion

The Zn_4Sb_3 embedded in the silica aerogel sample has been synthesised successfully and its thermoelectric properties have been compared with those of the Zn_4Sb_3 material. The Zn_4Sb_3 nanoparticles synthesised using the ball-milling process and an average diameter of 110nm of nanoparticles has been obtained. The Zn_4Sb_3 nanoparticles were embedded in silica

aerogel and a sample with a concentration of 700ppm has been prepared. Further increases in concentration of the Zn_4Sb_3 nanoparticles are not possible because the Zn_4Sb_3 nanoparticles collect at the bottom during synthesis and no further increases were shown in the Zn_4Sb_3 nanoparticle concentration in the final aerogel product.

The thermoelectric characterisation of Zn_4Sb_3 nanoparticles embedded in silica aerogel has been demonstrated successfully.

Chapter 6

6.1 Conclusion

This thesis was dedicated to the synthesis and characterisation of thermoelectric material using different techniques. Based on state-of-the-art thermoelectric material in Chapter 1, engineering material properties can alter the electrical and thermal conductivity. Silica aerogel is of interest owing to its minimal thermal and electrical conductivity. This has led to the synthesis of silica aerogel embedded with Ni nanoparticles and Zn_4Sb_3 thermoelectric material. Silica aerogel doped with Ni nanoparticles and Zn_4Sb_3 nanoparticles was synthesised using sol-gel process.

The methodology of the experimental work was introduced to study the thermoelectric properties of the samples and explained in Chapter 2. The Seebeck coefficient, thermal conductivity and electrical resistivity perimeters signify the performance and quality of the material. Therefore, precise and accurate measurement is essential. Scanning thermal microscopy (SThM) and temperature dependent Raman spectroscopy was used to evaluate the thermal properties of the synthesised samples. Electrical resistivity was measured using the four-point probe on CASK4200. Measured parameters were used to extract the sample ZT. The composition of the samples was studied using X-ray diffraction and transmission electron microscopy.

We raised a question regarding thermal conductivity measurement using SThM and to achieve more accurate thermal characterisation of materials. In Chapter 3, an approach to improve the thermal conductivity measurement using SThM was introduced. The SThM probe apex temperature (T_{apex}) is always estimated and considered as a constant value in order to extract values of G_p and then G_c. This increases the uncertainty regarding thermal conductivity measurement. In this work, a KNT thermal probe mounted on a SThM in conjunction with an ultra-fine thermocouple was used to experimentally measure G_p and then G_c. This led to a 5% improvement in thermal conductivity measurements compared with existing thermal conductivity measurements using SThM. Similarly, in this approach the sample Seebeck coefficient can be measured simultaneously with thermal conductivity. Compared with the existing method, this approach does not need any test structure and consists of direct measurement.

Nanostructuring has been noted to be a valuable method in regard to diminishing thermal conductivity, while maintaining the electrical properties of thermoelectric materials. In Chapter 4, the thermoelectricity of Ni nanoparticles embedded in silica aerogel at different concentrations was examined. As demonstrated, Ni nanoparticles samples exhibit a magnitude improvement of 6 orders when the concentrations are increased from 0 to 700 ppm. The electrical resistivity is highly sensitive to the concentration of Ni nanoparticles in the silica aerogels, while the thermal conductivity remains largely unchanged.

In Chapter 5, the Zn_4Sb_3 embedded in the silica aerogel sample has been synthesised successfully and its thermoelectric properties have been compared with those of the Zn_4Sb_3 material. The concentration of the Zn_4Sb_3 nanoparticles has increased to 700 ppm. The electrical resistivity of the Zn_4Sb_3 embedded in the silica aerogel has increased compared with bulk Zn_4Sb_3. The increase in electrical resistivity will weaken the power factor and consequently decease the ZT value.

6.2 Future works

In this work, the thermoelectric properties of silica aerogel-based material have been studied in order to maximise the efficiency of bulk Zn_4Sb_3 aiming for improved efficiencies of future thermoelectric modules at room temperature. The work achieved within this thesis is reported next:

- The complete thermoelectric characterisation including electrical resistivity, thermal conductivity and Seebeck coefficient of nickel nanoparticles embedded in silica aerogel at three different concentrations.
- The development and improvement of the characterisation technique to measure experimentally the thermal conductivity using scanning thermal microscopy, so that the thermal properties of the materials can be evaluated at the submicron level.
- The development of characterisation techniques to evaluate experimentally the Seebeck coefficient using scanning thermal microscopy, so that an accurate value of the Seebeck coefficient could be measured without fabricating micro-structure which allows the heat flux flowing inside the structure.
- The first study of Zn_4Sb_3 nanoparticles embedded in silica aerogel including synthesis and complete thermoelectric characterisation have been studied in order to improve the ZT.

The present investigation is focused on the optimising ZT of the Zn4Sb3 material while concurrently developing and deploying of new characterisation techniques. As a consequence, future analysis stemming from this work will likely be divided between studies of improving the thermoelectric properties of the Zn_4Sb_3 material using the sol-gel approach and seeking extended thermal characterisation capabilities.

- Opportunities to improve the thermoelectric properties of the Zn_4Sb_3 material

The main challenge in developing thermoelectric materials with a high figure of merit is to connect the thermoelectric parameters. Nanostructuring can increase the thermopower ($S^2\,\sigma$). Apart from nanostructuring, thermal conductivity can be reduced significantly by introducing porosity within the thermoelectric materials. The main mechanism to lower thermal conductivity in porous materials is by scattering the phonons with pore boundary.

Characterisation of nickel nanoparticles embedded in silica aerogel shows that the electrical resistivity of sample has been decreased by 6 orders of magnitudes as the concentration of nickel nanoparticles has been increased from 0 to 700ppm. While the thermal conductivity has reduced significantly compared with bulk nickel material also stayed unchanged as the concentration of nickel nanoparticles increased from 0 to 700ppm.

The synthesis and characterisation of Zn_4Sb_3 nanoparticles embedded in silica aerogel has been demonstrated in Chapter 5. The electrical resistivity of the sample has increased significantly compared with bulk Zn_4Sb_3 whereas the thermal conductivity has reduced enormously. In order to increase the ZT, it is necessary to increase the concentration of Zn_4Sb_3 nanoparticles beyond 700ppm in silica aerogel. However, there is a limitation in the sol-gel method in synthesis of the samples beyond 700 ppm concentration. At concentrations beyond 700ppm, some nanoparticles agglomerate and precipitate at the bottom of the wet gel during the gelation period, they cannot be dispersed further. Therefore, a higher concentration than 700ppm is only a nominal value. In fact, it is not possible to embed more nanoparticles.

It is believed that the approach, the underlying idea for improving the figure of merit, that showing here is generic and could bring large improvement in thermoelectric properties once the right materials are selected. For example, changing dimensionality, perhaps embedding 2D materials opposed to nanoparticles and nanowires one would be able to increase meaningfully the electrical conductivity of these composites further. However, this is going to be our future study.

- Opportunities in the thermal characterisation

Over the past decade, the nanostructuring has been proven to improve the performance of thermoelectric material. In order to evaluate the performance of thermoelectric materials, it is necessary to obtain an accurate characterisation of the individual parameters in the figure of merit. However, submicron characterisation has been proven to be challenge task in particular, Seebeck coefficient measurement.

The simultaneous temperature and Seebeck coefficient measurement have been demonstrated in Chapter 3 for variety of bulk sample. In this technique the heat is conduct by a Peltier heater to the sample and induced temperature and voltage will be measured using SThM. However, in nanostructured material such as nanowires, it is not possible to use a Peltier heater as heat is conducted to the SThM cantilever by air conduction (described in Chapter 3, Section 2).

In order to measure the Seebeck coefficient of nanowire using this technique, a joule heater test structure is required which will conduct heat from one side sample to another. Extra precaution is required to minimise the heat air conduction from the heater to the cantilever, as it will affect the temperature measurements.

References

[1]. Datta, S. and van Houten, H. (1996) Electronic Transport in Mesoscopic Systems. *Physics Today*, 49(5), pp. 70-70.

[2]. Berggren, K. (1988) Quantum phenomena in small semiconductor structures and devices. *International Journal of Quantum Chemistry*, 33(3), pp. 217-245.

[3]. Datta, S. (2017) *Lessons from nanoelectronics, A New Perspective on Transport*. Singapore: World Scientific Publishing Co. Pte Ltd.

[4]. Pierret, R. F. (1996), *Semiconductor Device Fundamentals*, Addison-Wesley Reading, MA, USA.

[5]. Changwook, J., Raseong, K., Mathieu, L., Supriyo, D. and Mark, L. (2010), On Landauer vs. Boltzmann and full band vs. Effective Mas Evaluation of Thermoelectric Transport Coefficient, *Journal of Applied Physics*, 107, 023707.

[6]. Ziman, J. M. (1964), Principle of the Theory of Solids, *Cambridge University Press*, Cambridge.

[7]. Ashcroft, N. W. and Mermin, N. D. (1976), Solid-State Physics Saunders College Philadelphia, PA.

[8]. Jensen, J. and Krebs, F. (2014) From the Bottom Up - Flexible Solid State Electrochromic Devices. *Advanced Materials*, 26(42), pp. 7231-7234.

[9]. Wong, B. and Mengüç, M. (2007) *Thermal transport for applications in nanomachining*. Berlin: Springer.

[10]. Tritt, T.M. & Subramanian, M.A. (2006), Thermoelectric Materials, Phenomena, and Applications: A Birds Eye View. *MRS Bulletin*. 31 (03), 188–198.

[11]. Goldsmid, H. (2010), Introduction to thermoelectricity. *Heidelberg: Springer*.

[12]. Smith, A.C., Janak, J. and Adler R. (1965), Electronic Conduction in Solid, *McGraw-Hill*, New York, NK.

[13]. Zlatić, V. and Hewson, A. (2009), Properties and applications of thermoelectric materials. *Dordrecht: Springer*.

[14]. Toberer, E.S., May, A.F. & Snyder, G.J. (2010), Zintl Chemistry for Designing High Efficiency Thermoelectric Materials. *Chemistry of Materials*. 22 (3), 624–634.

[15]. Snyder, G.J. and Ursell, T.S. (2003), Thermoelectric Efficiency and Compatibility. *Physical Review Letters*. 91 (14).

[16]. Phillips, P. (2012), Advanced solid state physics. Cambridge: *Cambridge University Press*.

[17]. Snyder, G. J. & Toberer, E. S. (2010), Complex thermoelectric materials. *Materials for Sustainable Energy*, pp. 101–110.

[18]. Chen, G. (2006), Nanoscale heat transfer and nanostructured thermoelectrics. *The Ninth Intersociety Conference on Thermal and Thermomechanical Phenomena In Electronic Systems*, 29, 2.

[19]. David, G. C., David, R. C., Shanhui F., Kenneth E. G., Pawel K., William P. King, Gerald D. Mahan, Arun M., Humphrey J. Maris, Simon R. Ph., Eric P. and Li S. (2014). Nanoscale thermal transport. II. Applied Physics Reviews 1.1: 011305.

[20]. Pierret, R. F. (2003), Advanced Semiconductor Fundamentals, 2nd Ed. Vol. VI, Modular Series on Solid State Devices, *Prentice Hall*, upper saddle River, N.J.

[21]. Yanzhong P., Heng W. (2012), Band Engineering of Thermoelectric Materials, *Advanced Materials* 24, 6125.

[22]. Nolas, G. S., Sharp J. W., Goldsmid, H. J. (2001), Thermoelectrics: Basic Principles and New Materials Development, Berlin/Heidelberg: *Springer*

[23]. Heikes, R. R. & Ure, R. W (1961), Thermoelectricity: *Science and Engineering Interscience*, New York.

[24]. Purdue University (1970), Thermophysical Properties Research Centre. Thermophysical Properties of Matter: The TPRC Data Series; a Comprehensive Compilation of Data, Vol. 1, ed. Y.S. Touloukian. New York: IFI/Plenum.

[25]. Koon, D.W. & Knickerbocker, C.J. (1996), Effects of macroscopic inhomogeneities on resistive and Hall measurements on crosses, cloverleafs and bars. *Review of Scientific Instruments*. 67 (12), 4282–4285.

[26]. Koon, D.W. & Chan, W.K. (1998), Direct measurement of the resistivity weighting function. *Review of Scientific Instruments*. 69 (12), 4218–4220.

[27]. Watkins, C., Shen, B. & Venkatasubramanian, R. (2005), Low-grade-heat energy harvesting using superlattice thermoelectrics for applications in implantable medical devices and sensors. *ICT 2005. 24th International Conference on Thermoelectrics, 2005.* DOI:10.1109/ICT.2005.1519934

[28]. Bottner, H. (2005). Miniaturised thermoelectric devices: Small size, high cooling power densities, short response time. ICT 2005. 24th International Conference on Thermoelectrics, 2005.

[29]. Ashcroft, N.W. and Mermin, N.D. (1976), Solid-State Physics, *Saunders College, Philadelphia*, PA.

[30]. Tarkhanyan, R. & Niarchos, D. (2013), Reduction in lattice thermal conductivity of porous materials due to inhomogeneous porosity. *International Journal of Thermal Sciences*. 67107–112.

[31]. Rauwel, P., Løvvik, O.M., Rauwel, E. & Taftø, J. (2011), Nanovoids in thermoelectric β-Zn4Sb3**:** A possibility for nanoengineering via Zn diffusion. *Acta Materialia*. 59 (13), 5266–5275.

[32]. Lowhorn, N.D., Wong-Ng, W., Lu, Z.Q., Thomas, E., Otani, M., Green, M., Dilley, N., Sharp, J. & Tran, T.N. (2009) Development of a Seebeck coefficient Standard Reference Material. *Applied Physics A*. 96 (2), 511–514.

[33]. Xie, W., Tang, X., Yan, Y., Zhang, Q. & Tritt, T.M. (2009), High thermoelectric performance BiSbTe alloy with unique low-dimensional structure. *Journal of Applied Physics*. 105 (11), 113713.

[34]. Zhou, J., Jin, C., Seol, J.H., Li, X. & Shi, L. (2005), Thermoelectric properties of individual electrodeposited bismuth telluride nanowires. *Applied Physics Letters*. 87 (13), 133109.

[35]. Yamamoto, H., Iguchi, R. & Morishita, M. (2009), Electrodeposition of Zn-Sb Thermoelectric Semiconductor Film in Ethylene Glycol Non-Aqueous Solution Containing Zn(II) and Sb(III). *ECS Transactions*.

[36]. Berland, K., Song, X., Carvalho, P.A., Persson, C., Finstad, T.G. & Løvvik, O.M. (2016) Enhancement of thermoelectric properties by energy filtering: Theoretical potential and experimental reality in nanostructured ZnSb. *Journal of Applied Physics*. 119 (12), 125103.

[37]. Kokh, K., Atuchin, V., Gavrilova, T., Kuratieva, N., Pervukhina, N. & Surovtsev, N. (2014) Microstructural and vibrational properties of PVT grown **Sb2Te3** crystals. *Solid State Communications*. Volume 177. pp16–19.

[38]. Boukai, A.I., Bunimovich, Y., Tahir-Kheli, J., Yu, J.-K., Iii, W.A.G. & Heath, J.R. (2008), Silicon nanowires as efficient thermoelectric materials. *Nature*. 451 (7175), 168–171.

[39]. Bagnich, S.A., Niedermeier, U., Melzer, C., Sarfert, W. & Seggern, H.V. (2009), Electron-hole pair mechanism for the magnetic field effect in organic light emitting diodes based on poly(paraphenylene vinylene). *Journal of Applied Physics*. 106 (11), 113702.

[40]. Evis, Z., Yilmaz, B., Usta, M. & Aktug, S.L. (2013), X-ray investigation of sintered cadmium doped hydroxyapatites. *Ceramics International*. 39 (3), 2359–2363.

[41]. Duan, B., Zhai, P., Ding, S., Xu, C., Li, G., Liu, L., Li, P. & Zhang, Q. (2014), Effects of Nanoparticle Size on the Thermoelectric and Mechanical Properties of Skutterudite Nanocomposites. *Journal of Electronic Materials*. 43 (6), 2115–2120.

[42]. Li, H., Song, Y.R., Yao, M.-Y., Zhu, F., Liu, C., Gao, C.L., Jia, J.-F., Qian, D., Yao, X., Shi, Y.J. & Wu, D. (2013), Carrier density dependence of the magnetic properties in iron-doped **Bi2Se3** topological insulator. *Journal of Applied Physics*. 113 (4), 043926.

[43]. Kunieda, M., Shimizu, K., Eguchi, T., Ueda, N. & Nakamura, H. (2011), Fundamental Properties Of Ultra High Performance-Strain Hardening Cementitious Composites And Usage For Repair. *Journal of Japan Society of Civil Engineers, Ser. E2 (Materials and Concrete Structures)*. 67 (4), 508–521.

[44]. Girard, S.N., He, J., Zhou, X., Shoemaker, D., Jaworski, C.M., Uher, C., Dravid, V.P., Heremans, J.P. & Kanatzidis, M.G. (2011), High Performance Na-doped PbTe–PbS Thermoelectric Materials: Electronic Density of States Modification and Shape-Controlled Nanostructures. *Journal of the American Chemical Society*. 133 (41), 16588–16597.

[45]. Vaidyanathan, R., Cox, S.M., Happek, U., Banga, D., Mathe, M.K. & Stickney, J.L. (2006) Preliminary Studies in the Electrodeposition of PbSe/PbTe Superlattice Thin Films via Electrochemical Atomic Layer Deposition (ALD)†. *Langmuir*. 22 (25), 10590–10595.

[46]. Li, S., Funahashi, R., Matsubara, I., Ueno, K. & Yamada, H. (1999) High temperature thermoelectric properties of oxide $Ca_9Co_{12}O_{28}$. *Journal of Materials Chemistry*. 9 (8), 1659–1660.

[47]. Zhu, S., Xie, W., Thompson, D., Holgate, T., Zhou, M., Yan, Y. & Tritt, T.M. (2011) Tuning the thermoelectric properties of polycrystalline FeSb2 by the in situ formation of Sb/InSb nanoinclusions. *Journal of Materials Research*. 26 (15), 1894–1899.

[48]. Uher, C., Chen, B., Hu, S., Morelli, D. & Meisner, G. (1997), Transport Properties of Partially-Filled CeyCo4Sb12. *MRS Proceedings*. 478.

[49]. Makaya, A. & Fredriksson, H. (2007), Variation of nitrogen solubility and mechanism of pore formation during production of porous Fe–Cr–Mn–Si–C material, *International Journal of Cast Metals Research*, 20, 2, 73-83 .

[50]. He, Q., Luo, H., Wang, Y., Li, W., Su, J., Lei, Z., Chen, Z., Zhang, Y. (2012). Effects of random pores on the thermoelectric properties of $Si_{100}P_{2.5}$ $(GaP)_{1.5}$ bulk, *Acta Physica Sinica*, 61(23).

[51]. Mele, P., Kamei, H., Yasumune, H., Matsumoto, K. & Miyazaki, K. (2014), Development of thermoelectric module based on dense Ca3Co4O9 and Zn0.98Al0.02O legs. *Metals and Materials International*. 20 (2), 389–397.

[52]. Mele, P. (2015), Nanostructured Thin Films of Thermoelectric Oxides. *Oxide Thin Films, Multilayers, and Nanocomposites*. 123–155.

[53]. Nolas, G.S., Slack, G.A., Morelli, D.T., Tritt, T.M. & Ehrlich, A.C. (1996) The effect of rare-earth filling on the lattice thermal conductivity of skutterudites. *Journal of Applied Physics*. 79 (8), 4002.

[54]. Cahill, D. (1988), Lattice Vibrations and Heat Transport In Crystals and Glasses, *Annual Review of Physical Chemistry* 39.1: 93-121.

[55]. Sze, S. M. Physics of Semiconductor Devices. *John Wiley and Sons*, New York (1981).

[56]. Hicks, L. D. and Dresselhaus, M. S. (1993), Effect of quantum-well structures on the thermoelectric figure of merit, *Physical Review B* 47, 12727.

[57]. Weishu, L., Kevin, C. L., Kenneth, M., Sangyeop, L., Qian, Z., Cyril, P. O., Gang, C. and Zhifeng, R.. (2013), Studies on the Bi2Te3–Bi2Se3–Bi2S3 system for mid-temperature thermoelectric energy conversion, *Energy & Environmental Science* 6.2: 552.

[58]. Llin, L.F., Samarelli, A., Zhang, Y., Weaver, J.M.R., Dobson, P., Cecchi, S., Chrastina, D., Isella, G., Etzelstorfer, T., Stangl, J., Gubler, E.M. & Paul, D.J. (2013), Thermal Conductivity Measurement Methods for SiGe Thermoelectric Materials. *Journal of Electronic Materials*. 42 (7), 2376–2380.

[59]. Smith, A. (1965), Seebeck Coefficient in N-Type Germanium-Silicon Alloys: "Competition" Region, *Physical Review* 139, 5A, 159.

[60]. Rama, V., Edward, S., Thomas, C. and Brooks, O. (2001), Thin-film thermoelectric devices with high room-temperature figures of merit, *Nature*, 413, 597-602.

[61]. Paothep, P., Prabhakar, B. (2010), Nanostructured thermoelectrics, *Materials Science and Engineering: R: Reports* 67.2-4: 19-63.

[62]. Chen, Z.-G., Han, G., Yang, L., Cheng, L. & Zou, J. (2012) Nanostructured thermoelectric materials: Current research and future challenge. *Progress in Natural Science: Materials International*. 22 (6), 535–549.

[63]. Hicks, L. D. and. Dresselhaus, M. S. (1996), Thermoelectric figure of merit of a one-dimensional conductor, *Physical Review B* 53, 16.

[64]. Goldsmid, H. (2014), Bismuth telluride and its alloys as materials for thermoelectric generation. *Materials* 7.4, 2577-2592.

[65]. Heng, W., Jianli, W., Xianlong, C. and Jeffrey, S. G. (2014), Thermoelectric alloys between PbSe and PbS with effective thermal conductivity reduction and high figure of merit, *Journal of Materials Chemistry a* 2.9, 3169.

[66]. Dresselhaus, M. S., Dresselhaus, G., Sun, X., Zhang, S. B., Cronin, Z. Koga, T. Ying, and J. Y. Chen, G. (2009). The Promise of Low-Dimensional Thermoelectric Materials, *Advanced Materials*, 19, 1043-1053.

[67]. Zhang, Z., Yee, J. K., Sharma, P. A., and Lavernia, E. J. (2013), Influence of porosity on the transport properties of Bi2Te3-based alloys by field-assisted sintering, *Journal of Materials Research* 28 (13), 1853-1861.

[68]. Sun, X. (2000). Experimental study of the effect of the quantum well structures on the thermoelectric figure of merit in Si /Si1-xGex system. *18th International Conference on Thermoelectrics*.

[69]. Wang, M., Wang, J., Pan, N. and S. Chen (2007), Mesoscopic predictions of the effective thermal conductivity for microscale random porous media, *Physical Review E* 75 (3).

[70]. Li, J. F., Liu, W. S., Zhao, L. D. and Zhou, M. (2010), High-performance nanostructured thermoelectric materials, *NPG Asia Materials* 2.4, 152-158.

[71]. Ganguly, S., Zhou, C., Morelli, D., Sakamoto, J. & Brock, S. L. (2012), *Journal of Physical Chemistry C* 116 (33), 17431-17439.

[72]. Ponomareva I. ,Srivastava D. and Menon M. (2007), thermal conductivity in thin silicon nanowires: phonon confinement effect, *Nano Letters* 7(5): 1155-1159.

[73]. Kim, S.W., Mishim, Y. and Choi, D. C. (2002), Effect of process conditions on the thermoelectric properties of CoSi, *Intermetallic* 10(2), 177-184.

[74]. Boor, J., Kim, D.S., Ao, X., Becker, M., Hinsche, N.F., Mertig, I., Zahn, P. & Schmidt, V. (2012), Thermoelectric properties of porous silicon. *Applied Physics A*. 107 (4), 789–794.

[75]. Brockway, L., Laer, M.V., Kang, Y. & Vaddiraju, S. (2013) Large-scale synthesis and in situ functionalization of **Zn3P2** and **Zn4Sb3** nanowire powders. *Physical Chemistry Chemical Physics*. 15 (17), 6260.

[76]. Jing, X., Anthony, F., Williams, D. S. and White, Jr B. E. (2013). Thermal conductivity of a ZnO nanowire/silica aerogel nanocomposite. *Applied Physics Letters* 102.19: 193101.

[77]. MacDonald, D. (2013) *Thermoelectricity*. Dover Publications.

[78]. Datta, S. (1989) *Quantum phenomena in modern semiconductor devices*. Reading, Mass.: Addison-Wesley.

[79]. Hsu, C., Huang, G., Chu, H., Yu, B., and Yao, D. (2011) An effective Seebeck coefficient obtained by experimental results of a thermoelectric generator module. *Applied Energy*, 88(12), pp. 5173-5179.

[80]. Pauw, L.J.V.D. (1991) A Method of Measuring Specific Resistivity And Hall Effect Of Discs Of Arbitrary Shape. *Semiconductor Devices: Pioneering Papers*. 174–182.

[81]. Koon, D.W. & Chan, W.K. (1998), Direct measurement of the resistivity weighting function. *Review of Scientific Instruments*. 69 (12), 4218–4220.

[82]. Mark, L. (2000), fundamental of carrier transport, 2th Ed., *Cambridge Univ. Press*, Cambridge, UK.

[83]. Incropera, F.P, DeWitt, D.P, Bergman, T.L, Lavine, A.S. (2006), Introduction to Heat Transfer. *Hoboken, NJ: Wiley*. 912.

[84]. Goodson, K.E., Käding, O.W., Rösner, M. & Zachai, R. (1995), Thermal conduction normal to diamond-silicon boundaries. *Applied Physics Letters*. 66 (23), 3134–3136.

[85]. Standard test method for thermal conductivity of solids by means of the guarded-comparative-longitudinal heat flow technique (2009). In Annual Book of ASTM Standards, Vol. 14.02. *West Conshohocken, PA: ASTM Int*. 15.

[86]. Borca-Tasciuc, T., Chen, G. (2004). Experimental techniques for thin-film thermal conductivity characterization In Thermal Conductivity: Theory, Properties, and Applications, ed. Tery M Tritt, 205–37. New York: *Kluwer Academic /Plenum*.

[87]. Broido, D.A., Malorny, M., Birner, G., Mingo, N. & Stewart, D.A. (2007), Intrinsic lattice thermal conductivity of semiconductors from first principles. *Applied Physics Letters*. 91 (23), 231922.

[88]. Wang, X., Jiang, H.T., Yan, C., Deng, F.S., Sun, Y., Li, Y.H., Shi, Y.L. & Chen, H. (2014), Transmission properties near Dirac-like point in two-dimensional dielectric photonic crystals. *EPL (Europhysics Letters)*. 108 (1), 14002.

[89]. Kyeongtae, K., Wonho, J., Woochul, L., Seid, S., Dakotah, T., Edgar, M., and Pramod, R.(2014), Quantification of thermal and contact resistances of scanning thermal probes, *Applied Physics Letters*, 105, 203107.

[90]. Jerzy, B., Justyna, J., Anna, K.-B., Piotr, F., Austin, F. and Mihai, C. (2016), Quantitative Thermal Microscopy Measurement with Thermal Probe Driven by dc+ac Current, *International Journal of Thermophysics*, 37:73.

[91]. Wielgoszewski, G., Sulecki, P., Gotszalk, T., Janus, P., Szmigiel, D., Grabiec, P. and Zschech, E. (2010), Microfabricated resistive high-sensitivity nanoprobe for scanning thermal microscopy, *Journal of Vacuum Science & Technology* B, 28, 6.

[92]. Wonho, J., Sunghoon, H., Edgar, M. & Pramod, R. (2015), Scanning Probe Microscopy for Thermal Transport Measurements, *Nanoscale and Microscale Thermophysical Engineering*, 19: 279–302.

[93]. Bodzenta, J., Juszczyk, J. and Chirtoc, M. (2013), Quantitative scanning thermal microscopy based on determination of thermal probe dynamic resistance, *Review of Scientific Instruments* 84, 093702.

[94]. Séverine, G., Ali, A., and Pierre-Olivier, C. (2015), Scanning thermal microscopy:A review, *Physica Status Solidi A* 212, 3, 477–494.

[95]. Tovee, P., Pumarol, M., Zeze, D., Kjoller, K. and O. Kolosov (2012), Nanoscale spatial resolution probes for scanning thermal microscopy of solid state materials, *Journal of Applied Physics*, 112,114317.

[96]. Cahill, D. (1988) Lattice Vibrations And Heat Transport In Crystals And Glasses. *Annual Review of Physical Chemistry*. 39 (1), 93–121.

[97]. Huang, S., Ruan, X.-D., Fu, X. & Yang, H.-Y. (2009), Measurement of the thermal transport properties of dielectric thin films using the micro-Raman method. *Journal of Zhejiang University-SCIENCE A*. 10 (1), 7–16.

[98]. Liu, M.S., Bursill, L.A., Prawer, S., Nugent, K.W., Tong, Y.Z. & Zhang, G.Y. (1999) Temperature dependence of Raman scattering in single crystal GaN films. *Applied Physics Letters*. 74 (21), 3125–3127.

[99]. Mandelkern, L. & Alamo, R.G. (1995), Comments on Paper "Raman Spectroscopy Employed for the Determination of the Intermediate Phase in Polyethylene". *Macromolecules*. 28 (8), 2988–2989.

[100]. Puyoo, E., Grauby, S., Rampnoux, J.-M., Rouvière, E. & Dilhaire, S. (2011) Scanning thermal microscopy of individual silicon nanowires. *Journal of Applied Physics*. 109 (2), 024302.

[101]. Warzoha R. J.; Fleischer A. S.; (2014), Determining the thermal conductivity of liquids using the transient hot disk method. Part II: Establishing an accurate and repeatable experimental methodology, *International Journal of Heat and Mass Transfer*; 71, 790–807

[102]. Hotdiskinstruments.com, Hot Disk AB-Testing Thermal Conductivity TPS 2500 S. [online] Available at: http://www.hotdiskinstruments.com/products/ instruments-for-thermal conductivity-measurements/tps-2500-s.html

[103]. Harris, D.C., Bertolucci, M.D. (1978), Symmetry and spectroscopy: an introduction to vibrational and electronic spectroscopy, *Oxford University Press*.

[104]. Carey, P.R. (1982), Biochemical Applications of Raman and Resonance Raman Spectroscopies, *Academic Press*.
[105]. Maslen, E. N., Fox, A. G., & O'Keefe, M. A. (2004), X-ray Scattering, in: E. Prince (Ed), *International Tables for Crystallography*, Vol. C (Kluwer Academic, Dordrecht, p. 554.
[106]. Williams D.B. & Carter C.B. (1996), The Transmission Electron Microscope. In: Transmission Electron Microscopy. *Springer*, Boston, MA
[107]. Tamon, H., Kitamura, T. & Okazaki, M. (1998), Preparation of Silica Aerogel from TEOS. *Journal of Colloid and Interface Science*. 197 (2), 353–359.
[108]. Kim, K., Jeong, W., Lee, W., Sadat, S., Thompson, D., Meyhofer, E. & Reddy, P. (2014), Quantification of thermal and contact resistances of scanning thermal probes. *Applied Physics Letters*. 105 (20), 203107.
[109]. Bodzenta, J., Juszczyk, J., Kaźmierczak-Bałata, A., Firek, P., Fleming, A. & Chirtoc, M. (2016), Quantitative Thermal Microscopy Measurement with Thermal Probe Driven by dc ac Current. *International Journal of Thermophysics*. 37 (7).
[110]. Raphaël, O., Trannoy, N., and Grossel, P. (2012) Thermal Resonance at the Microscale in AC Scanning Thermal Microscopy with a Thermal-Resistive Probe. *International Journal of Thermophysics*, 33(7), pp. 1259-1269.
[111]. W. Jeong, S.Hur, E. Meyhofer, and P. Reddy (2015), Scanning Probe Microscopy for Thermal Transport Measurements, Nanoscale and Microscale Thermophysical Engineering 19, 279.
[112]. Bodzenta, J., Juszczyk, J. & Chirtoc, M. (2013), Quantitative scanning thermal microscopy based on determination of thermal probe dynamic resistance. *Review of Scientific Instruments*. 84 (9), 093702.
[113]. Gomès, S., Assy, A. and Chapuis, P.-O. (2015), Scanning thermal microscopy: A review Physica Status Solidi (a) 212, 477.
[114]. Kushvaha, S.S., Hofbauer, W., Loke, Y.C., Singh, S.P. & O'Shea, S.J. (2011), Thermoelectric measurements using different tips in atomic force microscopy. *Journal of Applied Physics*. 109 (8), 084341.
[115]. Grauby, S., Puyoo, E., Rampnoux, J.-M., Rouvière, E. & Dilhaire, S. (2013), Si and SiGe Nanowires: Fabrication Process and Thermal Conductivity Measurement by 3ω-Scanning Thermal Microscopy. *The Journal of Physical Chemistry C*. 117 (17), 9025–9034.
[116]. Lefèvre, S., Volz, S. & Chapuis, P.-O. (2006), Nanoscale heat transfer at contact between a hot tip and a substrate. *International Journal of Heat and Mass Transfer*. 49 (1-2), 251–258.

[117]. David, L., Gomes, S. and Raynaud, M. (2007), Modelling for the thermal characterisation of solid materials by dc scanning thermal microscopy. *Journal of Physics D: Applied Physics*, 40(14), 4337.

[118]. Dinwiddie, R., Pylkki, R. and West, P. (1993), Thermal conductivity contrast imaging with a scanning thermal microscope. Thermal conductivity, **22**, 668-668.

[119]. Dobson, P.S., Weaver, J.M. and Mills, G. (2007), New Methods for Calibrated Scanning Thermal Microscopy (SThM), Proc. IEEE Sensors.

[120]. Despont, M., Brugger, J., Drechsler, U., Dürig, U., Häberle, W., Lutwyche, M., Rothuizen, H., Stutz, R., Widmer, R., Binnig, G., Rohrer, H. & Vettiger, P. (2000) VLSI-NEMS chip for parallel AFM data storage. *Sensors and Actuators A: Physical*. 80 (2), 100–107.

[121]. Fischer, H. (2005), Quantitative determination of heat conductivities by scanning thermal microscopy. *Thermochimica Acta*. 425 (1-2), 69–74.

[122]. Gomès, S., Trannoy, N. & Grossel, P. (1999), DC thermal microscopy: study of the thermal exchange between a probe and a sample. *Measurement Science and Technology*. 10 (9), 805–811.

[123]. Lefèvre, S., Volz, S., Saulnier, J.-B., Fuentes, C. & Trannoy, N. (2003), Thermal conductivity calibration for hot wire based dc scanning thermal microscopy. *Review of Scientific Instruments*. 74 (4), 2418–2423.

[124]. Assy, A. & Gomès, S. (2015), Temperature-dependent capillary forces at nano-contacts for estimating the heat conduction through a water meniscus. *Nanotechnology*. 26 (35), 355401.

[125]. Prasher, R. (2005), Predicting the Thermal Resistance of Nanosized Constrictions. *Nano Letters*. 5 (11), 2155–2159.

[126]. Watari, K., Hirao, K., Toriyama, M. & Ishizaki, K. (2004), Effect of Grain Size on the Thermal Conductivity of Si3N4. *Journal of the American Ceramic Society*. 82 (3), 777–779.

[127]. Tovee, P. (2012), Nanoscale spatial resolution probes for Scanning Thermal Microscopy of solid state materials. *Journal of Applied Physics*. 112(11), 114317.

[128]. Shivaprasad, S. and Angadi, M. Temperature coefficient of resistance of thin palladium films. *Journal of Physics D: Applied Physics,* 1980. 13(9): p. L171.

[129]. Lee, J., Wright, T. L., Abel, M. R., Sunden, E. O., Marchenkov, A., Graham, S. and King, W. P. (2007), Thermal conduction from microcantilever heaters in partial vacuum, *Journal of Applied Physics,* 101:014906.

[130]. Lee, B., Prater, C. B. and King, W. P. (2012), Lorentz Force actuation of a heated atomic force microscope cantilever, Nanotechnology, 23:055709.

[131]. Zhang, Y. L., Castillo, E. E., Mehta, R. J., Ramanath, G. and Borca-Tasciuc, T. (2011), A noncontact thermal microprobe for local thermal conductivity measurement, Rev. Sci. Instrum., 82:024902.

[132]. King, W. P. and Goodson, K. E. (2007), Thermomechanical formation of nanoscale polymer indents with a heated silicon tip, ASME J. Heat Trans., 129:1600–1604.

[133]. Nelson, B. A. and King, W. P. (2008), Modelling and simulation of the interface temperature between a heated silicon tip and a substrate, Nanosc. Microsc. Therm., 12:98–115.

[134]. Majumdar, A. (1999), Scanning thermal microscopy, Annual Review of Materials Science, 29, 505.

[135]. Luo, K., Shi, Z., Varesi, J. and Majumdar, A. (1997), Sensor nanofabrication, performance, and conduction mechanisms in scanning thermal microscopy, *Journal of Vacuum Science & Technology* B, 15,349.

[136]. Kasper, M. J., Natrajan, V. K., Privorotskaya, N. L., Christensen, K. T. and King, W. P. (2010), Natural advection from a microcantilever heat source, *Applied Physics Letters*, 96:063113.

[137]. Hao, Y., Anders, B. B., Mogens, C., and Bo, B. I. (2014), Fast Direct Synthesis and Compaction of Homogenous Phase-Pure Thermoelectric Zn_4Sb_3, ACS Applied Materials and Interfaces, 6 (13), 10542–10548.

[138]. Zhang, Y., Hapenciuc, C.L., Castillo, E.E., Borca-Tasciuc, T., Mehta, R.J., Karthik, C. & Ramanath, G. (2010) A microprobe technique for simultaneously measuring thermal conductivity and Seebeck coefficient of thin films. Applied Physics Letters. 96 (6), 062107.

[139]. Geballe, T.H. & Hull, G.W. (1955), Seebeck Effect in Silicon. *Physical Review*. 98 (4), 940–947

[140]. Martín-González, M., Caballero-Calero, O. & Díaz-Chao, P. (2013), Nanoengineering thermoelectrics for 21st century: Energy harvesting and other trends in the field. *Renewable and Sustainable Energy Reviews*. 24288–305.

[141]. Cahill, G., Ford, W. K., Goodson, K. E., Mahan, G. D., Majumdar, A., Maris, H. J., Merlin, R. and Phillpot, S. R. (2014), Nanoscale thermal transport. II. *Applied Physics Reviews* 1, 011305.

[142]. Hopkins, P.E., Rakich, P.T., Olsson, R.H., El-Kady, I.F. & Phinney, L.M. (2009), Origin of reduction in phonon thermal conductivity of microporous solids. *Applied Physics Letters*. 95 (16), 161902.

[143]. Li, H., Yu, Y. & Li, G. (2014), Computational modelling and analysis of thermoelectric properties of nanoporous silicon. *Journal of Applied Physics*. 115 (12), 124316.

[144]. Fricke, J., Hummer, E., Morper, H. J. and Scheuerpflug, P. (1989), Methods and compositions for preparing silica aerogels, *Journal De Physique* **50**, C487.

[145]. Choi, S. G., Ha, T. J., Yu, B. G., Jaung, S. P., Kwon, O., Park, H. H. (2008), Improvement of uncooled infrared imaging detector by using mesoporous silica as a thermal isolation layer, *Ceramics International*, 34, 833.

[146]. Coquil, T., Hutchinson, N., Pilon, L., Richman, E. & Tolbert, S. (2009), Thermal Conductivity of Cubic and Hexagonal Mesoporous Silica Thin Films. *Volume 2: Theory and Fundamental Research; Aerospace Heat Transfer; Gas Turbine Heat Transfer; Computational Heat Transfer*.

[147]. Jones, S. M. (2006), Aerogel: Space exploration applications, *Journal of Sol-Gel Science Technology* 40, 351.

[148]. Meftah, M., Gharibshahi, E., Soltani, N., Yunusand, W. M. M. and Saion, E. (2014), Structural, Optical and Electrical Properties of PVA/PANI/Nickel Nanocomposites Synthesised by Gamma Radiolytic Method, *Polymers* **6**, 2435.

[149]. Liu, W., Herrmann, A. K., Bigall, N. C., Rodriguez, P., Wen, D., Oezaslan, M., Schmidt, T. J., Gaponik, N. and Eychmüller, A. (2015), Noble Metal Aerogels—Synthesis, Characterisation and Application as Electrocatalysts, *Accounts of Chemical Research* 48, 154.

[150]. Zhou, S., Wang, M., Chen, X. and Xu, F. (2015), Facile Template Synthesis of Microfibrillated Cellulose/Polypyrrole/Silver Nanoparticles Hybrid Aerogels with Electrical Conductive and Pressure Responsive Properties, *ACS Sustainable Chemistry and Engineering* 3, 3346.

[151]. Han, X., Williamson, F., Bhaduri, G. A., Harvey, A. and Siller, L. (2015), Synthesis and characterisation of ambient pressure dried composites of silica aerogel matrix and embedded nickel nanoparticles, *The Journal of Supercritical Fluids* 106, 140.

[152]. Xie, J., Frachioni, A., Williams, D.S. & White, B.E. (2013) Thermal conductivity of a ZnO nanowire/silica aerogel nanocomposite. *Applied Physics Letters*. 102 (19), 193101.

[153]. Ganguly, S., Zhou, C., Morelli, D., Sakamoto, J. & Brock, S.L. (2012), Synthesis and Characterization of Telluride Aerogels: Effect of Gelation on Thermoelectric Performance of Bi2Te3 and Bi2–xSbxTe3 Nanostructures. *The Journal of Physical Chemistry C*. 116 (33), 17431–17439.

[154]. Warren, S.C., Perkins, M.R., Adams, A.M., Kamperman, M., Burns, A.A., Arora, H., Herz, E., Suteewong, T., Sai, H., Li, Z., Werner, J., Song, J., Werner-Zwanziger, U., Zwanziger, J.W., Grätzel, M., Disalvo, F.J. & Wiesner, U. (2012) A silica sol–gel design strategy for nanostructured metallic materials. *Nature Materials*. 11 (5), 460–467.

[155]. Ryan, J.V., Berry, A.D., Anderson, M.L., Long, J.W., Stroud, R.M., Cepak, V.M., Browning, V.M., Rolison, D.R. & Merzbacher, C.I. (2000), Electronic connection to the interior of a mesoporous insulator with nanowires of crystalline RuO2. *Nature*. 406 (6792), 169–172.

[156]. Watcharotone, S., Dikin, D.A., Stankovich, S., Piner, R., Jung, I., Dommett, G.H.B., Evmenenko, G., Wu, S.-E., Chen, S.-F., Liu, C.-P., Nguyen, S.T. & Ruoff, R.S. (2007), Graphene−Silica Composite Thin Films as Transparent Conductors. *Nano Letters*. 7 (7), 1888–1892.

[157]. Chwang, R., Smith, B. & Crowell, C. (1974), Contact size effects on the van der Pauw method for resistivity and Hall coefficient measurement. *Solid-State Electronics*. 17 (12), 1217–1227.

[158]. Chen, L., Fang, M., Liu, C., Liu, X. & Xing, S. (2015), Correction: Manipulating the nickel shape and catalytic performance: from spheres to chains to urchins. *CrystEngComm*. 17 (47), 9240–9240.

[159]. Abdurakhmanov, U., Rakhimova, Y., Mukhamedov, G. & Balberg, I. (2009), Temperature Dependence of the Conductivity in Ceramic Materials Containing Nickel Nanoparticles. *Journal of the American Ceramic Society*. 92 (3), 661–664.

[160]. Sandler, J., Kirk, J., Kinloch, I., Shaffer, M. & Windle, A. (2003), Ultra-low electrical percolation threshold in carbon-nanotube-epoxy composites. *Polymer*. 44 (19), 5893–5899.

[161]. Wang, Z., Shen, X., Han, N.M., Liu, X., Wu, Y., Ye, W. & Kim, J.-K. (2016), Ultralow Electrical Percolation in Graphene Aerogel/Epoxy Composites. *Chemistry of Materials*. 28 (18), 6731–6741.

[162]. Irin, F., Das, S., Atore, F.O. & Green, M.J. (2013) Ultralow Percolation Threshold in Aerogel and Cryogel Templated Composites. *Langmuir*. 29 (36), 11449–11456.

[163]. Dugdale, J.S. (2016), *The electrical properties of metals and alloys*. Mineola, NY: Dover Publications, Inc.

[164]. Li, J.-F., Liu, W.-S., Zhao, L.-D. & Zhou, M. (2010), High-performance nanostructured thermoelectric materials. *NPG Asia Materials*. 2 (4), 152–158.

[165]. Xue, W. & Gu, W. (2016), Conductivity size effect of polycrystalline metal nanowires. *AIP Advances*. 6 (11), 115001.

[166]. Wei, G., Wang, L., Xu, C., Du, X. & Yang, Y. (2016), Thermal conductivity investigations of granular and powdered silica aerogels at different temperatures and pressures. *Energy and Buildings*. 118, 226–231.

[167]. Perry, R. H.; Green, D. W., eds. (1997), *Perry's Chemical Engineers' Handbook* (7th ed.). McGraw-Hill.

[168]. Eckert, E.R.G. & Drake, R.M. (1987), *Analysis of heat and mass transfer*. London: Hemisphere.

[169]. Mozharivskyj, Y., Pecharsky, A.O., Budko, S. & Miller, G.J. (2004) A Promising Thermoelectric Material: Zn4Sb3 or $Zn_{6-\delta}Sb_5$. Its Composition, Structure, Stability, and Polymorphs. Structure and Stability of $Zn_{1-\delta}$ Sb. *Chemistry of Materials*. 16 (8), 1580–1589.

[170]. Chitroub, M., Besse, F. & Scherrer, H. (2008) Thermoelectric properties of semi-conducting compound Zn4Sb3. *Journal of Alloys and Compounds*. 460 (1-2), 90–93.

[171]. Toberer, E.S., Rauwel, P., Gariel, S., Taftø, J. & Snyder, G.J. (2010) Composition and the thermoelectric performance of β-Zn4Sb3. *Journal of Materials Chemistry*. 20 (44), 9877.

[172]. Viennois, R., Record, M.-C., Izard, V. & Tedenac, J.-C. (2007) Raman scattering study of the lattice dynamics of β-Zn4−xCdxSb3. Journal of Alloys and Compounds. 440 (1-2).

[173]. Harnwunggmoung, A., Kurosaki, K., Muta, H. & Yamanaka, S. (2010) Thermoelectric Properties of CoSb3-based Skutterudite Compounds. *MRS Proceedings*. 1267.

[174]. Snyder, G.J., Christensen, M., Nishibori, E., Caillat, T. & Iversen, B.B. (2004) Disordered zinc in Zn4Sb3 with phonon-glass and electron-crystal thermoelectric properties. *Nature Materials*. 3 (7), 458–463.

[175]. Wang, S., Li, H., Qi, D., Xie, W. & Tang, X. (2011) Enhancement of the thermoelectric performance of β-Zn4Sb3 by in situ nanostructures and minute Cd-doping. *Acta Materialia*. 59 (12), 4805–4817.

[176]. Toberer, E.S., Rauwel, P., Gariel, S., Taftø, J. & Snyder, G.J. (2010) Composition and the thermoelectric performance of β-Zn4Sb3. *Journal of Materials Chemistry*. 20 (44), 9877.

[177]. Li, G., Li, Y., Liu, L., Zhang, Q. & Zhai, P. (2013) Lattice thermal conductivity prediction of nanoporous β-Zn4Sb3: A nonequilibrium molecular dynamics simulation. *Materials Letters*. 107348–350.

[178]. Toberer, E.S., Sasaki, K.A., Chisholm, C.R.I., Haile, S.M., Goddard, W.A. & Snyder, G.J. (2007) Local structure of interstitial Zn in β-Zn4Sb3. *physica status solidi (RRL) – Rapid Research Letters*. 1 (6), 253–255.

[179]. Klein, L.C. (1994) A review of: "Sol-Gel Science - The Physics and Chemistry of Sol-Gel Processing" Edited by C. Jeffrey Brinker and George W. Scherer. *Materials and Manufacturing Processes*. 9 (5), 1007–1008.

[180]. Li, G., Li, Y., Zhang, Q., Liu, L. & Zhai, P. (2012) Effects of Disordered Atoms and Nanopores on Mechanical Properties of β-Zn4Sb3: a Molecular Dynamics Study. *Journal of Electronic Materials*. 42 (7), 1514–1521.

[181]. Tamon, H., Kitamura, T. & Okazaki, M. (1998) Preparation of Silica Aerogel from TEOS. *Journal of Colloid and Interface Science*. 197 (2), 353–359.

[182]. Rauwel, P., Løvvik, O.M., Rauwel, E. & Taftø, J. (2011) Nanovoids in thermoelectric β-Zn4Sb3: A possibility for nanoengineering via Zn diffusion. *Acta Materialia*. 59 (13), 5266–5275.

[183]. Błaszczyński, T., Ślosarczyk, A. & Morawski, M. (2013) Synthesis of Silica Aerogel by Supercritical Drying Method. *Procedia Engineering*. 57200–206.

[184]. Yin, H., Blichfeld, A.B., Christensen, M. & Iversen, B.B. (2014) Fast Direct Synthesis and Compaction of Homogenous Phase-Pure Thermoelectric Zn4Sb3. *ACS Applied Materials & Interfaces*. 6 (13), 10542–10548.

[185]. Carlini, R., Marré, D., Pallecchi, I., Ricciardi, R. & Zanicchi, G. (2014) Thermoelectric properties of Zn4Sb3 intermetallic compound doped with Aluminum and Silver. *Intermetallics*. 4560–64.

[186]. Caillat, T., Fleurial, J.-P. & Borshchevsky, A. (1997) Preparation and thermoelectric properties of semiconducting Zn4Sb3. *Journal of Physics and Chemistry of Solids*. 58 (7), 1119–1125.

[187]. Denoix, A., Solaiappan, A., Ayral, R., Rouessac, F. & Tedenac, J. (2010) Chemical route for formation of intermetallic Zn4Sb3 phase. *Journal of Solid State Chemistry*. 183 (5), 1090–1094.

[188]. Nylen, J., Andersson, M., Lidin, S. & Haeussermann, U. (2005) The Structure of β-Zn4Sb3: Ordering of the Phonon-Glass Thermoelectric Material β-Zn4Sb3. *ChemInform*. 36 (13).

[189]. Mohamad, A.B. & Hisao, A. (2014) The Effects of Doping Bismuth on the Thermoelectric Properties of Zn4Sb3. *The Malaysia-Japan Model on Technology Partnership*. 237–241.

[190]. Rauwel, P., Løvvik, O.M., Rauwel, E., Toberer, E.S., Snyder, G.J. & Taftø, J. (2011) Nanostructuring in β-Zn4Sb3 with variable starting Zn compositions. *physica status solidi (a)*. 208 (7), 1652–1657.

[191]. Yin, H., Johnsen, S., Borup, K.A., Kato, K., Takata, M. & Iversen, B.B. (2013) Highly enhanced thermal stability of Zn4Sb3 nanocomposites. *Chemical Communications*. 49 (58), 6540.

[192]. Li, Y., Dou, Y., Qin, X., Zhang, J., Xin, H., Li, D., Song, C., Zou, T., Liu, Y. & Li, C. (2016) Enhanced ZT in p-type β-Zn4Sb3/Bi0.4Sb1.6Te3 nanocomposites. *RSC Advances*. 6 (15), 12243–12248.